The Dissertation Committee for Mitchell George Moore
certifies that this is the approved version of the following dissertation:

Unsteady Growth and Relaxation of Viscous Fingers

Committee:

Harry L. Swinney, Supervisor

J. B. Swift

W. D. McCormick

Michael P. Marder

Graham F. Carey

Unsteady Growth and Relaxation of Viscous Fingers

by

Mitchell George Moore, B.S.

DISSERTATION

Presented to the Faculty of the Graduate School of

The University of Texas at Austin

in Partial Fulfillment

of the Requirements

for the Degree of

DOCTOR OF PHILOSOPHY

THE UNIVERSITY OF TEXAS AT AUSTIN

December 2003

Dedicated to my parents, Thomas and Patricia Moore.

Acknowledgments

This work was supported by the NASA Microgravity Program and the Office of Naval Research. I also received support from a University of Texas Continuing Fellowship.

No work of this magnitude is ever done alone. Anne Juel and John Burgess were my partners for all of the work done with the linear cell, and Eran Sharon was my partner for the work done with the radial cell. Their ideas and hard work were essential to the success of these projects.

In addition, John Burgess in particular was in many ways my immediate mentor, and I thank him for all he taught me, about both experimental physics and life.

I thank Steve Van Hook, Scott Franklin, and Eric Weeks for their advice and friendship early in my graduate career. I thank Erin Rericha, Beth Lewis, and the other members of the Center for Nonlinear Dynamics for their friendship and support as well.

I'd like to thank all those in the physics community with whom I've had many useful discussions on these projects, particularly Mark Mineev, who was our original inspiration for beginning these experiments. I thank Baruch Meerson and his colleagues for inspiring our coarsening work and for providing the images in fig. 3.6.

I possess no great talent for dealing with bureaucracy — quite the opposite in fact. So I must thank Dorothy Featherling, Theresa Hancock, Olga Vera, and Norma Kotz for dealing with it for me on many occasions.

I thank J. B. Swift and W. D. McCormick for always having their doors open for discussions. They always brought valuable insight to my questions and problems. I thank Professor Swift also for the excellent classes he taught; he was the best classroom teacher I've ever had.

My highest gratitude goes to Harry Swinney for all his help and guidance. He has shown the patience of many saints in dealing with my quirks and foibles during my graduate career. I could not have hoped for a better advisor.

I must also present a special thanks to the community at the First Unitarian Universalist Church of Austin, especially the members of the Voyagers group. Joining this community has been truly life altering. I could not hope to thank all the individuals there who have touched me, but I must at least mention the members of the KNOT covenant group: Ellen Briggs, Carrie (Oennika) Cook, Kristen Freeman, Carolyn Gremminger, Grog, Jenna Martin, Catherine Meiners, Vanessa Smith, Monica Smoot, Florence Thompson, David Spregelmeyer, and Lisa Sutton.

And to Carrie, Catherine, and Lisa particularly: You have been the rocks I have clung to through the storms and enriching companions on sunny days. This day might not have come without you. I love you dearly.

MITCHELL GEORGE MOORE

The University of Texas at Austin
17 November 2003

Unsteady Growth and Relaxation of Viscous Fingers

Publication No. _____

Mitchell George Moore, Ph.D.
The University of Texas at Austin, 2003

Supervisor: Harry L. Swinney

Viscous fingering occurs when a less viscous fluid is driven into a more viscous fluid in a porous medium or a thin layer geometry known as a Hele-Shaw cell. The problem is studied because of its applications to filtration and oil extraction, because of its relationship to other moving interface problems, such as solidification and flame fronts, and because the mathematical idealization of the problem has a number of unusual properties.

One set of our experiments was performed in rectangular Hele-Shaw channels where fingers travel down the long axis of the cell. These experiments revealed several phenomena that were not observed in previous experiments. At low flow rates, growing fingers exhibited width fluctuations that intermittently narrowed the finger as they evolved. The magnitude of these fluctuations was proportional to $\mathrm{Ca}^{-0.64}$, where Ca is the capillary number, which is proportional to the finger velocity. This relation held for all aspect ratios studied ($60 <$ (channel width)/(channel thickness) < 500) up to the

onset of tip instabilities in the fingers. At higher flow rates, finger pinch-off and reconnection events were observed. These events appear to be caused by an interaction between the actively growing finger and suppressed fingers at the back of the channel. Both the fluctuation and pinch-off phenomena were robust but not explained by current theory.

Our other experiments were performed in a Hele-Shaw cell with radial symmetry. These fingers generate highly ramified patterns as the air enters the cell from a central point. We have examined the relaxation of the fine structure of these patterns due to surface tension by removing the forcing after a pattern was grown. This relaxation, unlike most coarsening processes, was not dynamically scale invariant. Rather, it exhibits two distinct dynamic length scales that grow as different powers of time: $l_1(t) \sim t^{0.22}$, $l_2(t) \sim t^{0.31}$. These lengths correspond respectively to the scale below which the pattern is smooth (non-ramified) and the distance between different fingers in the pattern. The measured exponents were in agreement with the results of recent numerical studies of diffusion-controlled coarsening of fractal clusters [Lipshtat *et al.* Phys. Rev. E **65**, 050501 (2002)]. A consequence of the existence of two length scales is that the patterns at late times depended on the structural form at the onset of coarsening, providing information on the age of the fractal. We also present preliminary work on the fractal dimension of viscous fingering patterns.

Table of Contents

List of Tables

List of Figures

Chapter 1

Introduction

1.1 Viscous Fingering

Viscous fingering occurs whenever a less viscous fluid displaces a more viscous fluid in either a porous medium or a quasi-two-dimensional geometry known as a Hele-Shaw cell. The less viscous fluid pushes through the more viscous fluid, creating propagating "fingers" and leaving the more viscous fluid behind. Fig. 1.1 shows a single finger of water penetrating an oil in a Hele-Shaw cell.

The problem of viscous fingering in a Hele-Shaw cell was first studied by Saffman and Taylor in 1958 [122]. They used the Hele-Shaw geometry [49]

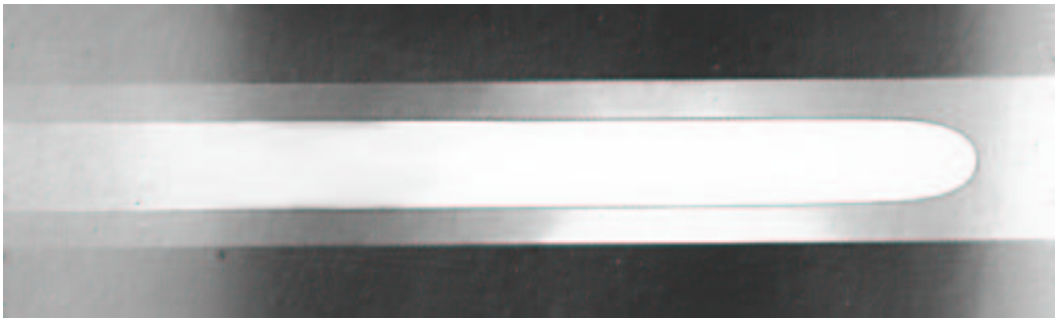

Figure 1.1: A single finger of water penetrating an oil in a Hele-Shaw channel, from Saffman and Taylor's original work [122]. The finger is travelling at a uniform rate from left to right and is half the width of the cell.

because fluid in the cell obeys the same equation of motion as fluids in porous media, Darcy's Law [38]; their underlying motivation was to investigate phenomena that occur in oil extraction. The primary instability from a flat front to fingers occurs when ground water moves to replace oil being extracted from an underground reservoir. Oil extraction ceases once water has fingered through the reservoir, and as a result, as much as half of the oil is left behind, dramatically reducing the extraction efficiency. The study of viscous fingering thus has a bearing on a number of practical concerns related to flow through porous media.

1.2 Related Moving Interface Problems

Another reason this problem is studied is that it is generally regarded as the simplest problem in the class of moving interface problems, which includes directional solidification (fig. 1.2) and crystallization, dendritic growth (fig. 1.3), chemical electrodeposition, and combustion fronts (fig. 1.4). Mathematically, moving interface problems are referred to as Stefan problems [36].

The mathematics underlying these problems are not identical to the viscous fingering problem; these problems are diffusional, while viscous fingering is Laplacian. In other words, viscous fingering (as we shall see in sec. 2.2) obeys Laplace's equation for the pressure ($\nabla^2 P = 0$), while the driving fields in these other problems (temperature and/or concentration U) obey the diffusion equation ($D\nabla^2 U = \partial U/\partial t$, D is the diffusion constant) instead [36, 109]. But in the limit where the diffusion length ($\ell = D/V$, V is the front velocity)

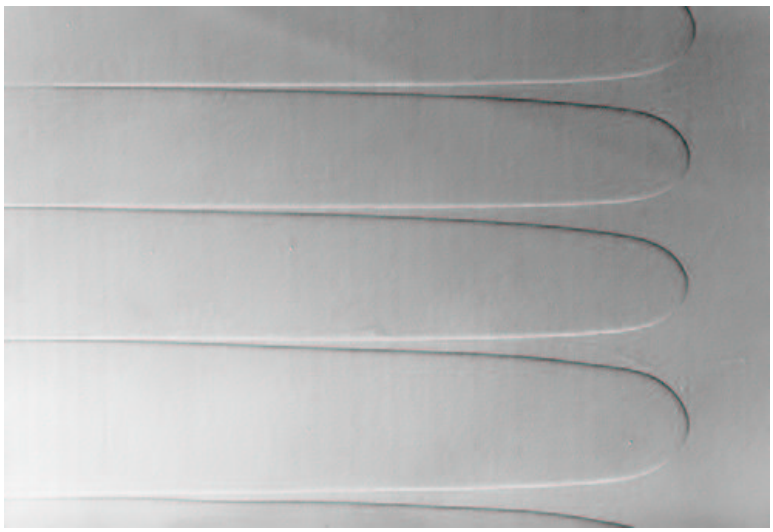

Figure 1.2: Directional solidification of succinonitrile. The solidification front is propagating from left to right; the fingers on the left are solid succinonitrile penetrating into supercooled liquid succinonitrile on the right. The Peclet number $P = 2aV/D$ is 0.3 (where a is a characteristic length of the system, V is the front velocity, and D is the diffusion constant). From Pelcé [109].

is large compared to the system's characteristic lengths, the time derivative term is small and the system is quasi-Laplacian [36]. (This is usually expressed as requiring that the Peclet number $P = 2aV/D$ is small, where a is a characteristic length of the system [109].)

Another difference between viscous fingering and solidification, dendritic growth, and electrodeposition is crystalline anisotropy. This creates a surface tension term that can vary along different growth directions. The main result of this anisotropy is that the mechanism of secondary instabilities becomes side-branching (as in fig. 1.3) instead of tip splitting (as in fig. 2.16). A number of erroneous references are made to side-branching in the isotropic

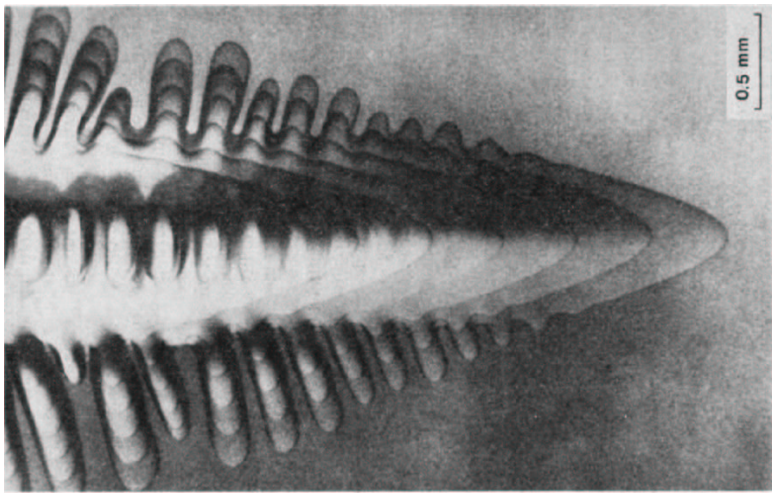

Figure 1.3: Multiple-exposure photograph of a growing succinonitrile dendritic crystal. The solidification front is propagating from left to right. Side branches are growing on four sides (up, down, out of the page, into the page). From Huang and Glicksman [53].

viscous fingering literature; all of these are in fact what Lajeunesse and Couder refer to as "imperfect tip splitting" [67], which occurs when one of the branches following a tip split stops growing due to the constraints of the walls of the cell and of nearby fingers. True side-branches start and grow only after the tip has passed.

Combustion front propagation can possess even more complications. There can be many different regimes of ignition chemistry which can feature an interplay between diffusion of different chemical species and/or heat. The underlying mathematics is similar to viscous fingering only when the diffusion of one element (heat or one chemical species) dominates and possesses a diffusive length scale on the order of the system size (as with solidification). Also,

Figure 1.4: A fingering instability in burning paper in an essentially two-dimensional chamber. In this image, oxygen flows to the left as the front propagates to the right. As the oxygen flow is decreased, fingers first form and then tip splitting occurs. (False-color photo on cover of January 1999 Physics Today [76], contributed by Zik, Olami, and Moses [148]).

three dimensional effects due to convection cannot be avoided in general, and fingering patterns do not occur in such a case [76]. But when convection effects can be negated somehow, either by an appropriate geometry [148], or by removing gravity as was done in a space shuttle experiment [76], then fingering patterns such as those in fig. 1.4 can occur.

However, as different as these systems can be, they all essentially reduce to the viscous fingering problem in the appropriate limit (large diffusion length, as discussed above). Studying viscous fingering phenomena should thus aid our understanding of these more complex problems as well.

1.3 Organization

The remainder of this dissertation is organized as follows. Chapter 2 covers the history and background of viscous fingering, which is quite extensive — the problem has been studied for 45 years. Chapter 3 covers the background of a related phenomenon, diffusion limited aggregation, and its relationship to a new scenario of domain coarsening.

Chapter 4 covers the experimental setups for both the channel and radial cells in great detail. This includes the description of the data acquisition procedures and initial image processing.

Chapter 5 presents our primary results from the channel, fluctuating fingers. At low flow rates, growing fingers undergo width fluctuations that intermittently narrow the finger as they evolve. This phenomenon is quantitatively robust but not explained by current theory.

Chapter 6 presents our primary result from the radial cell, the relaxation of fractal viscous fingering patterns. These patterns undergo a coarsening process that, unlike most coarsening processes, is not dynamically scale invariant. The system exhibits two distinct length scales that grow as different powers of time, with exponents in agreement with those from recent simulations of fractal coarsening.

Chapter 7 presents an overview of other results, including the observation of finger pinch-off events, and describes current research being performed. Chapter 8 provides a brief summary and conclusion.

Appendix A contains the designs for all parts submitted to the machine shop. Appendix B contains the details of several calculations made during the design of the experiments described in chapter 4.

Chapter 2

Background: Viscous Fingering

2.1 Saffman-Taylor Fingering

The phenomenon of viscous fingering was first studied in 1952 by Hill [50], a researcher working for a sugar producing company. During one stage of the refining of beet and cane sugar, viscous sugar solutions were driven through large granular charcoal filters. The adsorptive power of the filters decreased as they became clogged over time, reaching a point where the purity of the sugar solution after filtration was unacceptably low. They then wished to clear the rest of the sugar solution from the filter by flushing water through. Hill discovered that this was only effective in the center section of the channel; the edges remained filled with the viscous sugar solution. He referred to this as "channelling", but it is clearly an early example of miscible viscous fingering in a porous medium.

The foundation of the field was laid in 1958 by the classic paper of Saffman and Taylor [122] on their studies of viscous fingering in Hele-Shaw channels. Their work on the motion of single fingers posed questions that went unanswered for more than twenty years, and some of those originally proposed answers are still being debated today. The analytic work in Saffman

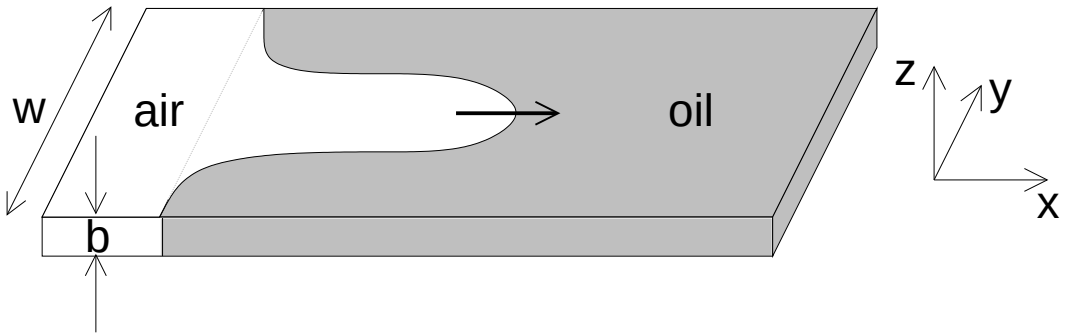

Figure 2.1: A schematic view of a Hele-Shaw channel. Oil flows out of the channel uniformly across the width of the cell. The gap thickness b is much less than the width w. The coordinates used for the calculations in the text are also shown.

and Taylor's original paper was also performed and published independently in 1959 by Chuoke, van Meurs, and van der Poel [25], and in 1956 by Zhuravlev [147] in the Soviet Union.

While this section will attempt an overview of work done on this system, a number of good reviews are available: Bensimon, Kadanoff, Liang, Shraiman, and Chao [13], Homsy [51], Kessler, Koplik, and Levine [59], Pelcé [109], and Couder [37]. A list of references on moving boundary problems in Hele-Shaw flows can be found at
http://www.maths.ox.ac.uk/∼howison/Hele-Shaw/ [45].

2.2 Hele-shaw Geometry

A Hele-Shaw cell is a quasi-2D geometry where fluid is confined between two plates whose spacing b is much less than their lateral dimensions (fig. 2.1) [49]. Several variations of the Hele-Shaw geometry exist. We will be-

gin by discussing the the channel geometry, where fluid flows uniformly across the width of the channel. Other geometries will be discussed later, but the underlying physics is essentially identical. For the channel, we use the coordinate system as shown in fig. 2.1; x and y are the in-plane coordinates (across the width and length, respectively) and z is the coordinate across the gap.

The equations of motion for fluid in a Hele-Shaw cell are derived by starting with the equations for incompressible viscous fluid flow, $\boldsymbol{\nabla} \cdot \boldsymbol{u} = 0$ [68, p. 17] and $\rho\, \partial \boldsymbol{u}/\partial t = -\boldsymbol{\nabla} P + \mu \nabla^2 \boldsymbol{u}$ (Stokes' equation [68, pp. 46, 58]), where $\boldsymbol{u}$ is the fluid velocity, P is the pressure, ρ is the fluid density, and μ is the fluid's dynamic viscosity.

From Stokes' equation, the variation of the velocity in the vertical (z) direction is found to follow a Poiseuille (parabolic) flow profile [68, p. 52],

$$\boldsymbol{u}(z) = -\left(\frac{1}{2\mu}\boldsymbol{\nabla} P\right)\left(bz - z^2\right). \tag{2.1}$$

The average flow in the x-y plane is obtained by integrating the z-dependence out:

$$\begin{aligned} \int_0^b \boldsymbol{u}\,\mathrm{d}z &= -\left(\frac{1}{2\mu}\boldsymbol{\nabla} P\right)\int_0^b \left(bz - z^2\right)\mathrm{d}z \\ \langle \boldsymbol{u} \rangle\, b &= -\left(\frac{1}{2\mu}\boldsymbol{\nabla} P\right)(b^3/6) \\ \boldsymbol{u}(x,y) &= -\frac{b^2}{12\mu}\boldsymbol{\nabla} P(x,y) \end{aligned} \tag{2.2}$$

Equation 2.2 is identical to Darcy's law for the flow of fluid through

porous media,

$$\boldsymbol{u} = -\frac{\kappa}{\mu}\boldsymbol{\nabla} P, \tag{2.3}$$

where κ is the permeability of the porous medium, provided $b^2/12$ is taken as the effective permeability of the Hele-Shaw cell.

The underlying physical reason that both porous media and the Hele-Shaw geometry have the same equations of motion is that both are dominated by viscous drag; drag against the solid part of the material for porous media and against the plates for the Hele-Shaw geometry.

Applying the additional incompressibility condition, $\boldsymbol{\nabla} \cdot \boldsymbol{u} = 0$, we obtain Laplace's equation for the pressure field, $\nabla^2 P = 0$. Because this equation underlies the dynamics, viscous fingering is more generally known as Laplacian growth.

Laplace's equation is of course quite generic to many situations. The substance of the problem then lies in the boundary conditions. The time dependence arises from the kinetic boundary condition ([109], p. 24): $\boldsymbol{v}_{\text{interface}} \cdot \hat{\boldsymbol{n}} = \boldsymbol{u}_{\text{fluid}} \cdot \hat{\boldsymbol{n}}$, where $\hat{\boldsymbol{n}}$ is the unit normal vector at the interface. This simply tells us that the interface moves with the local fluid motion. The other boundary condition is the dynamic boundary condition for the pressure difference across the interface. For fully 3D problems, this is ([68], p. 239)

$$\delta P\Big|_{\text{interface}} = \sigma \ (\kappa_1 + \kappa_2)\,, \tag{2.4}$$

where σ is the surface (interfacial) tension between the two fluids, and κ_1 and κ_2 are the two principle curvatures at each point on the interface. This

condition (and its nonlinearity) introduces most of the analytical difficulties in this problem. Because of that, many early analyses neglected surface tension ($\delta P\Big|_{\text{interface}} = 0$), but this introduces additional complications because the $\sigma \to 0$ limit is singular [139, 59, 61]. (This is not immediately obvious and is still in dispute in some circumstances [92, 125, 90, 20, 2, 91].)

The analyses of this problem always exploit the two dimensional nature of the problem, so this boundary condition must be simplified to fit into that framework. The most common form assumed is

$$\delta P\Big|_{\text{interface}} = \sigma \left(\frac{2}{b} + \frac{1}{R} \right), \tag{2.5}$$

where R is the radius of curvature in the x-y plane. While the $2/b$ term is much larger than the in-plane curvature $1/R$, it is constant everywhere on the interface and will drop out of any analyses. Thus this is further reduced to

$$\delta P\Big|_{\text{interface}} = \sigma/R. \tag{2.6}$$

Though the gap thickness b is constant, it can be effectively reduced by oil left on the top and bottom plates. The effects of this remaining film of oil are discussed in sec. 2.4.3.

The relative importance of the role of surface tension in the problem is generally expressed via the capillary number, a non-dimensional number relating the strength of the viscous forces to surface tension forces: $\text{Ca} = \mu V/\sigma$, where V is the interface velocity.

Park and Homsy [105] and even Saffman and Taylor [122] point out that even though eqn. 2.5 seems naturally implied from the static formulas, it

is in fact an assumption. By carefully examining the fully 3D moving interface problem for a completely wetting fluid for small Ca and large w/b, Park and Homsy [105] found instead

$$\delta P\Big|_{\text{interface}} = \sigma \left(\frac{2}{b} + \frac{\pi}{4} \frac{1}{R} \right). \tag{2.7}$$

The additional factor of $\pi/4$ arises from considerations involving the motion of the interface; the pressure boundary condition for a moving interface is not identical to those for a static interface. (The Ca $\to 0$ limit is not completely regular, though it is not as singular as the Ca $\to \infty$ limit, which will be discussed later.) This essentially means that the fluid interface within a Hele-Shaw cell has an effective surface tension $\sigma_{\text{eff}} = \frac{\pi}{4}\sigma$. (A significant amount of later work ignores this factor of $\pi/4$, despite experimental evidence for it [104].)

Since our work was done exclusively with air and silicone oil, the analyses presented assume the viscosity of the air is negligible. (Even for our least viscous silicone oil, $\mu_{\text{oil}}/\mu_{\text{air}} \approx 550$.) The more general (fluid-fluid) case results either follow similarly or can be found in Couder [37].

2.3 Stability of Moving Interfaces

While a flat interface between the fluids moving at constant velocity is always a solution of these equations, the interface is only stable when the more viscous fluid displaces the less viscous fluid. The instability can be understood quite simply in the case where the viscosity of the less viscous fluid is negligible. If the interface has a small bump in the direction of motion,

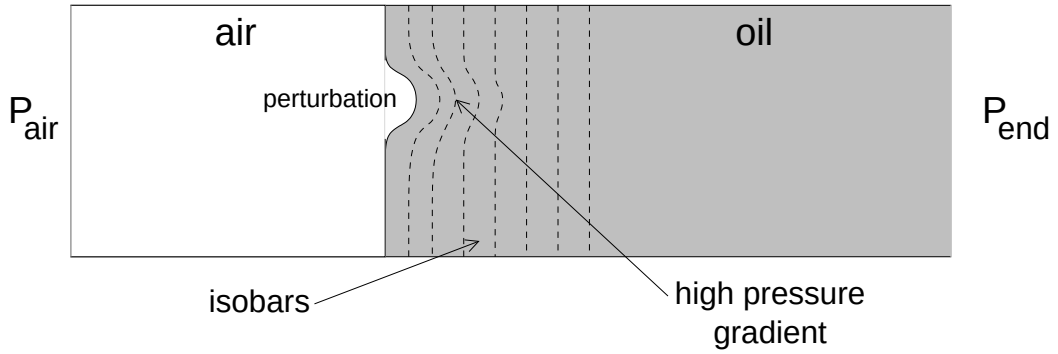

Figure 2.2: The instability of the interface can be easily explained qualitatively by examining how a forward perturbation of the interface must crowd the isobars in the viscous fluid together, creating a higher pressure gradient there. By Darcy's Law, the fluid will then move faster there than at the rest of the interface, further enlarging the perturbation.

the isobars in front are slightly crowded, creating a higher pressure gradient (see fig. 2.2). Since the velocity of fluid motion is proportional to the pressure gradient, the bump will move faster than the rest of the interface and leave it behind. Similarly, any backwards bump will stretch the isobars in front of it, lowering the pressure gradient and slowing fluid there down. This bump will move slower than the interface and will fall behind. Any perturbation of the interface will thus clearly grow and distort the flat interface.

To examine quantitatively the stability of the flat interface, I will present the linear stability analysis of the flat interface solution. This parallels the derivations given in Couder's review [37]. (Couder does the case with two viscous fluids; we assume the viscosity of the invading fluid is negligible. This result is the same as setting $\mu_1 = 0$ in Couder's analysis.)

We consider an initially flat interface separating a region of air and

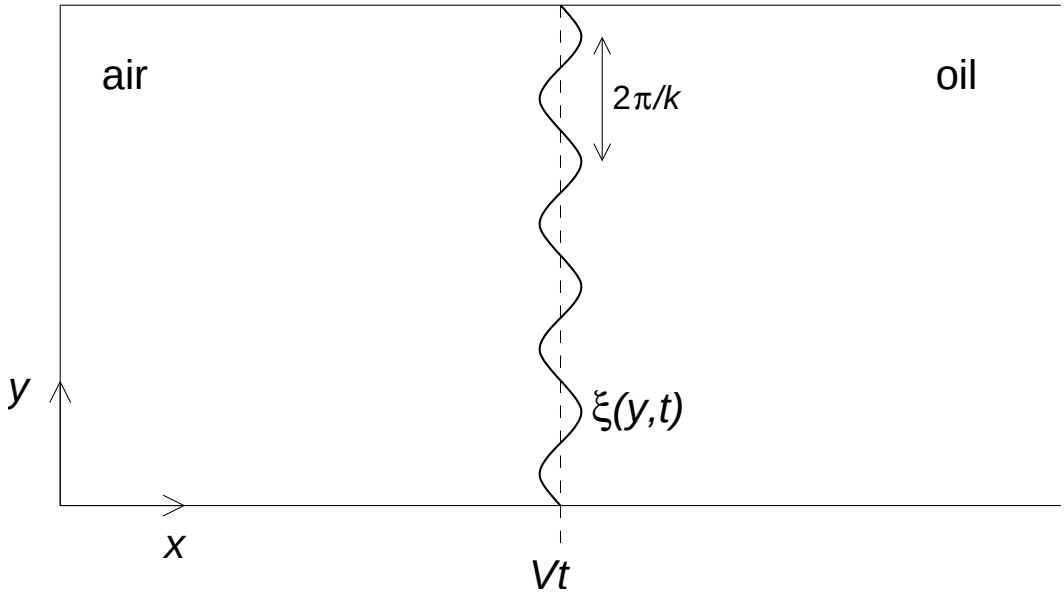

Figure 2.3: Definitions of the axes and variables for the linear stability analysis performed in the text. (Modelled after fig. 4 in Couder [37].)

oil. The interface runs parallel to the y-axis and moves in the x direction with velocity V. We consider the interface to have infinite extent in the y direction (i.e., we do not consider the effects the side boundary of the cell on the interface). We begin with our fundamental equations,

$$\boldsymbol{u} = \frac{-b^2}{12\mu}\boldsymbol{\nabla} P, \qquad \nabla^2 P = 0. \tag{2.8}$$

The flat interface base state is described by $\boldsymbol{u}_0 = V$, which immediately implies

$$P_0 = \frac{-12\mu V}{b^2}(x - Vt). \tag{2.9}$$

We then examine small perturbations from this base state:

$$P = P_0 + \delta P, \tag{2.10}$$

$$\boldsymbol{u} = \boldsymbol{u}_0 + \delta \boldsymbol{u}. \tag{2.11}$$

The interface position (see fig. 2.3) will be described by its x-coordinate, given by

$$\xi(y,t) = Vt + \epsilon \mathrm{e}^{\gamma t} \sin ky, \tag{2.12}$$

where ϵ is small.

To satisfy Laplace's equation, the solutions will have the form

$$\delta P = P(x,t) \sin ky = A\mathrm{e}^{\gamma t - kx} \sin ky. \tag{2.13}$$

(The e^{+kx} solution is excluded by the boundary condition at $+\infty$; we expect the perturbation to be small far from the interface.) We can find the constant A by considering the kinematic boundary condition. For small deformations,

$$\boldsymbol{u} \cdot \hat{\boldsymbol{n}} = \delta u_x(y) = \frac{\partial \xi}{\partial t} - V \tag{2.14}$$

at the interface. Thus

$$\left. \frac{-b^2}{12\mu} \frac{\partial(\delta P)}{\partial x} \right|_{x=\xi} = \delta u_x(y) = \epsilon\gamma \mathrm{e}^{\gamma t} \sin ky, \tag{2.15}$$

which gives

$$\delta P = \frac{12\mu\epsilon\gamma}{b^2 k} \mathrm{e}^{\gamma t} \mathrm{e}^{-k(x-Vt)} \sin ky. \tag{2.16}$$

We apply the dynamic boundary condition by first noting that, because we are neglecting the viscosity of the air, $P_{\mathrm{air}} = \text{constant}$, which can be taken

to be zero without a loss of generality. Thus the pressure difference at the interface is

$$P_{\text{oil}} - P_{\text{air}} = \Delta P\Big|_{x=\xi} = \sigma\kappa, \tag{2.17}$$

where κ is the curvature of the interface (using the simplest standard form for the surface tension term). Then to first order,

$$P\Big|_{x=\xi} = \sigma\frac{\partial^2\xi}{\partial y^2}. \tag{2.18}$$

Combining equations 2.9, 2.10, 2.12, and 2.16, we have

$$P\Big|_{x=\xi} = \frac{-12\mu V}{b^2}\left(\xi(y,t) - Vt\right) + \frac{12\mu}{b^2}\frac{\epsilon\gamma}{k}\mathrm{e}^{\gamma t}\mathrm{e}^{-k(\xi(y,t)-Vt)}\sin ky. \tag{2.19}$$

From eqn. 2.12, we also immediately have

$$\xi(y,t) - Vt = \epsilon\mathrm{e}^{\gamma t}\sin ky, \tag{2.20}$$

from which we have

$$\sigma\frac{\partial^2\xi}{\partial y^2} = -\sigma k^2\epsilon\mathrm{e}^{\gamma t}\sin ky. \tag{2.21}$$

Substituting eqn. 2.20 into eqn. 2.19 and only keeping terms that are first order in ϵ, then equating with eqn. 2.21, we get

$$-\sigma k^2\left\{\epsilon\mathrm{e}^{\gamma t}\sin ky\right\} = \frac{-12\mu V}{b^2}\left\{\epsilon\mathrm{e}^{\gamma t}\sin ky\right\} + \frac{12\mu}{b^2}\frac{\gamma}{k}\left\{\epsilon\mathrm{e}^{\gamma t}\sin ky\right\}, \tag{2.22}$$

which reduces to

$$-\sigma k^3 = \frac{-12\mu Vk}{b^2} + \frac{12\mu}{b^2}\gamma, \tag{2.23}$$

finally giving

$$\gamma = Vk - \frac{b^2\sigma}{12\mu}k^3. \tag{2.24}$$

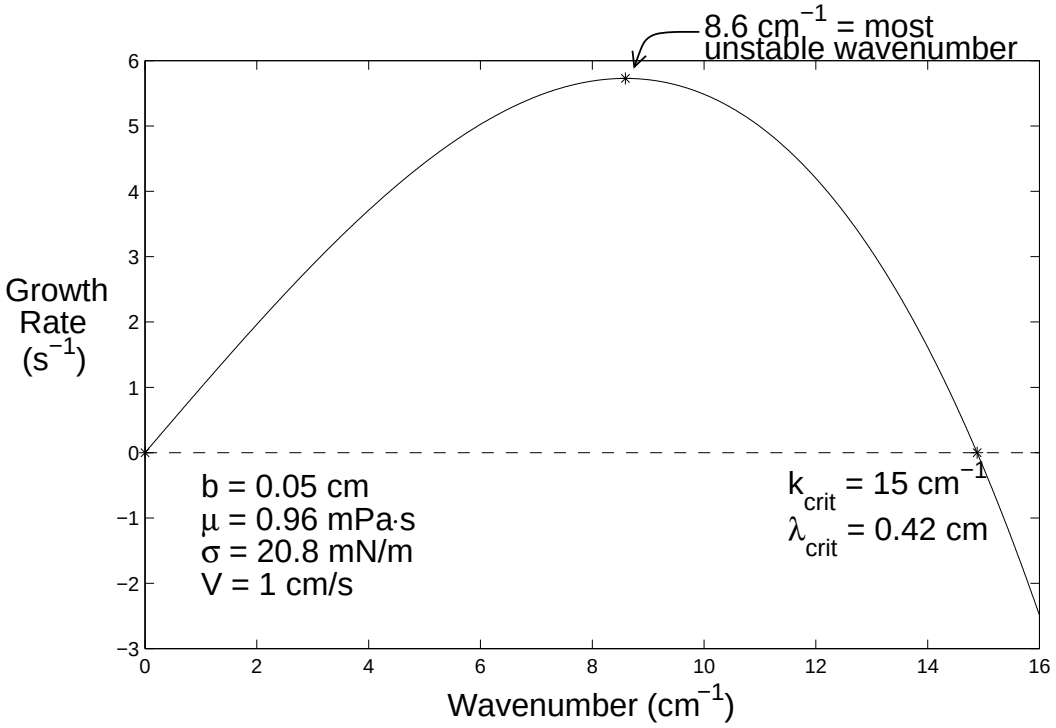

Figure 2.4: A graph of the dispersion relation (growth rate *vs.* wavenumber) for small perturbations of the interface. The parameters used are typical for the experimental work described here.

The growth rate γ is always negative for $V < 0$; the flat interface is always stable when pushing a more viscous fluid into a less viscous one. For $V > 0$, γ has a maximum for wavenumber

$$k_{\max} = \frac{2}{b}\sqrt{\mathrm{Ca}}, \tag{2.25}$$

where $\mathrm{Ca} = \mu V/\sigma$ is the capillary number, a non-dimensional number relating the strength of the viscous pressure gradient to surface tension forces. Modes with wavenumber greater than

$$k_{\mathrm{crit}} = \sqrt{3}k_{\max} \tag{2.26}$$

are suppressed, as we might expect; surface tension suppresses modes having short wavelengths and hence high curvature.

The wavelength corresponding to the critical wavenumber, $\lambda_{\text{crit}} = \pi b/\sqrt{3\,\text{Ca}}$, is often called the capillary length. ($\lambda_{\text{crit}} \simeq 4$ mm for the parameter values in fig. 2.4; this is about 8 times the gap thickness b.) It is also occasionally called the Mullins-Sekerka length after the essentially identical result found by Mullins and Sekerka [100] for the instability of a solidification front.

The dispersion relation (eqn. 2.24) is also often expressed in terms of a different non-dimensional number frequently called the Modified Capillary Number, which is

$$1/B = 12\,\frac{\mu V}{\sigma}\left(\frac{w}{b}\right)^2. \tag{2.27}$$

The notation is a historical artifact; the parameter B was first developed by theorists who like to think of this as a non-dimensional surface tension, but then later $1/B$ was adopted by experimentalists who prefer to have the controllable parameter V in the numerator.

Many variations of the latter parameter occur in the literature, differing primarily by numeric factors of $(2\pi)^2$, etc., though some researchers have used the velocity at infinity instead of the velocity of the finger tip. For a constant velocity single finger, this introduces factors of the relative finger width λ; the relationship is not simple when secondary instabilities are occurring. (Arguments can be made for either choice: V_∞ is constant while the finger velocity may not be, but the finger velocity is often much more easily measured. We use the latter velocity.)

Tabeling, Zocchi, and Libchaber [135] argue that the critical $1/B$ (the minimum to have an instability) occurs when the critical wavelength equals the channel width, $\lambda_{\text{crit}} = w$, which gives $1/B_{\text{crit}} = 4\pi^2$. This would be acceptable for periodic boundary conditions (often assumed in theoretical work), but all experiments have the boundary pinned at the sides of the channel. I therefore reason that $\lambda_{\text{crit}}/2 = w$ is more sensible, which gives $1/B_{\text{crit}} = \pi^2$. This is more consistent with Tabeling, Zocchi, and Libchaber's own observations, as they report finger widths less than one for $1/B \gtrsim 5$. (We have observed fingers down to $1/B = 13.1$ for $w/b = 58.4$; this finger was 91% of the channel width and moved at 0.13 mm/s.)

Park, Gorell, and Homsy [104] attempted experimentally to verify this dispersion relation (eqn. 2.24) and obtained reasonable agreement for a moderate range of Ca, though the data were noisy. They obtained better agreement, particularly for the cut-off wavelengths, when they used the effective surface tension described earlier, $\sigma_{\text{eff}} = \frac{\pi}{4}\sigma$. Experimental limitations, particularly effects due to the pinning of the interface at the beginning of the channel, created greater differences at low Ca.

2.4 Single Finger Regime

After the linear stage of growth, the forward sections of the advancing front elongate into long fingers, which then interact and compete. Saffman and Taylor [122] observed that a single finger will ultimately win out and propagate steadily down the center of the channel with a fixed width. The finger width

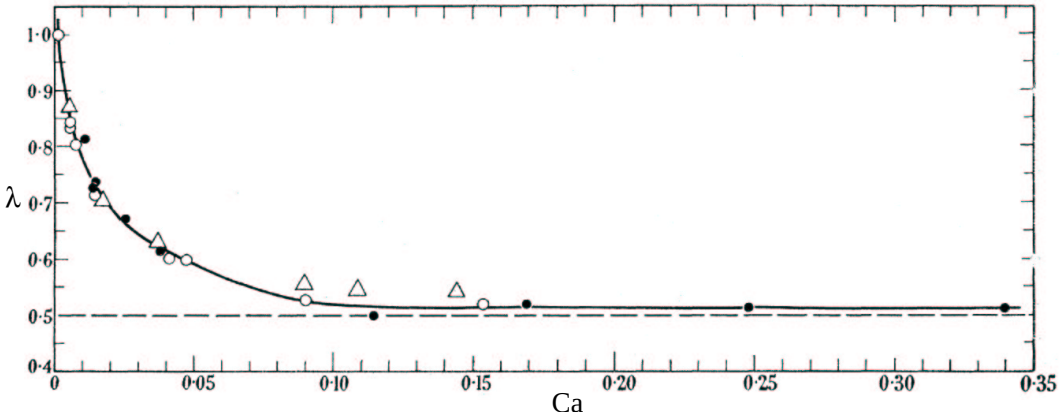

Figure 2.5: Saffman and Taylor's [122] original experimental results for the relative width of single fingers λ *vs.* the capillary number Ca. The results are for a single aspect ratio, $w/b = 32$, for water penetrating various oils ($\triangle$ & $\circ$, 30 mPa $\cdot$ s; $\bullet$, 450 mPa $\cdot$ s). The solid line is merely a guide to the eye.

is described by the parameter λ, defined as the ratio of the finger width to the channel width. They found that the single finger was nearly the width of the channel (λ just under 1) at low Ca but quickly dropped off to $\lambda \approx 1/2$ as Ca increased, as shown in fig. 2.5. They did not observe fingers with $\lambda < 1/2$.

For the case of a single, infinitely long finger steadily propagating in the absence of surface tension, Saffman and Taylor used conformal mapping techniques to obtain a solution for the shape:

$$x = \frac{w(1-\lambda)}{\pi} \ln\left\{\cos\left(\frac{\pi y}{w\lambda}\right)\right\}, \tag{2.28}$$

where the relative finger width λ enters as a free parameter (in the range 0 to 1). Further analysis by Taylor and Saffman revealed a set of asymmetric

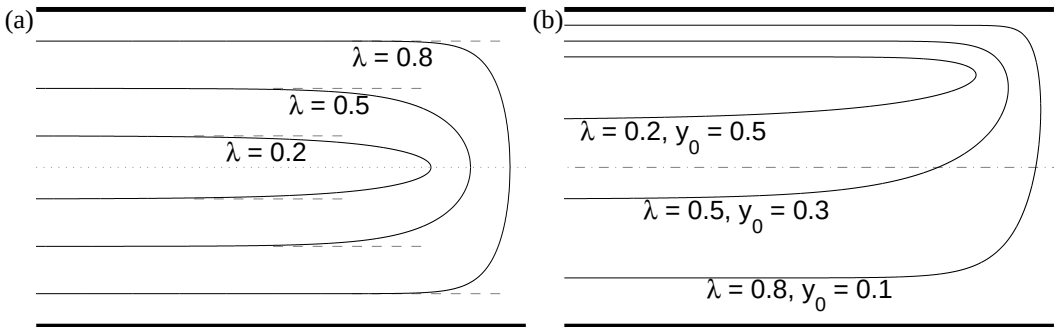

Figure 2.6: a) The symmetric finger shape calculated without surface tension (eqn. 2.28) for various values of the width λ. (Modelled after fig. 7 in Saffman and Taylor [122]). Without surface tension, λ can take any value from 0 to 1. Pitts's finger shapes (eqn. 2.30) are identical to Saffman and Taylor's $\lambda = 0.5$ finger, re-scaled to the appropriate width. b) The asymmetric finger shape calculated without surface tension (eqn. 2.29) for various values of λ and y_0. Without surface tension, λ and y_0 can take any value from 0 to 1, provided $\lambda + |y_0| < 1$.

solutions as well [140]:

$$x = \frac{w(1-\lambda)}{\pi} \ln\left\{\cos\left(\frac{\pi(y-y_0)}{w\lambda}\right)\right\} + \frac{wy_0}{\pi} \ln\left\{\tan\left(\frac{\pi}{4} + \frac{\pi(y-y_0)}{2w\lambda}\right)\right\}, \tag{2.29}$$

where both λ and y_0 enter as free parameters (in the range 0 to 1, with the constraint that $\lambda + |y_0| < 1$). These asymmetric solutions reduce to the symmetric solutions for $y_0 = 0$. The complete family of solutions is thus described by two continuous parameters. Profiles for various values of λ and y_0 are shown in fig. 2.6.

However, these solutions could not predict what finger width would actually appear, including why the finger was always centered ($y_0 = 0$) , why

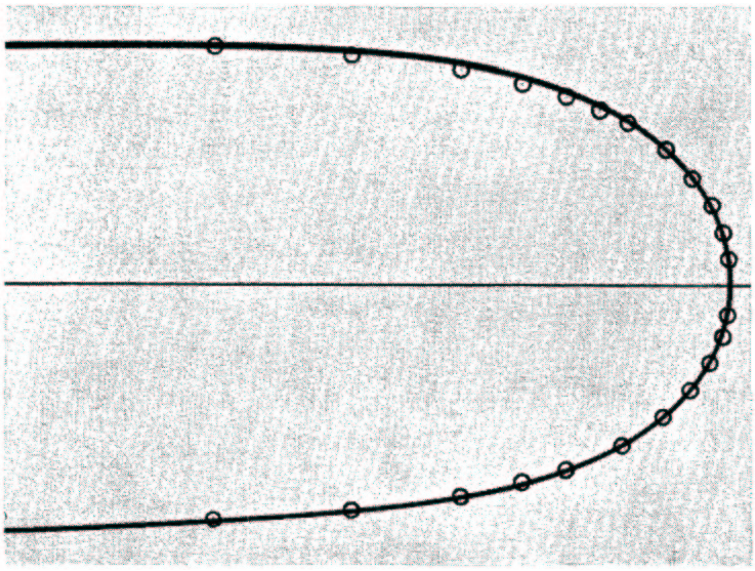

Figure 2.7: An experimental half width finger with the theoretical profile (eqn. 2.28) for $\lambda = 1/2$ superimposed (circles). From Saffman and Taylor [122].

$\lambda \approx 1/2$ was so common, or why $\lambda < 1/2$ was never observed.

Also, the finger shape thus obtained agreed well with the observed finger shape for finger widths near 1/2 (fig. 2.7), but disagreed for much wider fingers (fig. 2.8) [122].

Pitts [114] later found a different set of solutions:

$$x = \frac{w\lambda}{\pi} \ln \left\{ \cos \left(\frac{\pi y}{w\lambda} \right) \right\}, \tag{2.30}$$

but to do so he used what even he admitted was a physically unjustified starting assumption. They also cannot predict λ, but they do in fact fit the observed finger profile well for fingers with $0.5 < \lambda < 0.85$! These fingers have the same form as the Saffman-Taylor finger at $\lambda = 1/2$ and are self-similar;

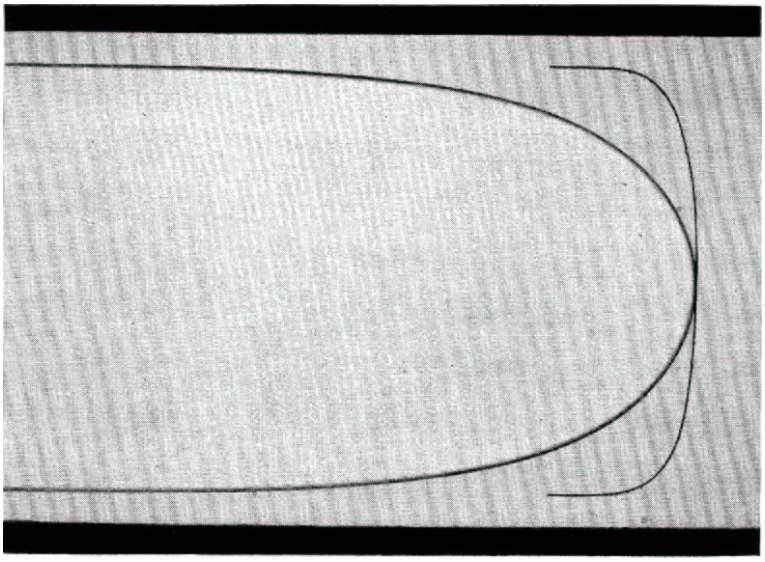

Figure 2.8: An experimental finger with $\lambda = 0.87$. Drawn in front is the theoretical profile for $\lambda = 0.87$, revealing a large disagreement. From Saffman and Taylor [122].

in other words, they are the Saffman-Taylor half width finger re-scaled to the appropriate width λ. Why these solutions match the experiment so well has never (to my knowledge) been explained.

Finally, Tabeling, Zocchi, and Libchaber reported that the tip shape became a semi-circle for $1/B < 50$, which gave them $\lambda > 0.85$ [135].

2.4.1 Selection of Finger Width

While theories without surface tension make no prediction for the width of the steady finger, the experimental system adopts a single symmetric finger with a well defined width at a given modified capillary number. Trying to explain this became known as the "selection problem", which remained unsolved

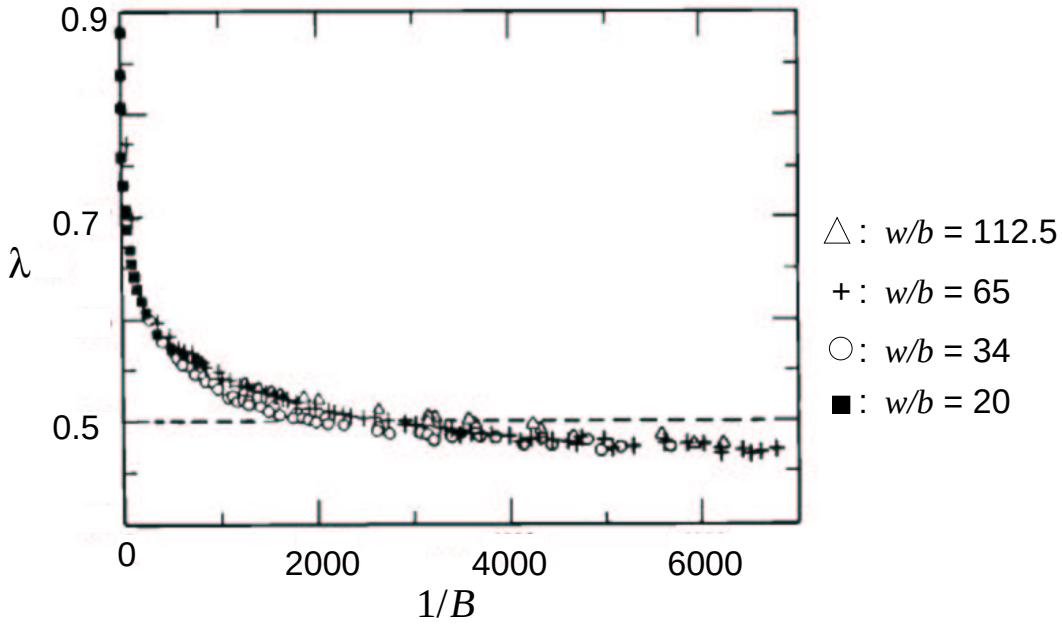

Figure 2.9: Tabeling, Zocchi, and Libchaber's [135] results for finger width λ *vs.* $1/B$ for various aspect ratios w/b. Their curves do not superpose exactly and fall slightly below $\lambda = 1/2$ at large $1/B$.

for almost twenty years.

The most definitive experimental work on the behavior of single fingers this was done by Tabeling, Zocchi, and Libchaber [135]; their experimental results are shown in fig. 2.9. Unlike Saffman and Taylor's results, their data do not collapse exactly onto a single curve. Also, their results at large $1/B$ fall slightly below $\lambda = 1/2$ and do not exhibit a clear plateau. These differences are generally ascribed to effects of the film of oil left behind on the plate, which I discuss further below.

To solve the "selection problem" and explain why single steady fin-

gers had the observed width and shape, a great deal of analytic work was required [86, 85, 28, 29, 52, 130, 142], aided by numerical simulations [41, 126, 127]. The difficulties arose because the problem of an infinitely long finger propagating steadily down a channel in the absence of surface tension turns out to be structurally unstable (Tanveer, Siegel, Magdaleno, Casademunt) [139, 132, 131, 77, 21, 108, 78]. In other words, perturbing that problem in some way (by adding surface tension, examining finite channel length effects, etc.) will drastically change the solutions even if the perturbation is arbitrarily small. Thus adding surface tension (which was believed to be the mechanism for the width selection) cannot be done using standard perturbation theory; surface tension enters the problem as a singular perturbation [139, 59, 61].

Specifically, including surface tension introduces transcendentally small terms in the formula for the interface shape. These terms will not appear in any regular perturbation expansion, hence this approach is often referred to as "asymptotics beyond all orders" [139, 59]. However, these terms create a physically unallowable cusp at the tip except for particular values of the width [61]. This thus introduces a constraint (a "solvability condition") that reduces the continuous family of symmetric solutions to a countably infinite set. These solutions give the finger width λ as a function of $1/B$ alone [37]. Some of these finger width solutions are shown in fig. 2.10. A similar singular perturbation analysis of the asymmetric Saffman-Taylor solutions gives a solvability condition that can never be satisfied [136, 27]; including surface tension thus eliminates them from consideration.

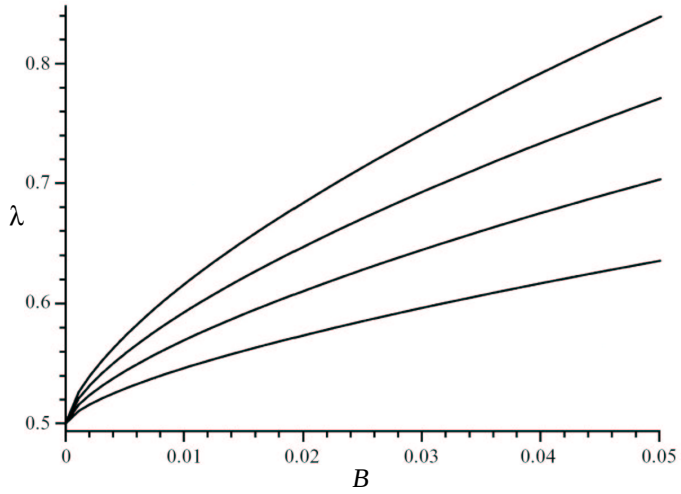

Figure 2.10: The first three branches of analytic solutions for finger width *vs.* B. Only the lowest branch is stable. From Vanden-Broeck [142] (through Tanveer [139]).

All of these functions are monotonic, with $\lambda \to 1/2^+$ as $1/B \to \infty$ and $\lambda \to 1$ as $1/B \to 0$. The last piece of the "selection problem" puzzle was put into place by studying the stability of these branches: only the solution with the narrowest width at a given $1/B$ was stable [60, 136].

At large $1/B$, these functions follow the asymptotic relation $\lambda - 1/2 = a_n(1/B)^{-2/3}$, where a_n depends on the particular solution examined [28, 37]. (The value for the stable solution is $a_0 = 2.385$.) Numerical solutions are required for low and intermediate $1/B$. I am not aware of any asymptotic analytic formula for λ as $1/B \to 0$, though Tabeling, Zocchi, and Libchaber found empirically that $1 - \lambda = (0.011)(1/B)$ for $1/B < 20$. (Again, note that this is not consistent with their proposed cut-off value for the instability, $1/B_{\text{crit}} = 4\pi^2 \approx 40$ [135].)

Though the theory predicts a given value of λ for a particular $1/B$ for all aspect ratios w/b, the experimental data did not quite collapse onto a single curve for all values of w/b. Also, the experimental widths had λ drop below $1/2$ by a few percent (fig. 2.9). These differences are ascribed to the effects of film wetting on the dynamic boundary condition.

2.4.2 Dynamical Selection

There are a few who dissent from this conventional understanding of the selection of finger width [92, 1, 43]. They agree that surface tension is a singular perturbation in the asymptotic ($t \to \infty$) limit but state that it is not singular in the initial value problem (i.e., in the finite time domain). They therefore argue that zero surface tension solutions to the initial value problem may still describe the non-zero surface tension dynamics. At worst, they would expect the real dynamics to diverge from the zero surface tension dynamics only on long time scales of order $O(1/\sigma)$.

Others counter that the problem is still structurally unstable in the finite time domain, and that any solution to the zero surface tension problem must diverge from the correct dynamics in $O(1)$ time [132, 131, 77, 21, 108, 78].

Many solutions to the initial value problem without surface tension are ill-behaved, as shown in fig. 2.11. However, Mineev has found a set of solutions to this problem that remain well behaved for all time [92]. These solutions further have the interesting property that over time they will eventually evolve into the half-width finger of Saffman and Taylor.

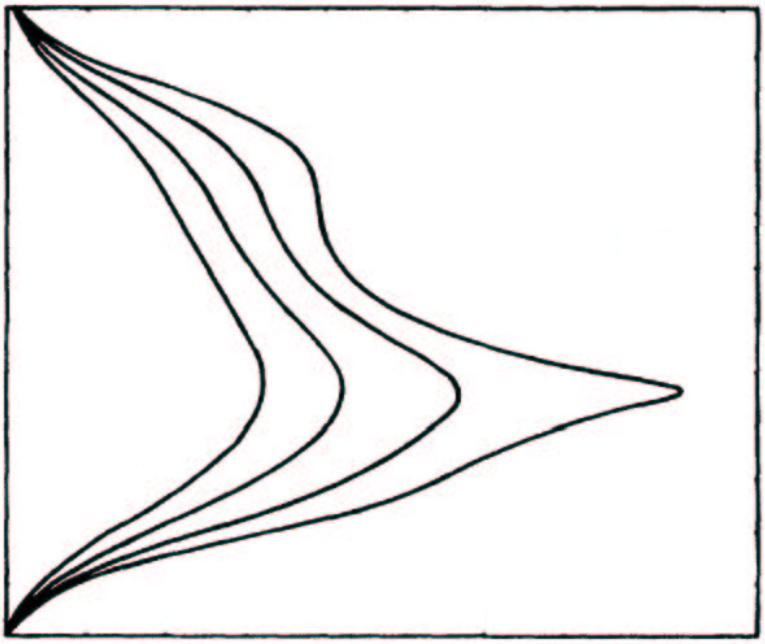

Figure 2.11: The evolution of an arbitrary initial interface in a simulation without surface tension. A cusp singularity is developed in finite time. From Bensimon *et al.* [13] (edited to remove extraneous detail).

These solutions are described (using the x and y coordinates as real and imaginary parts of a complex coordinate z) by

$$z(t,\phi) = \tau(t) + i\mu\phi + \sum_{k=1}^{N} \alpha_k \ln\left[e^{i\phi} - a_k(t)\right], \tag{2.31}$$

where $\mu = 1 - \sum_{k=1}^{N} \alpha_k$, α_k = constant and $|a_k| < 1$. The time evolution of a_k and τ can be found from

$$\beta_k = \tau - \left(1 - \sum_{l=1}^{N} \alpha_l\right) \ln \bar{a}_k + \sum_{l=1}^{N} \ln\left(\frac{1}{\bar{a}_k} - a_l\right) = \text{constant}, \tag{2.32}$$

$$t + C = \left(1 - \frac{1}{2}\sum_{k=1}^{N} \alpha_k\right)\tau + \frac{1}{2}\sum_{k=1}^{N} \alpha_k \ln(a_k). \tag{2.33}$$

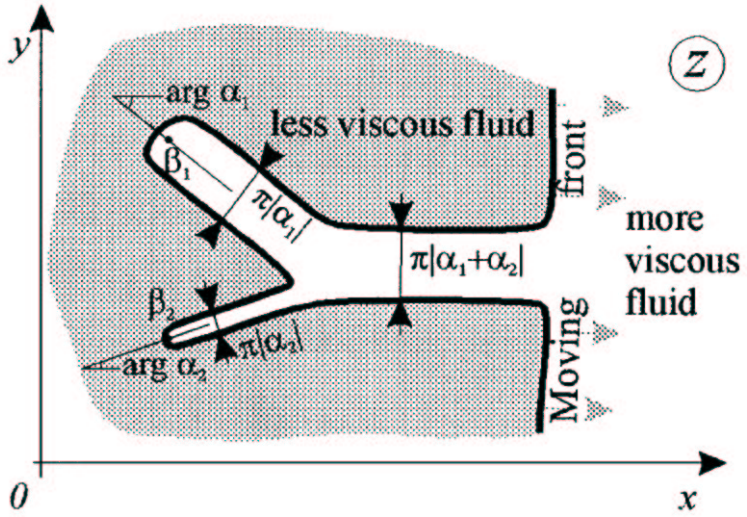

Figure 2.12: Geometrical interpretation of the complex constants of motion α_k and β_k ($k = 1, \ldots, N$): $\beta_k - \alpha_k \ln 2$ is the location of the k^{th} stagnation point. At that point, a "fjord" with parallel walls starts, having width $\pi|\alpha_k|$ and making an angle with respect to the horizontal axis $\arg \alpha_k$. From Mineev [92].

These solutions describe the evolution of N fingers over time. A simple geometrical interpretation of the constants α_k and β_k can be seen in fig. 2.12.

The set of these solutions have non-zero measure within the space of solutions to the zero surface tension problem [93]. Mineev states that "They describe tip splitting, side-branching, competition, coarsening, and screening of growing fingers which are observed in all known experiments and simulations." [92]. Mineev further believes that these solutions can accurately describe the non-zero surface tension dynamics arbitrarily closely [89].

Others disagree: As Magdaleno and Casademunt [77] explain, "We do not question the validity of the analytical results of Mineev [92] but the conclusions drawn concerning the dynamical role of surface tension. . . . the

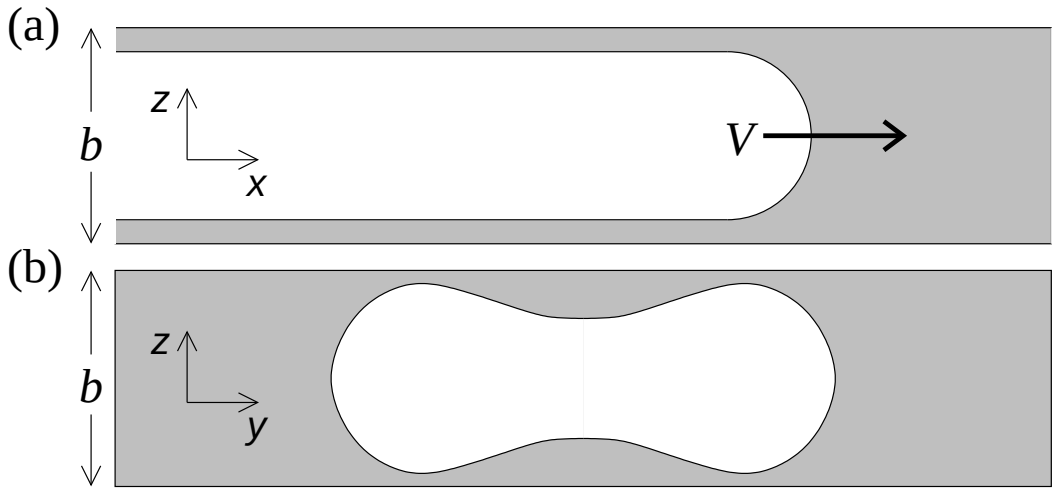

Figure 2.13: (a) Illustration of a side view of an advancing finger, showing thin film left behind on the plates. (b) Illustration of a front view of an advancing finger. The thickness of the film is an increasing function of the normal velocity of the interface, so the film is thickest at the center of the finger and thinnest at the sides. The amount of variation in thickness is exaggerated for clarity.

dynamics leading to $\lambda = 1/2$ need not be close to the physical one."

This debate is still ongoing. In sections 7.2 and 8.1 we will briefly discuss how we have attempted to address these issues experimentally.

2.4.3 Film-wetting Corrections

In most experiments, oils and other fluids that wet glass are used as the more viscous, displaced fluid. These fluids then leave a film on the top and bottom plates (as illustrated in fig. 2.13). If this film has a constant thickness, this reduces the effective gap thickness but otherwise the vertical curvature can again be ignored. However, even small differences in the film thickness can have significant effects because the vertical curvature is so large.

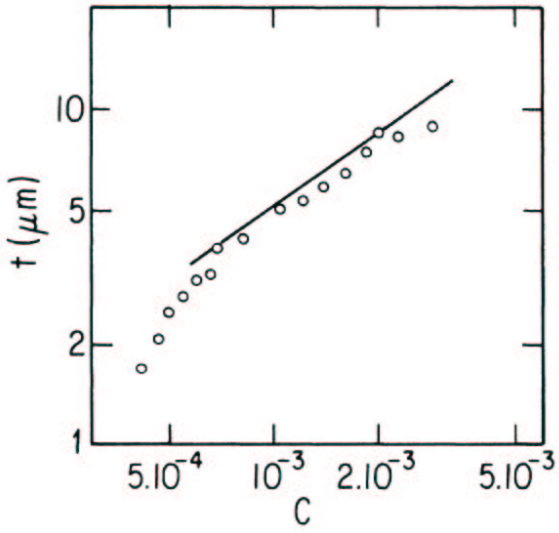

Figure 2.14: The maximum mean thickness of the films *vs.* the capillary number. The straight line corresponds to the Bretherton calculation [19]. Measured by Tabeling and Libchaber [134] using interferometry.

The first order corrections for the effects of the variations of film thickness are based on Bretherton's work on the fluid layer near the walls for a large bubble rising in a capillary tube. For this system he found that the layer thickness depended on the normal velocity of the interface there; the layer thickness t was proportional to $(\mathrm{Ca})^{2/3}$ for a moderate range of Ca [19]. Using interferometry, Tabeling and Libchaber [134] experimentally verified the applicability of this relation to fluids in Hele-Shaw cells, though only for a single aspect ratio $w/b = 66.3$ (see fig. 2.14). They also observed that this relation broke down at both high and low Ca, and they proposed empirical extensions of this relation for high Ca [135].

This means that the film thickness will also vary along the finger profile;

it will be thickest behind the tip, where the normal velocity was greatest, and thinnest at the sides (as in fig. 2.13(b)). The problem is thus fully three dimensional.

Park and Homsy [105] started with the Bretherton relation in their analysis of the fully three dimensional interface problem and obtained additional corrections as a function of Ca and w/b. Their results were later extended to a wider range of parameters by Reinelt [120]. Tabeling and Libchaber [134] applied Park and Homsy's result to the single finger case by averaging over the interface shape to create an effective surface tension

$$\sigma^* = \sigma \left[\frac{\pi}{4} + \alpha\lambda \left(\frac{w}{b} \right) (\mathrm{Ca})^{2/3} \right], \tag{2.34}$$

where λ is again the relative finger width and α is a constant ≈ 1.7. By applying this correction to their finger width data, they obtained reasonable agreement between the theoretical curve and the experimental data for $1/B < 200$, which before had differed by at least 10% (as shown in fig. 2.15).

Corrections for film wetting in different regimes were studied extensively by Tanveer [137, 138]. Detailed comparison between his results and experiments have not been performed, but they roughly account for the small amount of narrowing below 1/2 seen for fingers at high $1/B$. Tanveer predicts that fingers significantly narrower than 1/2 could be obtained due to these effects, but the conditions necessary to reach the regime where these predictions apply would be difficult to reach experimentally. It would require reaching values of $1/B \gtrsim 20,000$ for reasonable aspect ratios ($w/b \sim 250$), which is well

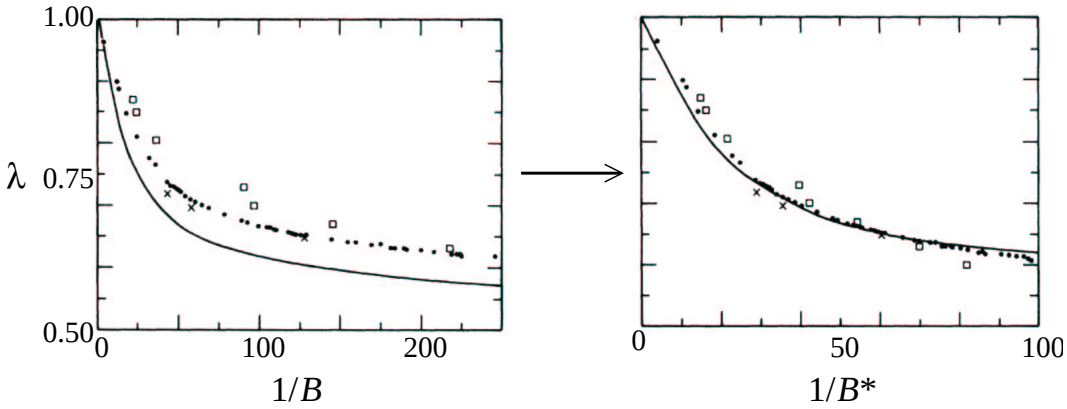

Figure 2.15: The comparison between theory (solid lines) and experiments (symbols) before (left) and after (right) applying Tabeling and Libchaber's results for an effective surface tension which includes effects of the variations in film thickness [134]. □, data from Saffman and Taylor [122], $w/b = 31.8$; •, $w/b = 66.3$, $\mu = 9.3$ mPa · s; ×, $w/b = 62.3$, $\mu = 487$ mPa · s. The solid curve is the theoretical prediction of McLean and Saffman [85]. (Both graphs are from Tabeling and Libchaber [134].)

into the regime where the single finger is unstable in most systems.

In all of the work discussed here, the thickness of the top and bottom film have been taken as equal. Gravity can cause the thicknesses to become unequal; the magnitude of this effect is described by the Bond number $G = \rho g b^2/\sigma$, which is the ratio of gravitational forces to capillary forces. For essentially all experimental work, the Bond number has been small ($G \ll 1$), so the film asymmetry due to gravity is very small and its effects unimportant [109, 55].

2.5 Secondary Instabilities

At still higher flow rates, a sequence of secondary instabilities occurs. Analytically, the half width finger is linearly stable for all flow rates, no matter how large [60]. However, finite amplitude perturbations can generate secondary instabilities in a manner somewhat similar to the instabilities in fluid flows in pipes [68, sec. 28].

The instability of the system to finite perturbations can be understood by considering that the multiple branches of solutions all approach $\lambda = 1/2$ as B goes to zero. Since only the lowest branch is stable, any perturbation large enough to push the system across an unstable branch can radically change the behavior. The amplitude needed decreases as the difference between the solutions decreases; Bensimon [12] found that the magnitude of the perturbation required decreased faster than exponentially with decreasing B.

All of the observed instabilities can be thought of as variations on tip splitting (fig. 2.16), where a point on the tip suddenly falls behind (a stagnation point). The instability grows quickly, developing into a fjord behind two competing fingers. However, unless the stagnation point occurs exactly at the tip, there is a competition between the growth of the instability and the advection of instability back to the sides of the finger, where the growth rate drops to zero and features become frozen [59, 109].

While both the growth and advection rates increase with increasing finger velocity, the advection effect dominates at lower velocities. Stagna-

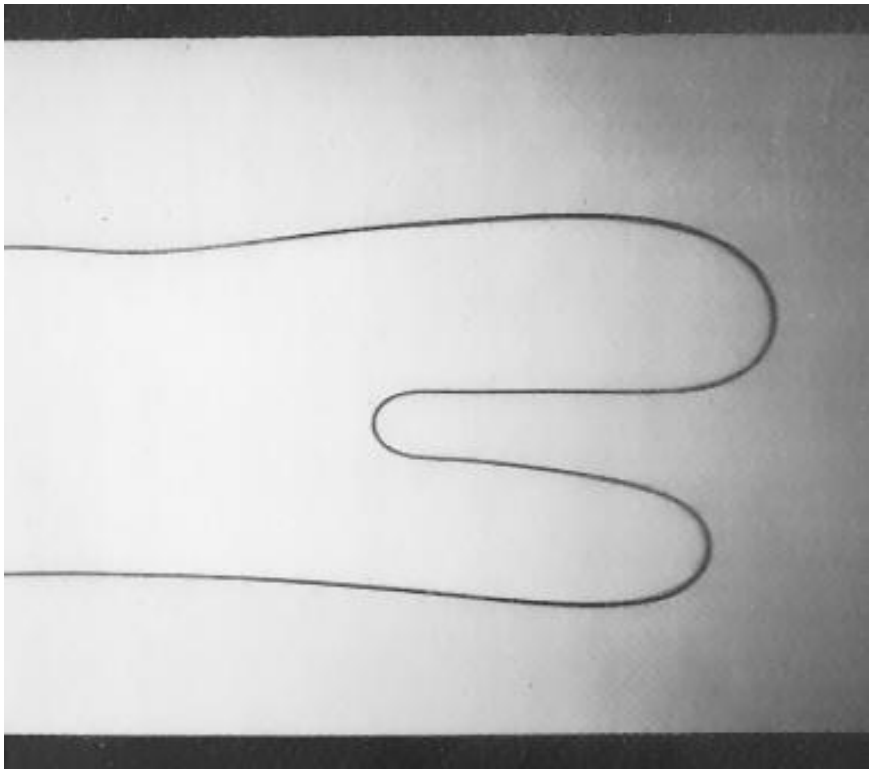

Figure 2.16: A close up view shortly after a tip splitting event. The two new fingers will compete (the upper one most likely winning), then the winning finger will grow wider until it becomes unstable again, allowing another tip splitting to occur. From Tabeling, Zocchi, and Libchaber [135].

tion points are advected to the sides of the finger before they grow enough to generate a fjord and two new fingers. This describes the first instability that appears, an asymmetric hump mode [13], shown in fig. 2.17. At higher speeds, the stagnation point is advected far enough towards a side that even though two fingers form, one of them is immediately suppressed by the other. (These events are sometimes called "side-branching" events, but this is inaccurate, as they are not at all comparable to side-branching events in dendritic growth [67, 109].) At still higher speeds, the growth of the instability dominates the advection effect and tip splitting with more equal secondary fingers are seen. These fingers then compete; the winning finger will shield the growth of the other finger and grow wide enough to be unstable to further tip splits [51]. Similar results have been obtained in numerical simulations [40, 41]. A pattern of such repeated tip splitting is shown in fig. 2.18. Maxworthy [80] and Kopf-Sill and Homsy [64] made some attempts to quantify the finger behavior in the repeated tip splitting regime, but otherwise little quantitative work has been done there.

The only experimental observations of finite perturbations to the system were of the effect of variations in the gap thickness b [135]. Tabeling, Zocchi, and Libchaber observed that decreasing the amount of variation in the gap thickness ($\delta b/b$) by an order of magnitude doubled the value of $1/B$ at which secondary instabilities began. They attempted to investigate the effects of other types of intentionally induced noise but obtained no conclusive results.

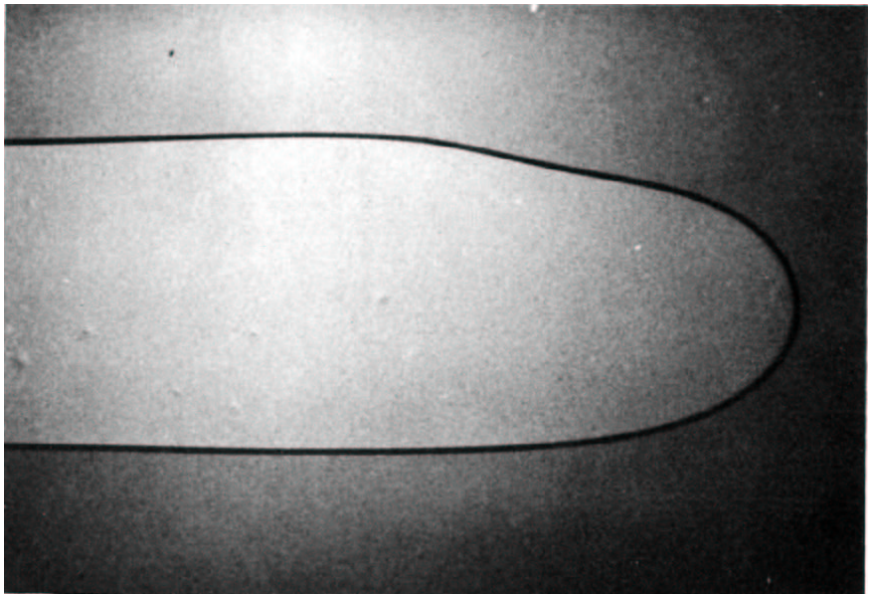

Figure 2.17: The first instability that appears as the modified capillary number is increased is an asymmetric hump mode. It is essentially a tip splitting event where the stagnation point was advected back too quickly to grow significantly. From Tabeling, Zocchi, and Libchaber [135].

Figure 2.18: A photograph showing a complex pattern of repeated tip splitting in a channel at $1/B = 3.3 \times 10^5$. The cell has width $w = 10$ cm and gap $b = 0.25$ mm. From Arnéodo *et al.* [4].

2.5.1 Anomalous Fingers

Because the mechanism governing the selection of finger width is very dependent on the behavior at the finger's tip, experimenters investigated what would happen if the tip were perturbed by a wire [149] or a bubble [35]. They found that the behavior could indeed be profoundly altered in such cases.

Fig. 2.19 shows a pair of fingers whose tip was perturbed by a small wire suspended in the channel at mid-height. The fingers are significantly narrower than half the channel width, and the finger can easily be moved off the center by placing the wire off-center. These fingers also remain stable until much higher flow rates; unperturbed fingers usually become unstable for $1/B < 7000$, but these fingers remain stable up to $1/B \sim 29000$!

The shapes of these fingers seem to match the analytic shapes calculated for zero surface tension by Saffman and Taylor (eqn. 2.28 for the symmetric shape). This is demonstrated more explicitly in fig. 2.20, where the shape of a finger perturbed with a bubble is compared against the Saffman-Taylor formula for $\lambda = 0.32$, as well as the empirical formula of Pitts. Unlike the fingers with $\lambda > 1/2$, the shape clearly matches the former, not the latter.

Bubbles at the tip can also drive new branching behavior. Fig. 2.21 shows fingers with branches created by pulsating or oscillating tips. In the former case, the branches grow after the tip has passed, making them true side branching events rather than imperfect tip splits.

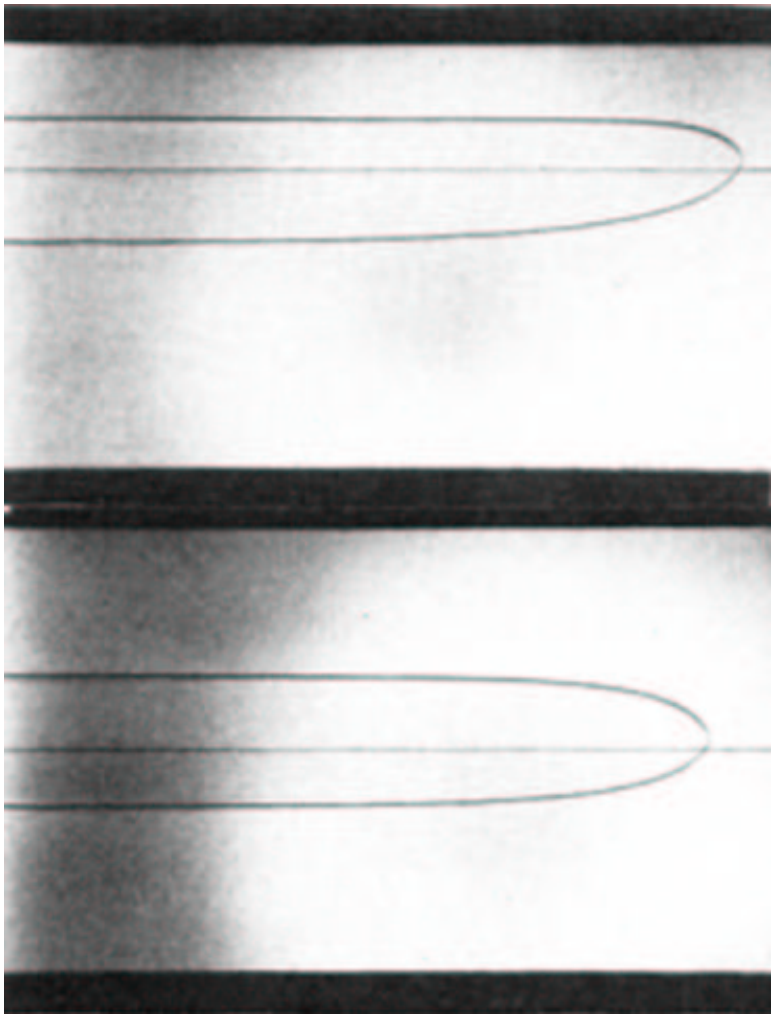

Figure 2.19: Steady state fingers of air penetrating into oil along wires in a cell of width $w = 5$ cm and gap $b = 0.8$ cm. (The wires have been retouched on the figure by the original authors.) Top: A nylon wire with a diameter of 117 μm is suspended inside the cell at mid-height. $1/B = 17200$, $\lambda = 0.296$. The shape is asymmetric because the finger is not moving in the middle of the channel. Bottom: A 13 μm thick tungsten wire is used. $1/B = 28300$, $\lambda = 0.300$. From Zocci, Shaw, Libchaber, and Kadanoff [149].

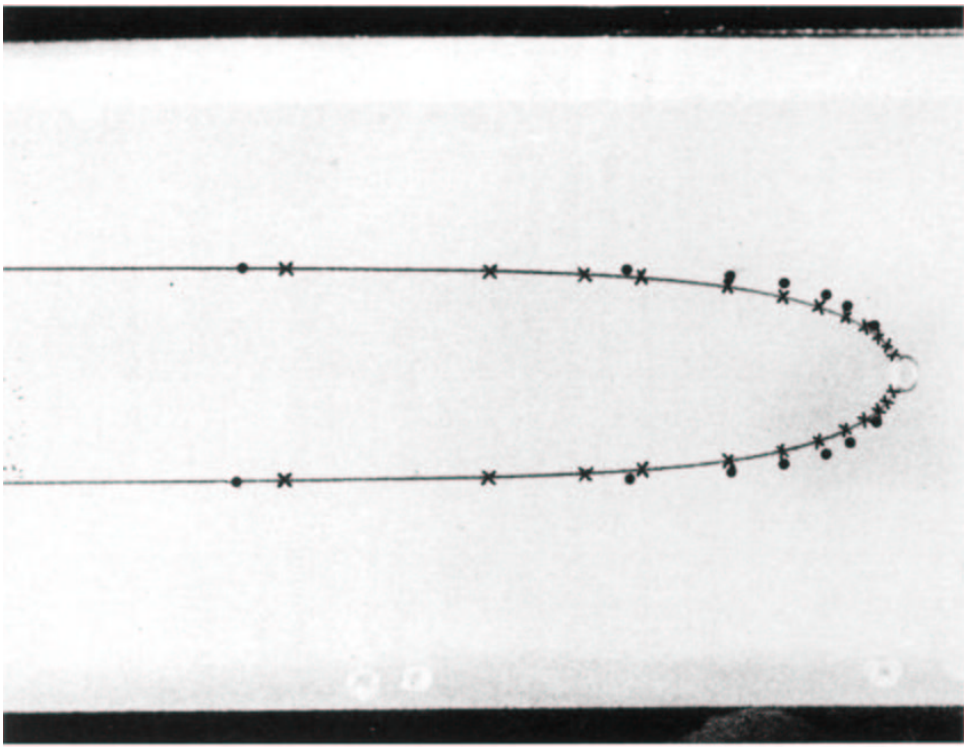

Figure 2.20: An anomalous finger with a bubble at the tip, moving at $V = 5.3$ cm/s in a cell of width $w = 6$ cm and gap $b = 0.1$ cm. The crosses are points on the theoretical profile of Saffman and Taylor (eqn. 2.28) for $\lambda = 0.32$; the dots are points from Pitts self-similar profile (eqn. 2.30) for the same λ. From Couder, Gerard, and Rabaud [35].

2.6 Alternate Geometries

2.6.1 Sector

If you take the walls of the channel geometry and angle them, you create the sector geometry (fig. 2.22), also referred to as the wedge geometry. The sector can be diverging, where the channel width increases in the direction of finger propagation, or converging, where the channel width decreases in that direction. Examples of viscous fingering in diverging sectors can be seen for a

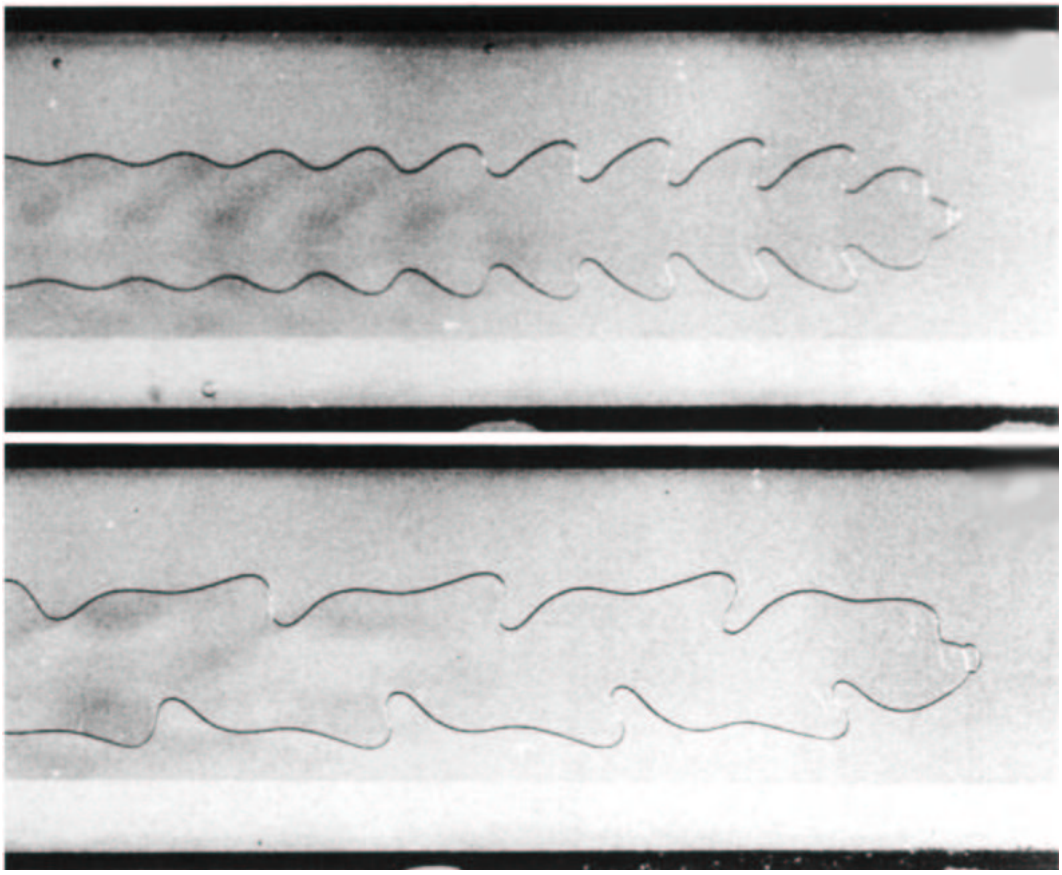

Figure 2.21: Behaviors observed for fingers with a bubble at the tip in a cell of width $w = 6$ cm and gap $b = 0.1$ cm. Top: The pulsating tip regime of a finger with a small tip bubble, $V = 10$ cm/s. Bottom: The oscillating tip regime of a finger with a larger tip bubble, $V = 7$ cm/s. From Couder, Gerard, and Rabaud [35].

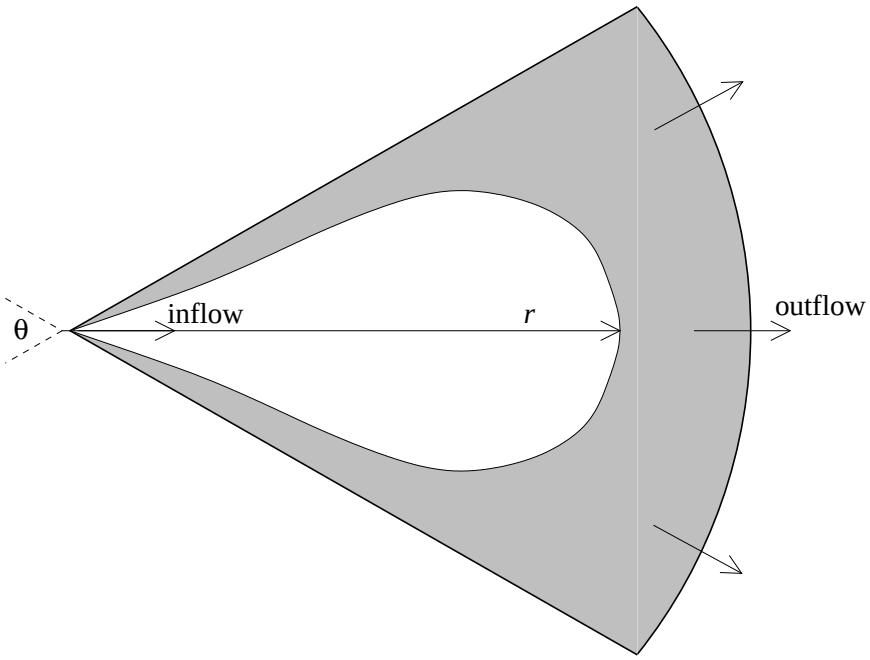

Figure 2.22: A schematic of the sector geometry, in this case, a diverging sector. The fluid flows in a wedge of angle θ; air flows in at a point (or short edge) while oil is extracted uniformly along the opposite arc.

narrow sector in fig. 2.23 and a wide sector in fig. 2.24.

Thomé *et al.* [141] were the first to work on the sector geometry. They observed experimentally that stable fingers growing in a wedge are self similar. Analytically, such fingers arise from a selection process similar to that observed in the linear geometry [9, 26, 10].

Much of the behavior of sector fingers can be understood by examining the channel parameter $1/B = 12\,\frac{\mu V}{\sigma}\left(\frac{w}{b}\right)^2$ and replacing the constant width w by $r\theta$, where r is the distance of the tip from the sector's convergence point (see fig. 2.22) and θ is the angle (in radians) of the sector. Thus, for a constant

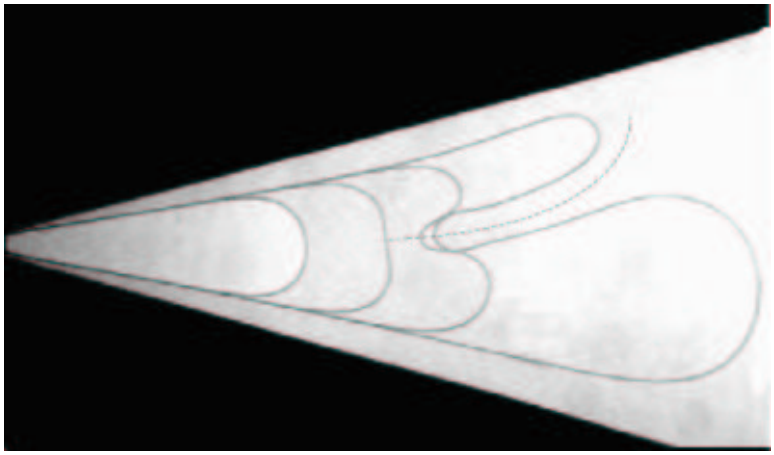

Figure 2.23: Four successive profiles from a Saffman-Taylor finger in a wedge of angle $\theta = 30°$, showing the dynamics of an imperfect tip splitting. The initial destabilization can be seen on the second profile; by the fourth profile the resulting secondary finger has stopped growing. The dotted line shows the shape of the fjord; the fingers act as though they were evolving in a cell shaped by the exterior wall and that fjord. From Lajeunesse and Couder [67].

velocity finger, the modified capillary number is $1/B = 12\,\frac{\mu V}{\sigma}\left(\frac{r\theta}{b}\right)^2$, which increases rapidly as the finger advances (r increases). The finger thus reaches the tip-splitting regime rapidly.

However, imposing a constant finger velocity requires imposing a constant pressure gradient, which is experimentally difficult. Usually, one imposes either a constant flow rate or a constant pressure difference.

In the channel, imposing a constant flow rate creates a finger with an approximately constant velocity. But in a sector, conservation of fluid implies the flow rate q is given by $q = r\theta bV$, thus $V = q/(r\theta b)$; the finger slows down as it advances. Overall, we have $1/B = 12\,\frac{\mu q}{r\theta b\sigma}\left(\frac{r\theta}{b}\right)^2 = 12\,\frac{\mu q}{\sigma}\left(\frac{r\theta}{b^3}\right)$, so the

Figure 2.24: A developed Saffman-Taylor fingering pattern in a sector-shaped cell of angle $\theta = 100°$. The tip-splitting instability is "perfect", the term introduced by Lajeunesse and Couder when the two branches generated by the first splitting keep growing to form two independent large-scale structures. From Lajeunesse and Couder [67].

modified capillary number still increases as the finger propagates, but not as quickly as in the constant velocity case.

Imposing a constant pressure difference (for example, by using a column of fluid of a given height to drive the flow), however, results in a finger that accelerates as it propagates. (This is true in the channel as well.) Here, for a pressure difference ΔP, $V \sim \Delta P / (r \ln(R/r))$, where R is the total length of the sector [141]. So in this case, the capillary number increases even faster than in the constant velocity case and the tip-splitting behavior is reached even more quickly. (See [141] for further insight.)

In the channel geometry, one of the fingers caused by a tip split always

stops growing and is suppressed. Lajeunesse and Couder [67] found that this remained true for sectors with $\theta < 70°$. They refer to this as "imperfect tip-splitting" (sometimes inaccurately referred to as side-branching). However for sectors with $\theta > 90°$, the first tip splitting resulted in two independent fingers which both continued to grow. They call this "perfect tip-splitting". For $70° < \theta < 90°$, both perfect and imperfect tip-splitting was seen.

This raises the question of whether there is a critical angle between perfect and imperfect tip-splitting. Analytic work by Arneodo *et al.* on DLA (sec. 3.1) and radial patterns suggests that these possess a 5-fold symmetry, which would imply that two independent fingers could only exist for sectors with $\theta \geq \theta_c = 144°$ [3]. Analytic work by Kessler *et al.*found $120 < \theta_c < 140$ [58]. The work of Lajeunesse and Couder [67] and Thomé *et al.* [141] suggests the critical angle is lower, though Lajeunesse and Couder point out that their evolution time may not have been long enough to determine if a particular finger was eventually going to be suppressed or not, thus lowering the apparent critical angle.

After a tip-splitting event (perfect or imperfect), each finger acts like it is growing in a wedge whose wall is defined by the fjord between them [67]; these are referred to as "virtual cells".

The converging sector geometry has also been studied [141, 9, 26, 10], though not as extensively. The fingers here are also self-similar, but the behavior is otherwise not very interesting, as the decreasing width leads to the suppression of tip splitting.

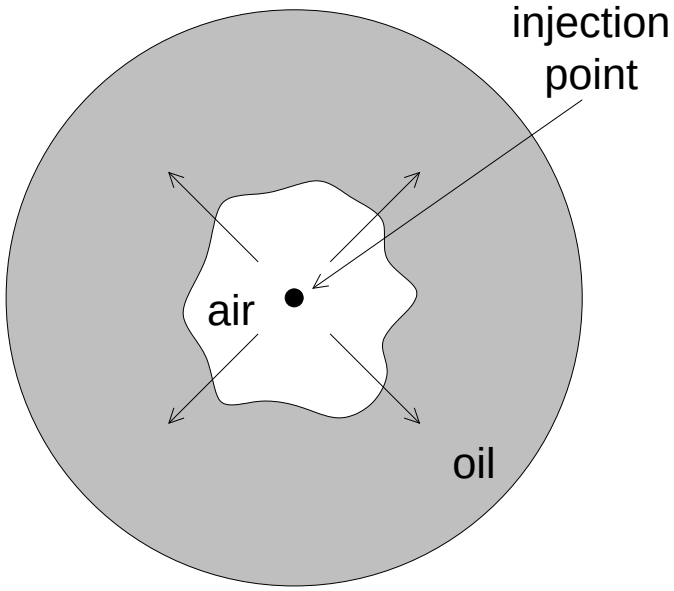

Figure 2.25: A schematic of the radial geometry. Fluid is injected (withdrawn) at the center and withdrawn (injected) uniformly around the sides.

2.6.2 Radial

The radial geometry can be in many ways be regarded as a sector with $\theta = 2\pi$ (and periodic boundary conditions). A schematic of a radial Hele-Shaw cell can be seen in fig. 2.25. Fluid is injected in the center and extracted uniformly in all directions. An example of viscous fingering in the radial geometry can be seen in fig. 2.26. Most of the concepts from the sector geometry carry over to the radial geometry, including the differences between constant flow rate and constant pressure difference forcing. The radial geometry was first studied by Bataille [8] and later by Patterson [107]; a great deal of later work exists, particularly work by Chen [24], Rauseo *et al.* [119] and Couder [67].

The concept of virtual cells also still applies; Thomé *et al.* [141] demon-

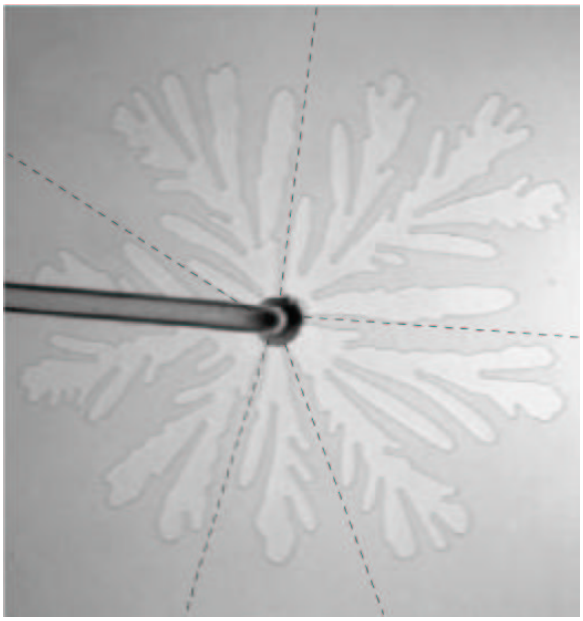

Figure 2.26: A highly branched pattern obtained in the radial geometry. The dotted lines show the primary fjords which form the virtual cells in which the fingers evolve. (The tube seen in this image is ubiquitous in radial experimental images, though it is not hard to redesign the experiment to remove it.) From Lajeunesse and Couder [67].

strated that radial fingers grow as if enclosed between virtual walls in a sector cell defined by the neighboring fjords. An example of this idea can be seen in the dotted lines on fig. 2.26.

The patterns in radial cells (and wide sectors) can become highly ramified at high forcing rates. The structures definitely seem similar to fractals, albeit with only a few generations of splitting. May and Maher [81] reported a fractal dimension of 1.71 for low flow rates with an abrupt transition at approximately Ca = 40 to 1.79 for higher flow rates. However, their work has a number of limitations. The biggest is that their patterns were not very

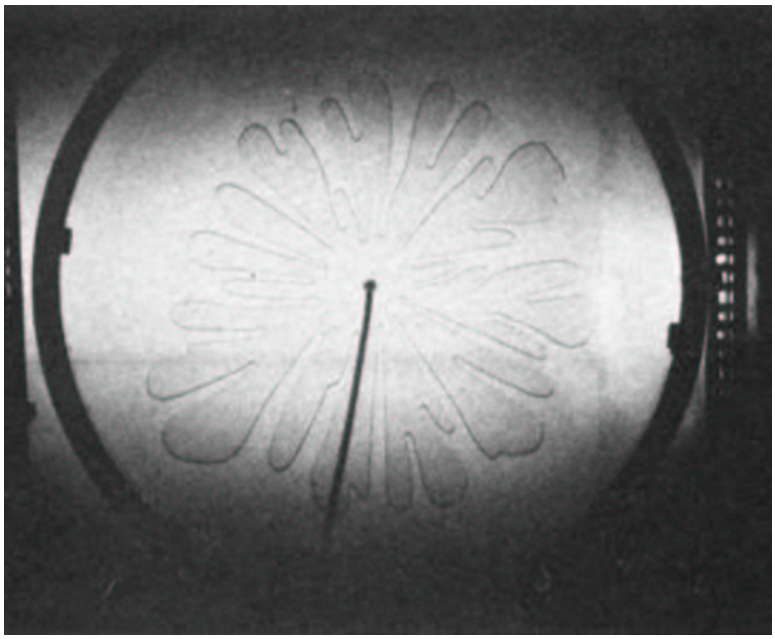

Figure 2.27: An image from May and Maher's [81] work on the fractal dimension of radial patterns. This pattern was produced at one of their higher flow rates ($\approx$ 78% of their maximum rate), yet is clearly undeserving of the term fractal, possessing at most two generations of splitting; our experiment can exhibit up to three more generations.

complex, possessing only two generations of tip splitting, as seen in fig. 2.27. (Compare that with our pattern, fig. 4.16.) Also, they obtained their fractal dimension D by measuring the radius of gyration of the pattern R_g and the area of the pattern A and fitting this to the relation $R_g \sim A^{1/D}$. This is similar to the cluster mass method of finding the fractal dimension, but applied *at only one point*, the origin. The method is not reliable unless averaged over many points [48].

Couder is really the only experimentalist (before us) to have generated

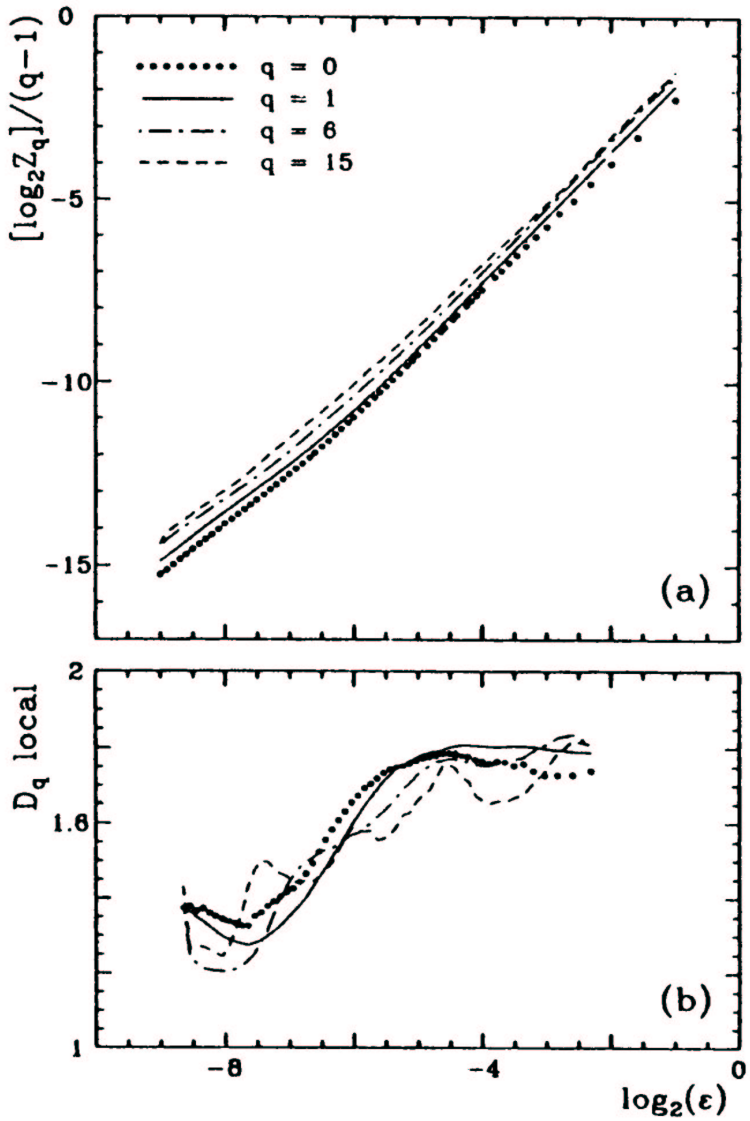

Figure 2.28: Multifractal spectrum for radial fingering pattern: (a) $\ln[Z_q/(q-1)]$ *vs.* $\log_2(\epsilon)$, where Z_q is a partition function and ϵ is the box size used in the partition. The slope of these lines gives the multifractal dimensions D_q. (b) The local value of D_q (i.e., the local slopes of the lines in (a)) *vs.* $\log_2(\epsilon)$. There is a small roughly flat range from $-5.5 < \log_2(\epsilon) < 2$, from which Couder [34] extracts his values of D_q.

radial patterns (with immiscible Newtonian fluids) that are ramified enough to deserve to be called fractal. He examined the multifractal spectrum [47] D_q for $0 \leq q \leq 15$ (fig. 2.28) and found values between 1.77 and 1.69, though his scatter was sufficiently large to consider these values roughly equal [34]. In particular, he found the capacity dimension $D_0 = 1.76$. (This is the dimension measured by box counting and cluster mass methods [48].)

People have also studied inflowing radial patterns [141], as shown in fig. 2.29. In many ways, this is the system most relevant to oil extraction; the more viscous fluid is withdrawn through a point and the less viscous fluid invades from the outside. In this case, the fingers screen each other as they converge until one finger reaches the center. All inflow of the viscous fluid then stops; only the less viscous fluid is now extracted.

2.6.3 Five Spot

The "5 spot" geometry is similar to the radial geometry except that the extraction of the outer fluid occurs only at four points surrounding the center instead of uniformly around the center [128, 22, 23, 102], as show in fig. 2.30. The initial patterns formed resemble radial patterns but change as the influence of the individual sinks is felt. This pattern has been studied because it more closely models the situation found in oil extraction, where all inputs and outputs are done through wells at specific points.

One potential source of confusion regarding the name of this geometry is that for analytic and computational work, only one quadrant of the system

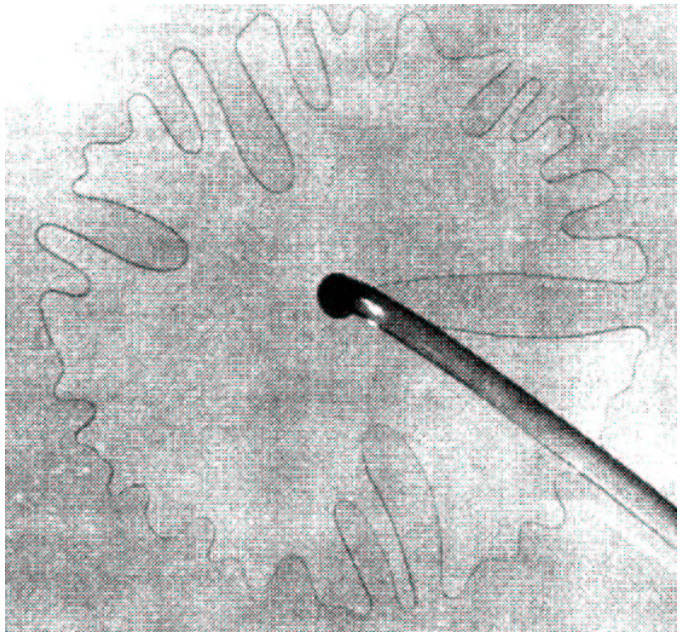

Figure 2.29: A pattern formed when the more viscous fluid is extracted from the center and the less viscous fluid invades from the edges. The converging fingers screen each other off; eventually one finger reaches the center and all other fingers stop. From Thomé, Rabaud, Hakim, and Couder [141].

is usually studied, with fourfold symmetry assumed [128]. That system has a source at one corner and a sink at the opposite corner of a square, and it might not appear immediately obvious why it's labelled "5 spot".

The only experimental realizations of the five-spot pattern appear to have been done with miscible fluids [70, 113]; I am not aware of any experimental work on the five-spot pattern with immiscible fluids.

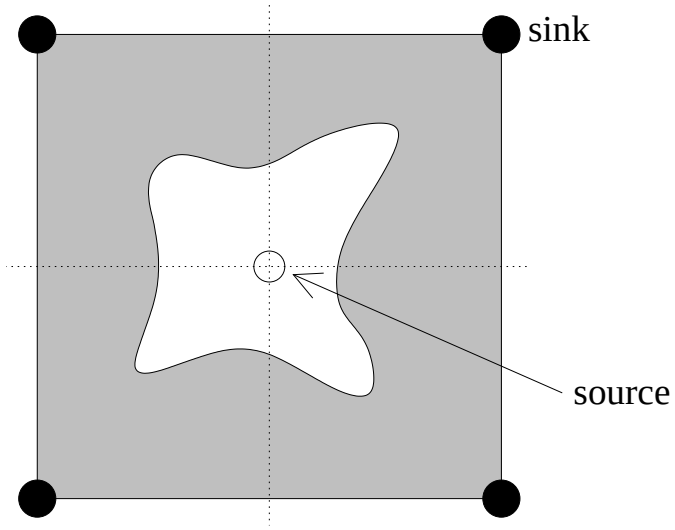

Figure 2.30: A schematic of the five spot geometry, where air is injected at the center and oil is extracted at four symmetrically placed points. The resulting flow is similar to the radial cell at first, then the fingers begin to feel the effects of individual sinks and head directly towards them. The dotted lines show axes of symmetry; frequently simulations are done for only one quadrant, with symmetric boundary conditions.

2.6.4 Other

Some more extreme geometric variations on Hele-Shaw cells have been considered, where the gap is a spherical shell [96, 103], a conical shell [95], or a cylindrical shell [94]. Additional approximations are required to derive Darcy's Law in these systems, generally that the radius of the system is large compared with the gap thickness. The only related experimental work was done in a cylindrical cell using a critical binary fluid mixture at a very low viscosity contrast [146]. It's not clear that those results would apply to more general circumstances.

2.7 Variations on Simple Saffman-Taylor Fingering

A large number of variations on the theme of simple Saffman-Taylor fingering have been studied, either as natural extensions or to connect with the related moving interface problems. A good overview is a review by McCloud and Maher, "Experimental perturbations to Saffman-Taylor flow" [82].

2.7.1 Anisotropic Cells

The similarities and differences between viscous fingering and crystal growth (and directional solidification) were discussed previously (chapter 1). One of the key differences is that for crystal growth, the surface tension is anisotropic because of the underlying crystal structure. So to remove this difference, a number of investigators have studied viscous fingers with an imposed anisotropy [11, 83, 115]. With this anisotropy, viscous fingers can exhibit patterns seen during crystal growth, such as needles (fig. 2.31(c)) and dendrites (fig. 2.31(d)). The latter also show true side branching (rather than imperfect tip splitting) like dendritic crystals.

2.7.2 Miscible and Non-Newtonian Fluids

Viscous fingering has also been performed with miscible fluids in the regime where the inter-diffusion of the fluids is slow compared to the finger growth time scale. Miscible viscous fingers are generally narrower and more fractal than immiscible viscous fingers [24].

A great deal of recent work has centered on viscous fingering in vis-

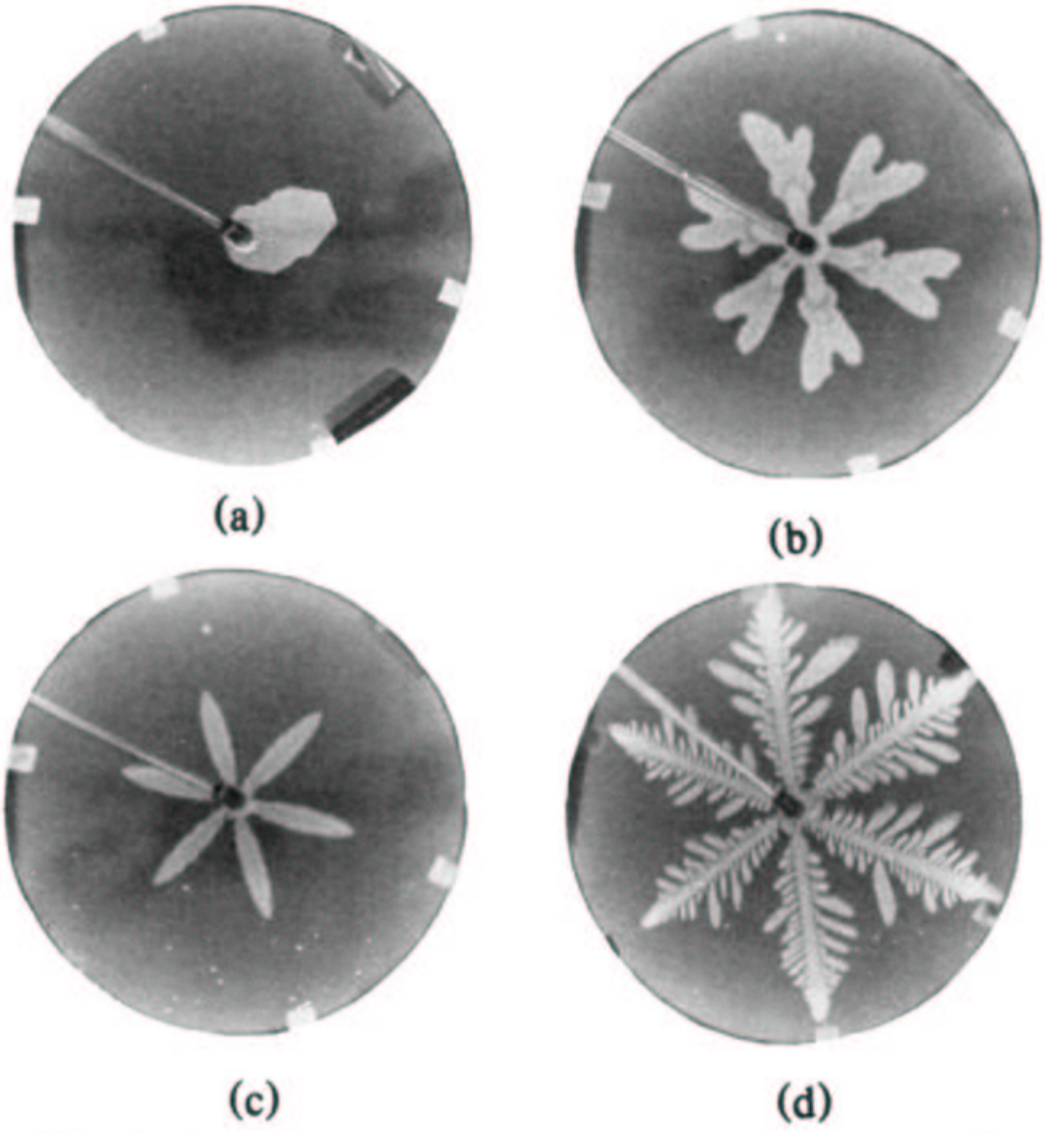

Figure 2.31: The various patterns observed in the Hele-Shaw experiments with anisotropy, in order of increasing applied pressure: a) faceted growth, b) tip splitting, c) needle crystals, d) dendrites. The plate is 25 cm across and is engraved with a regular sixfold lattice of grooves with a depth 0.3 times the gap depth (1.27 mm). From Ben-Jacob, Godbey, Goldenfeld, Koplik, Levine, Mueller, and Sander [11].

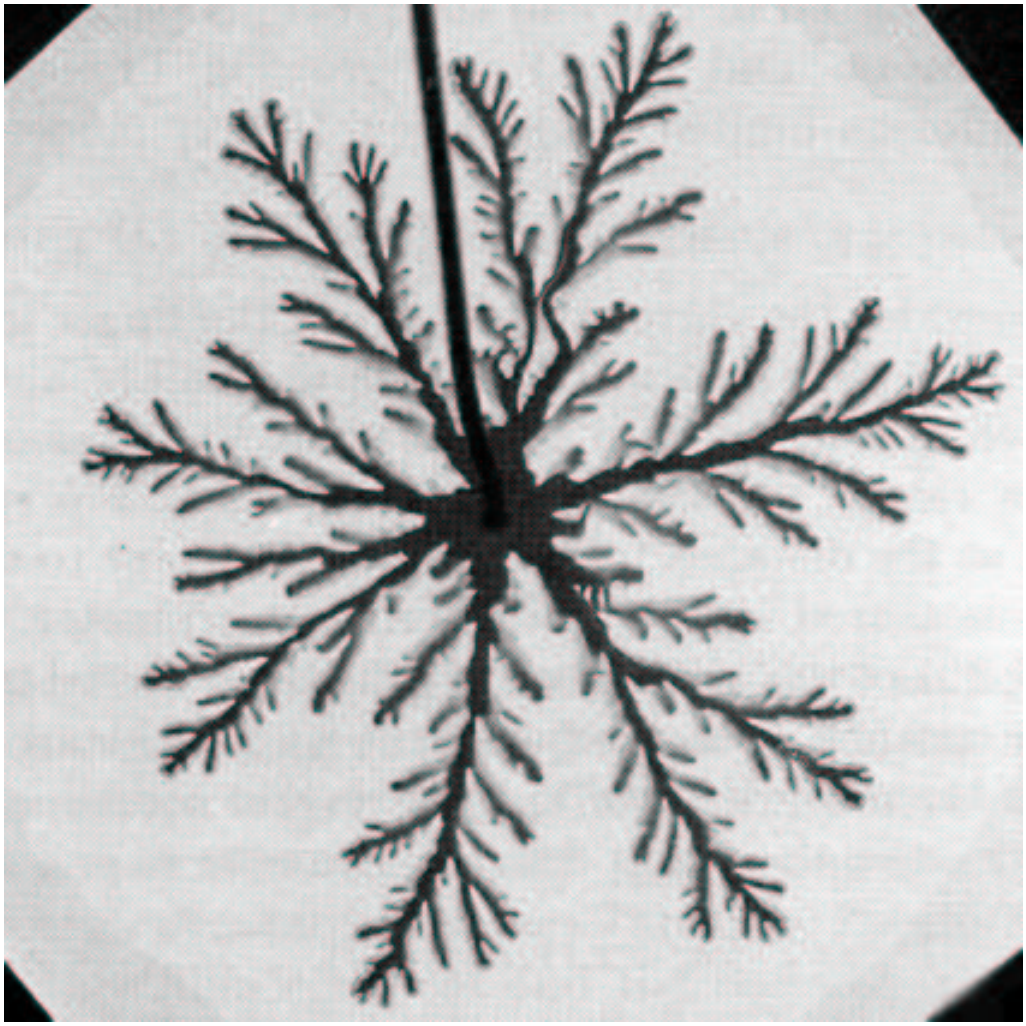

Figure 2.32: Dyed water displacing glycerol in a radial cell. This miscible pattern shows thinner water layers at the bases of side fingers and along the boundary of the pattern, widening of the branches, and interpenetration of the fingers. From Chen [24] (cropped).

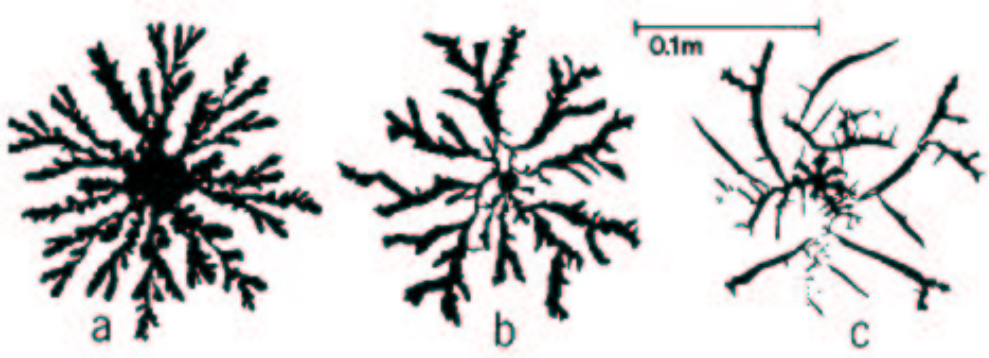

Figure 2.33: Patterns obtained by injecting water into water-based smectite muds or pastes. The clay/water ratios are a) 0.08, b) 0.10, and c) 0.20. a) A viscous fingering pattern, c) a viscoelastic fracturing pattern, b) a pattern in the crossover regime. The mass fractal dimensions of the pure patterns, derived by a box-counting method, are a) 1.65 and c) 1.43. From Lemaire, Levitz, Daccords, and Van Damme [71].

coelastic fluids [71, 143, 116, 63, 14, 62]. Depending on the particular fluids and forcing, all the previously mentioned patterns can be observed, plus new patterns such as viscoelastic fracturing (fig. 2.33(c)).

2.7.3 Other Variations

Viscous fingers have also been driven in alternate ways, such as time periodic forcing [118, 15], or by driving the fluids by separating the plates [66]. The former case can stabilize otherwise unstable growth or favor particular modes of growth; the latter case is of practical interest because it is related to fracture properties of metallic glasses. Plate separation patterns are also similar to inflowing radial patterns and can resemble river networks [121].

The plate separation experiment has also been done for an anisotropic

Figure 2.34: (color) A region from a time sequence of images from an experiment driven by separating the plates at one end (the bottom of image). The plates are approximately 9 cm square. The initial spacing between the plates is 0.05 mm, and the rate of separation at the lifted end is 0.025 cm/min. From La Roche, Fernández, Octavio, Loeser, and Lobb [66].

cell [11] and for shear thinning fluids [121]. In general, almost all of the variations discussed in this section have been combined (e.g., miscible viscoelastic fingering) by someone at some time. Space doesn't permit an exhaustive list of all these combinations, nor a list of many other variations on viscous fingering (such as, for example, chemical reactions at the moving fluid interface in Hele-Shaw cells — see [44] and references therein).

Chapter 3

Background: Diffusion Limited Aggregation and Coarsening

3.1 Diffusion Limited Aggregation

Diffusion limited aggregation (DLA) is a very simple model of crystal growth [145] that, despite its simplicity, has attracted an enormous amount of attention.

The simplest variation places a seed particle at the center of a rectangular grid, then places another particle on the grid a large distance away. This particle then executes a random walk on the grid until it comes in contact with the seed particle. It is then frozen in place. If the particle gets too far away from the cluster, it will be discarded and a new particle started. (Alternatively, the random walk is sometimes executed with periodic boundary conditions.) This process is repeated, one particle at a time: another particle is randomly placed on the grid a large distance from the cluster of previous particles and random walks until it comes in contact with the cluster, becoming part of it. This has been described as "growing a crystal one molecule at a time" [123].

An intricate, highly branched structure grows that displays fractal scaling with a fractal dimension $D = 1.713$ [39]. An example is shown in figure 3.1.

A number of other variations of this simulation exist. For large clusters, the anisotropy of the lattice begins to emerge in the growing pattern [56, 88, 87]. This led to the development of "off-lattice DLA", algorithms that don't constrain particles to a lattice and thus avoid the imposed anisotropy [124, 6]. Most current work uses off-lattice DLA; the qualitative appearance is the same as lattice DLA, but the quantitative results are slightly different [124, 87]. Other variations on DLA use different random walking algorithms [124], or attempt to reduce the shot noise inherent in the problem so as to reach an asymptotic state more quickly [6]. The overall qualitative properties are similar for all of these cases.

Despite the apparent differences between DLA and viscous fingering, there is an underlying mathematical correspondence between them. In the continuum limit of DLA, the probability u of finding a particle at a point obeys the diffusion equation [124, 13]. When a steady flux of walkers from source at infinity is imposed, this reduces to Laplace's equation [124, 13]. In addition, the velocity of the interface is proportional to the gradient of the probability density [124, 13].

The parallels are immediately obvious: for DLA, the probability density u obeys $\nabla^2 u = 0$, making the pattern grow with a local speed $\boldsymbol{v}_{\text{interface}} \propto \boldsymbol{\nabla} u$; for viscous fingering, the pressure field P obeys $\nabla^2 P = 0$, and the interface moves with velocity $\boldsymbol{v}_{\text{interface}} \propto \boldsymbol{\nabla} P$. These similarities are evident when examining the patterns formed in these systems; compare fig. 2.26 and fig. 3.1.

An example of this close connection between DLA and viscous fingering

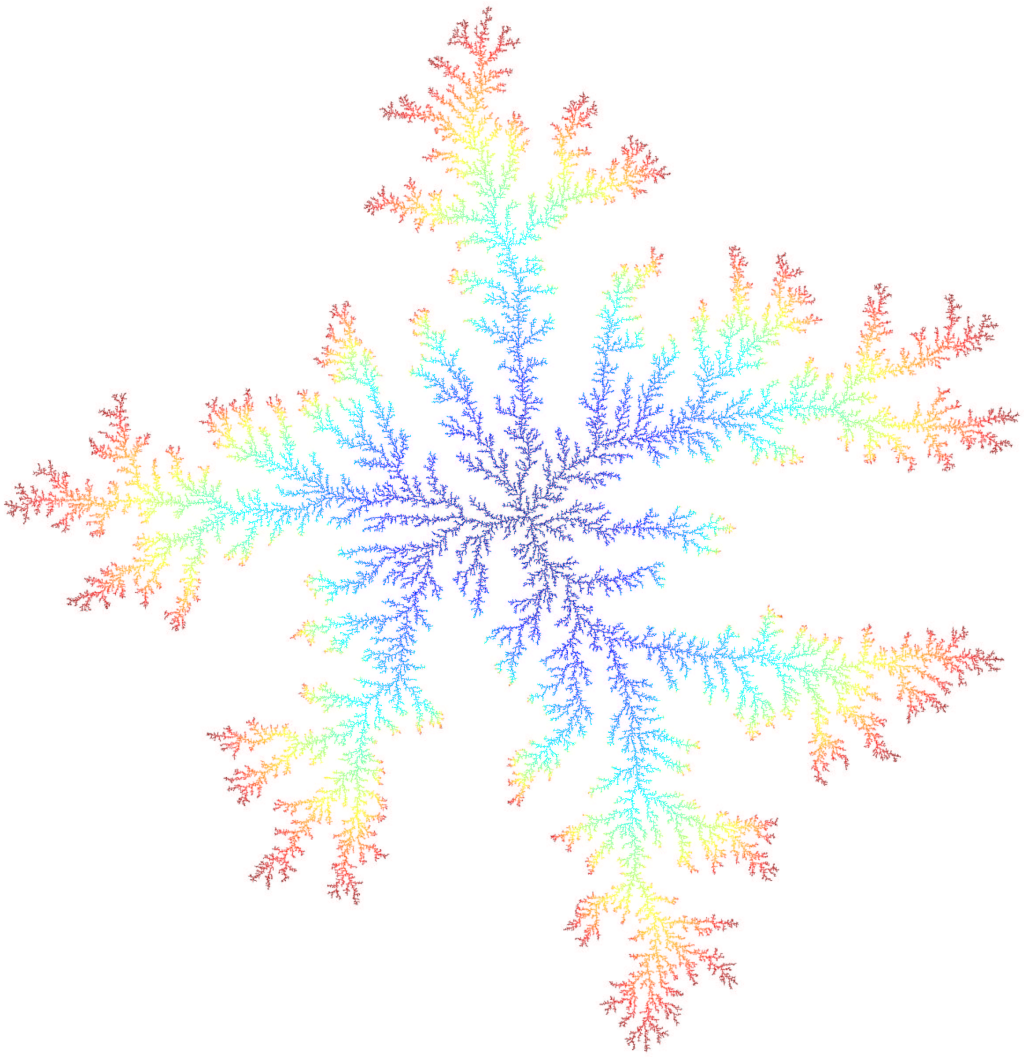

Figure 3.1: (color) A simple diffusion limited aggregate (DLA) grown by the author with 255,000 points on a 3000 × 3000 square lattice. The color (from blue to red) scales with the time of deposition.

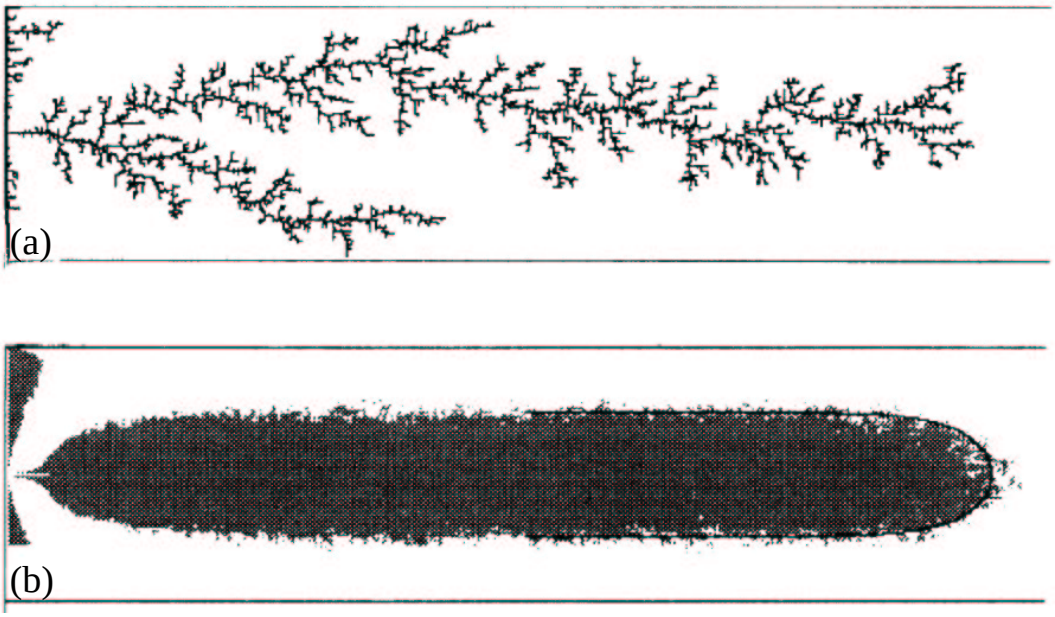

Figure 3.2: a) A DLA cluster of 6000 particles grown in a strip of width $w = 128$. b) A partition obtained from the analysis of 510 aggregates like that shown in (a) having the same number of particles (6000). The points of the cell where the occupation probability is larger than 1/2 are represented in grey. The continuous line is the shape of the Saffman-Taylor analytical solution (eqn. 2.28) of width $\lambda = 1/2$. From Arnéodo *et al.* [4].

is an intriguing discovery by Arnéodo *et al.* [4]. They grew 510 DLA clusters in a channel (an example is in fig. 3.2(a)), then averaged them to obtain the probability that a given cell was occupied in a particular cluster. When they then shaded in all cells where this probability was greater than 1/2 (fig. 3.2(b)), the resulting shape matched the profile of Saffman and Taylor's half width finger! This remarkable result continues to hold for DLA clusters grown in sectors; partitioning them on the probability 1/2 gives the analytic shape of the single finger solution for that sector.

The primary difference between the two systems is the origin of the cut-off at small length scales. For DLA, this cut-off is provided by the finite size of the particles. For viscous fingering, the cut-off is imposed by surface tension. This difference might seem minor and unlikely to affect the dynamics at large scales. However, because surface tension enters the viscous fingering problem as a singular perturbation, the form of the cut-off could in fact be crucial to the overall dynamics. A great deal of current debate exists on whether DLA and Laplacian growth are truly in the same "universality class" [39, 7, 5], though some of the proponents of them being distinct have recently withdrawn their claims [72].

Our radial system may be ideal for resolving this conflict experimentally because it can grow viscous fingers with fractal scaling over a greater range of length scales than any previous system.

3.2 Coarsening Systems

3.2.1 Introduction

A system which is driven far from equilibrium will relax towards an equilibrium state (or towards a new non-equilibrium state if the driving is changed but not removed), but its behavior as it does so can be non-trivial. A system can be found far from equilibrium either by changing the temperature from a temperature where one behavior is stable to a temperature where a different behavior is preferred, or by being driven far from equilibrium. After the temperature quench or after the driving is removed, the system will begin

its relaxation. This dynamical evolution from the initial disordered state to the final equilibrium state, usually called "domain coarsening", is described by the theory of phase ordering kinetics [17].

The prototypical example of a coarsening system is the ferromagnetic Ising model (simulated using Monte Carlo dynamics), which consists of a lattice of points each containing either an up spin or a down spin. Parallel spins have lower energy than anti-parallel spins. The lowest energy configuration is either all up spins or all down spins. However, at finite temperature, some spins will flip; the spontaneous magnetization as a function of temperature will appear as in figure 3.3. If we quench the system from an initial temperature T_i above T_c to a temperature T_f below T_c, there are two equilibrium phases with magnetization $\pm M_0$. But the system is still in the disordered state corresponding to T_i; it will not order instantaneously. Instead, ordered regions of parallel spins will form in the system and grow in size over time as the two different equilibrium phases compete to select the final equilibrium state.

An example of such a process is shown in figure 3.4. One feature of this particular coarsening scenario is that, if one re-scales the domains at later sizes back to the sizes at earlier times, the system looks statistically similar [17]. This property of "scale invariance" is elaborated on below.

A similar phenomenon occurs in the phase separation of binary alloys [79, 57] and binary fluids [133]. At high temperatures, the two substances will mix uniformly; at low temperatures they will spontaneously separate into different domains. (This is known as spinodal decomposition in binary alloys

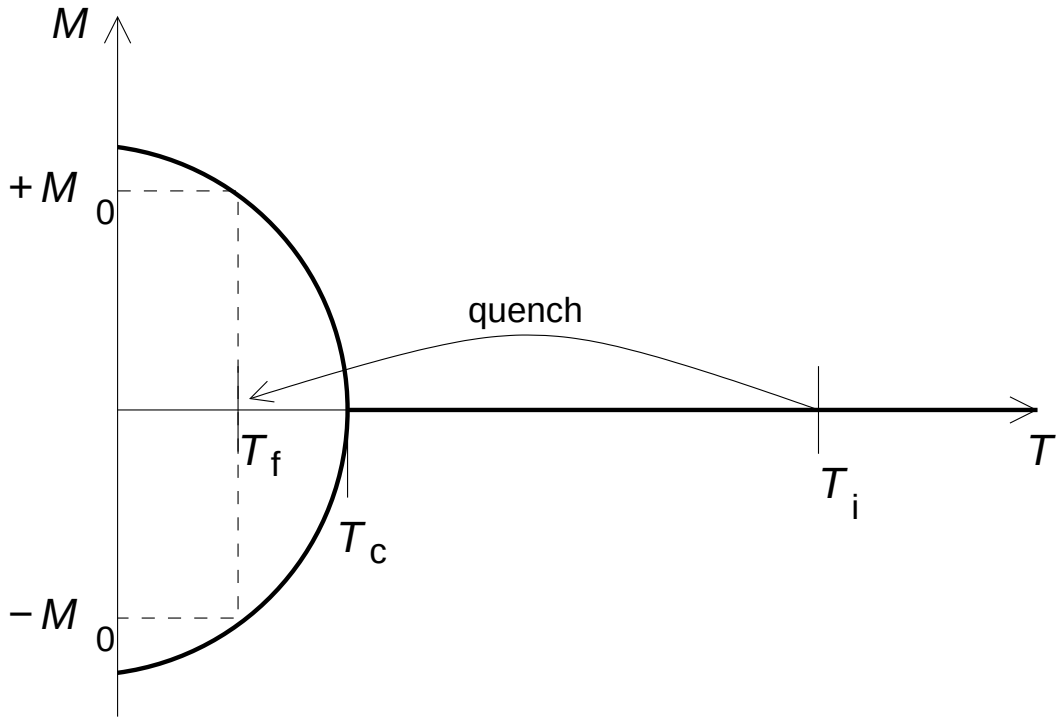

Figure 3.3: A schematic of the magnetization M of the Ising model as a function of temperature. Below the critical temperature T_c, two states are possible because of the spontaneous symmetry breaking. Immediately after a temperature quench from T_i to T_f, the system begins to form ordered domains of magnetization $\pm M_0$ which grow in competition with each other over time. (Figure modelled after fig. 1 in Bray [17].)

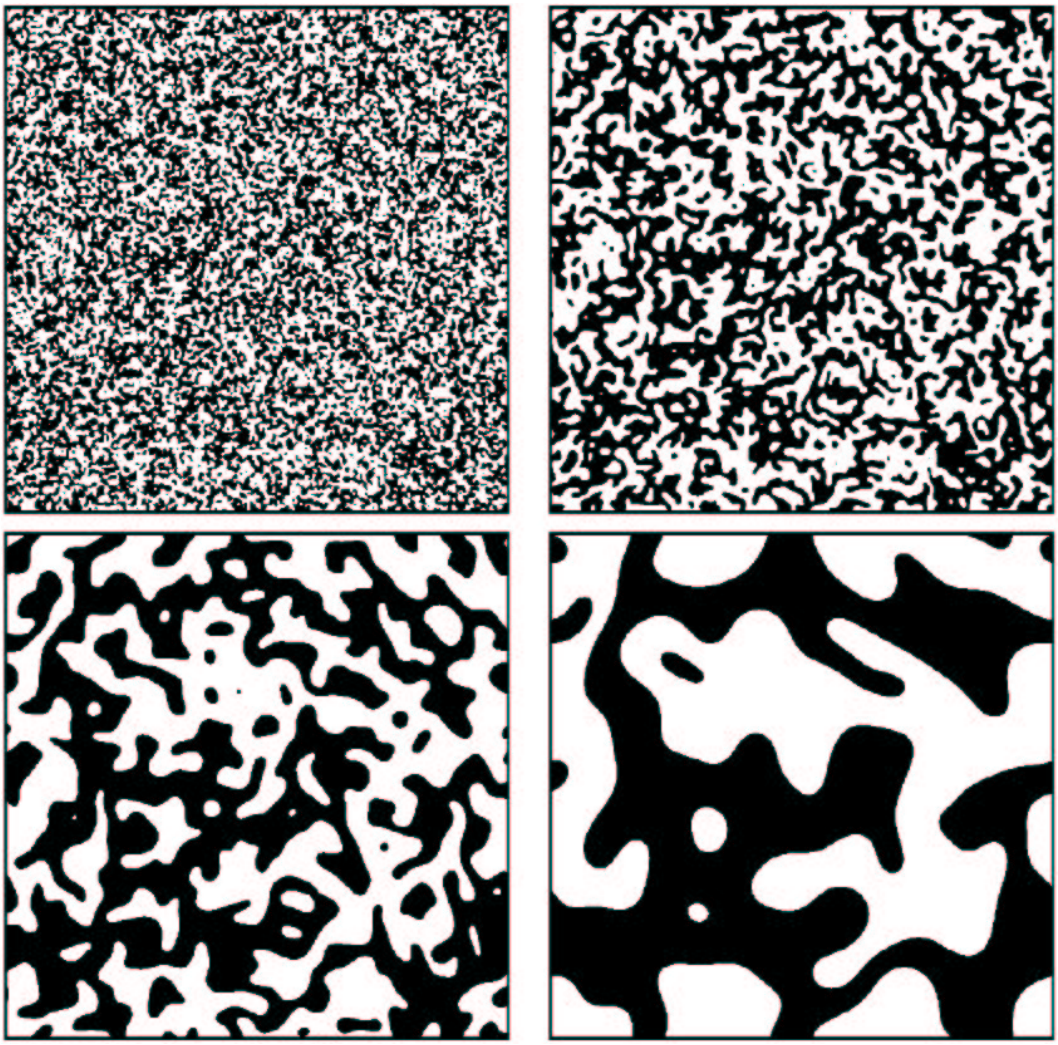

Figure 3.4: A sequence of snapshots of a globally conserved coarsening system from Conti, Meerson, Peleg, and Sasorov [30]. The initial conditions were "white noise" with equal areas of each phase. This is a simulation of a globally-constrained Ginzburg-Landau equation on a 1024×1024 domain with periodic boundary conditions. The times are $t = 5.2$ (upper-left), $t = 32.3$ (upper-right), $t = 204.8$ (lower-left), and $t = 1305.5$ (lower-right).

and mixtures; the late stage in both cases is referred to as Ostwald ripening.) These systems contain an additional element not present in the Ising models. In the standard Ising models, the total spin is not conserved. Any particular spin is free to flip by itself. However, atoms/molecules of one species in the binary substance cannot "flip" and become an atom of the other species. The relaxation process must proceed by having atoms of different species swap locations; the substances are locally conserved, and the underlying mechanism is diffusional. In the Ising model this would be equivalent to requiring that spin flips occur only in pairs between opposite spin neighbors. This has a significant effect on the phase ordering dynamics and will result in much slower coarsening than in the non-conserved case.

Another possibility is that a global conservation law could be imposed on the system, e.g. an Ising system where the total magnetization is conserved (by an external magnetic field), but sites do not have to be neighboring to exchange spins. While this does impose mild constraints on the system, they are not nearly as restrictive as the diffusion limited coarsening and behave similarly to non-conserved systems [30].

The study of domain coarsening has history of almost four decades, beginning with the work of Lifshitz [73], Lifshitz and Slyozov [74], and Wagner [144], and is described by the outstanding review of Bray [17]. Bray also explains that "Part of the fascination of the field, and the reason why it remains a challenge more than three decades after the first theoretical papers appeared, is that, in the thermodynamic limit, final equilibrium is never achieved! This

is because the longest relaxation time diverges with the system size in the ordered phase, reflecting the broken ergodicity. Instead, a network of domains of the equilibrium phases develops, and the typical length scale associated with these domains increases with time."

3.2.2 Scale Invariant Systems

These systems are usually analyzed quantitatively by examining the correlation function

$$C(\boldsymbol{r}, t) = \langle \phi(\boldsymbol{x} + \boldsymbol{r}, t)\phi(\boldsymbol{x}, t)\rangle_{\boldsymbol{x}}, \tag{3.1}$$

where ϕ is an order parameter describing the system. This is usually further averaged over all angles to produce a correlation function with two scalar quantities, $G(r, t)$.

The correlation function gives you the probability that if you go a distance r from a point inside (outside) the cluster, you will still be inside (outside) the cluster. The drop-off of the correlation function as r increases is initially linear (Porod law [17]) and provides one method for defining a length scale for the system. The correlation function for small r is fit to a line and the x-intercept is taken as that length scale.

For fractal systems, the correlation function, while still having an initial linear drop, does not immediately drop to zero. This reflects the long range correlations present in fractal systems. The correlation function will then exhibit a range of power law decay, and the magnitude of the exponent δ is

related to the fractal dimension $D_f = 2 - \delta$.

A scale invariant relaxation occurs when the system can be described statistically at all times by a single length scale, which itself changes in time as a power law, $L \sim t^{\alpha}$ in a simple manner. This means the correlation function $G(r,t)$ can be collapsed to a single function $f(r/t^{\alpha})$, as shown in fig. 3.5 for $\alpha = 1/2$. The non-conserved and globally conserved Ising models are scale invariant with dynamical exponent $\alpha = 1/2$. The locally conserved systems (e.g., binary substance separation) are scale invariant with $\alpha = 1/3$. One consequence of scale invariance is that all information about the initial structure is lost. A state with large domains of size ℓ that evolved over a short period from a relatively coarse initial condition cannot be distinguished from a state with domains of size ℓ that evolved over a long time from a very fine initial condition.

3.2.3 Fractal Coarsening

In the systems described so far, the initial conditions before they are quenched are usually set at thermal equilibrium at very high temperature. The initial state therefore possesses no long-range correlations. However, other systems that undergo relaxation begin with a state that is not in equilibrium at any temperature. Such systems are often the result of a non-equilibrium growth process and often generate fractal surfaces, as is the case in solidification from a super-saturated solution [69], growth of thin films during deposition [18], and the formation of a fracture surface in a brittle material [16] or

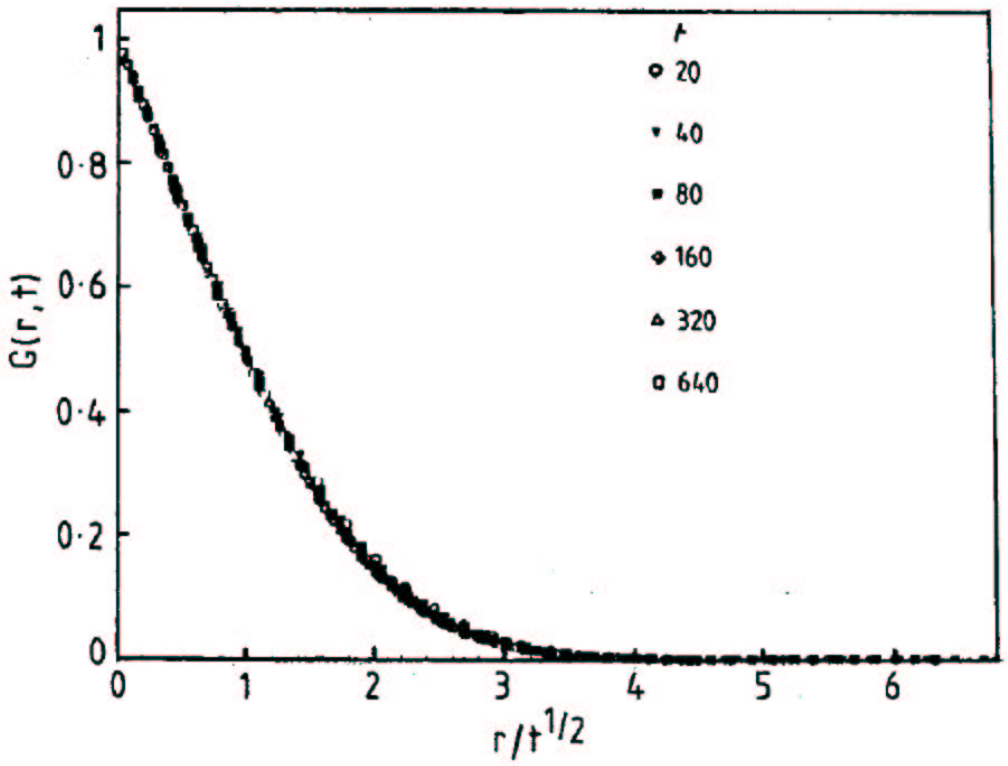

Figure 3.5: Scaling function $f(r/t^{1/2})$ for the correlation function of the 2-D non-conserved Ising model following a quench from $T = \infty$ to $T = 0$. The time t is the number of Monte Carlo steps per spin. From Humayun and Bray [54] (through Bray [17]).

geological landscape [112]. When the growth stops, these systems are also far from equilibrium and begin to relax.

When a fractal initial condition undergoes a coarsening process with a global conservation law, the resulting relaxation is still scale invariant [111], i.e., it is statistically self-similar at all times. However, when a fractal initial condition relaxes in accordance with a local conservation law, the scale invariance is broken. This means there exist multiple length scales that evolve in time independently of one another. Because of these multiple scales, systems that evolve over different lengths of time will appear different; in contrast to scale invariant systems, information about the initial configuration of the pattern is not lost. So far as we are aware, the locally conserved fractal coarsening scenarios described here are the only coarsening systems that are not scale invariant.

Conti, Meerson, and Sasorov [32] created a locally conserved fractal coarsening process by running a Cahn-Hilliard simulation on a DLA fractal. They created an initial DLA pattern with radius of order 250 using a standard random-walk algorithm on a 512×512 rectangular grid. They set $u = 1$ on occupied sites and $u = 0$ on empty sites, then numerically simulated a relaxation process using the (dimensionless) Cahn-Hilliard equation,

$$\frac{\partial u}{\partial t} = \frac{1}{2}\nabla^2\left(\nabla^2 u + u - u^3\right) = 0, \tag{3.2}$$

on the same domain. This is a diffusive relaxation process, which like surface tension is driven by the local curvature at the interface of the two phases. After

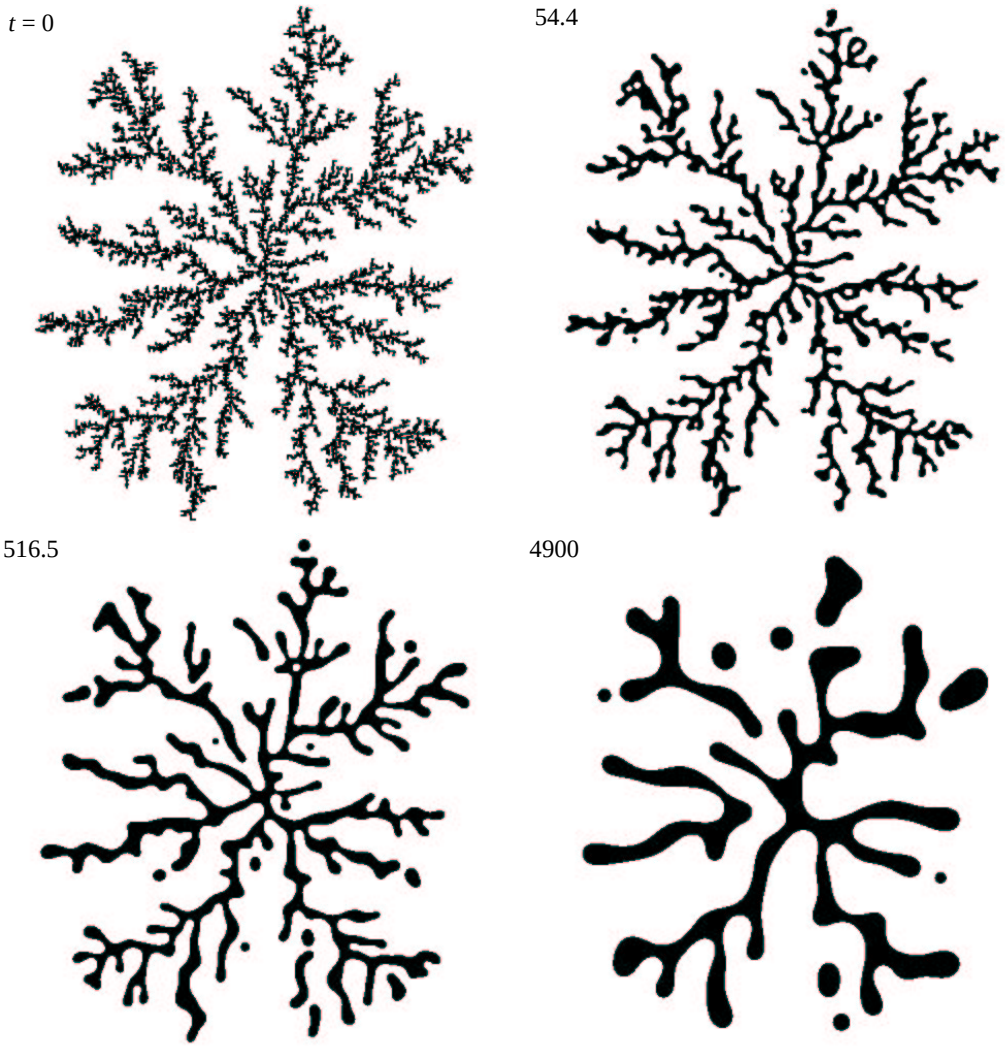

Figure 3.6: Coarsening of an initially fractal pattern according to a local conservation law. The size of the pattern does not shrink in time, as it would for a scale invariant system; instead the initially connected pattern breaks up. Provided by Conti, Meerson, and Sasorov [33].

evolution through 5000 time steps, u can range from -1 to +1. They then re-discretized the system to calculate the correlation functions by identifying the cluster as those points where $u(r,t) \geq 0$. They averaged these correlation functions over ten different initial DLA configurations.

Lipshtat, Meerson, and Sasorov [75] performed similar simulations with non-DLA fractals. They used a hierarchical algorithm to build random fractal clusters with tunable fractal dimension. They obtained qualitatively similar results; no clear dependence on the cluster's fractal dimension emerged.

There is one immediately obvious sign of the breakdown of scale invariance. In a scale invariant system with mass (area) conservation, the radius of gyration of the cluster L (upper cutoff of fractal scaling) must decrease in time. The argument (due to Conti, Meerson, and Sasorov [31]) is simple: the mass of the cluster M must scale as $M \sim \ell^d (L/\ell)^D$, where ℓ is lower fractal cut-off, D is the fractal dimension of the cluster, and d is the embedding Euclidean dimension. If $\ell \sim t^\alpha$, mass conservation immediately gives $L(t) \sim t^{(1-d/D)\alpha}$, a decreasing function of time. If the radius of gyration of cluster remains constant, then scale invariance has broken down, as Conti, Meerson, and Sasorov [32] observed; L changed less than 2% during the course of their simulations. This implies the emergence of multiple independent length scales as the system relaxes.

To further quantify the different behavior, they also examined the behavior of the correlation function. From the form of the correlation function at small scales (fig. 3.7), they obtained a length scale l_1 by fitting to a line and

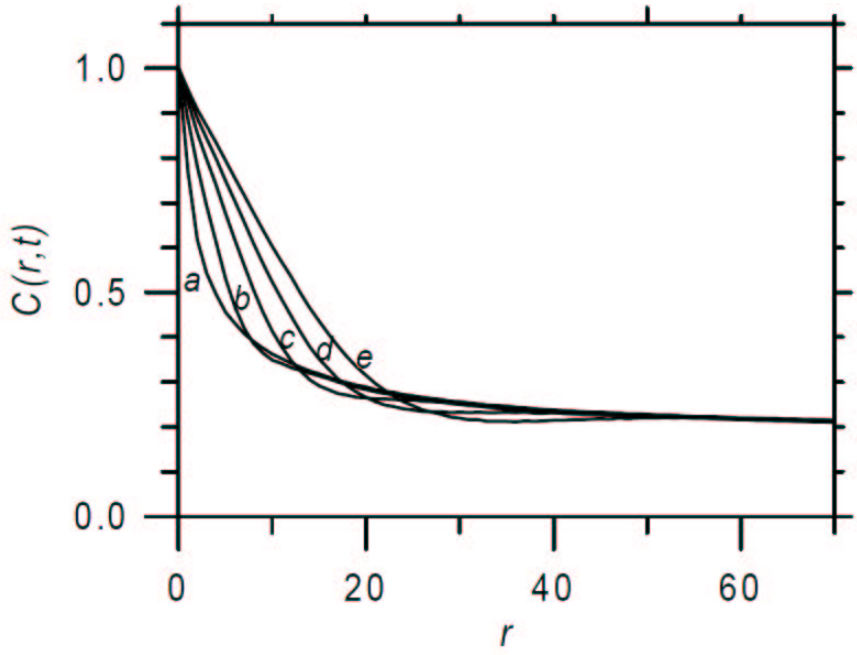

Figure 3.7: Dynamics of the correlation function $C(r,t)$ at small and intermediate distances during fractal coarsening for time moments t = 0 (a), 34.7 (b), 516.5 (c), 1992 (d) and 4900 (e). From Conti, Meerson, and Sasorov [32].

finding the intercept in the usual way. They found that this length evolved in time as $t^{0.20}$ at late times (fig. 3.8). This time exponent is significantly smaller than that for any of the scale invariant cases. (Lipshtat *et al.* [75] found an essentially identical time exponent, 0.21 ± 0.01.)

They then examined the behavior of the correlation function at large scales. As you can see in fig. 3.9, the correlation function develops a dip at large scales which clearly prevents the correlation functions at different times from collapsing to a single curve by a simple re-scaling. To determine a second length scale from this, they normalized the correlation functions

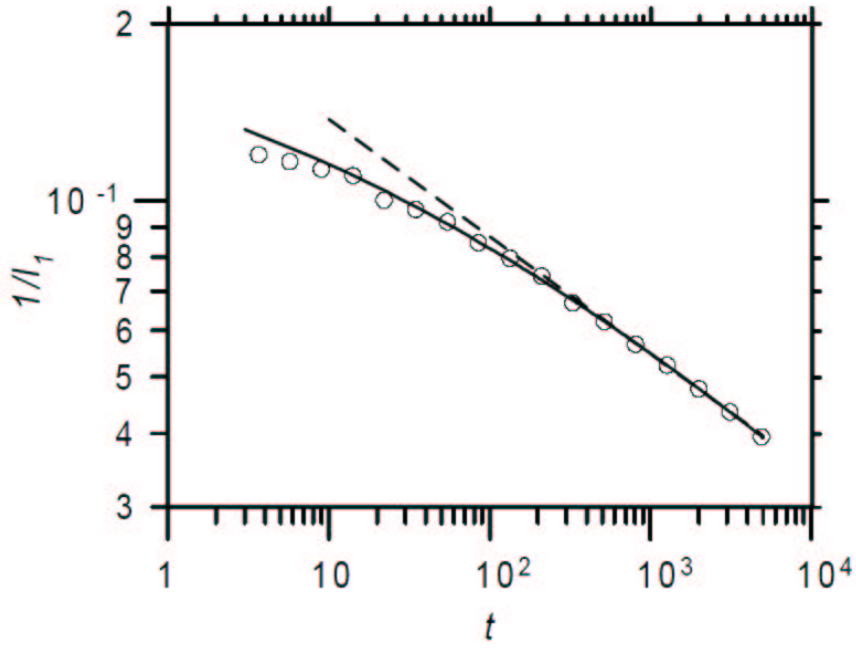

Figure 3.8: The inverse of the first correlation length $1/l_1(t)$ for a fractal coarsening system versus time (circles) and its fits versus a corrected power law of the form $1/l_1(t) = (0.44)/(2.0 + t^{0.26})$ (solid line) and versus a normal power law, $t^{0.20}$(dashed line). From Conti, Meerson, and Sasorov [32].

at different times to have the same value for $r = 300$. This collapsed the large r parts of the function together, defining what they called the "frozen tail". They then find the start of this tail by examining when the correlation function at late times differs from the correlation function at $t = 0$ by more than 3%. They take this as the second length scale l_2. (This definition has several deficiencies which I will discuss in describing our analysis of similar data from our experiment.) They found that this length evolved in time as $t^{0.39}$ at late times (fig. 3.10). This time exponent is significantly different from the exponent for l_1. Lipshtat *et al.* [75] found a time exponent of 0.32 ± 0.01,

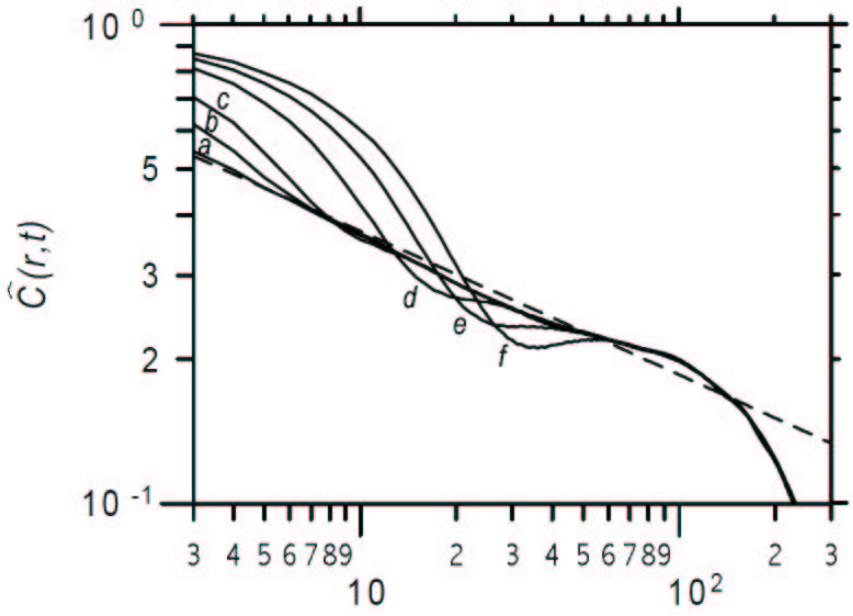

Figure 3.9: Dynamics of the correlation function $\hat{C}(r;t)$ during fractal coarsening at time moments t = 0 (a), 3.65 (b), 34.7 (c), 516.5 (d), 1992 (e) and 4900 (f). The dashed line shows the power-law fit $0.74r^{-0.30}$ on the interval $3 \leq r \leq 150$). From Conti, Meerson, and Sasorov [32].

which is similar to the exponent for the single length scale observed in locally conserving scale invariant coarsening systems.

The origin of this second length scale is the break-up of the cluster (which can be seen in fig. 3.6). Similar fragmentation has been seen numerically in the thermal relaxation of fractal clusters [101] and experimentally during the relaxation of thin metal films deposited on a substrate [18]. This break-up is an inevitable consequence of the combination of the increase of the small length scale and the constant size of the cluster. As we shall see (chapter 6), the second length scale corresponds to the average distance be-

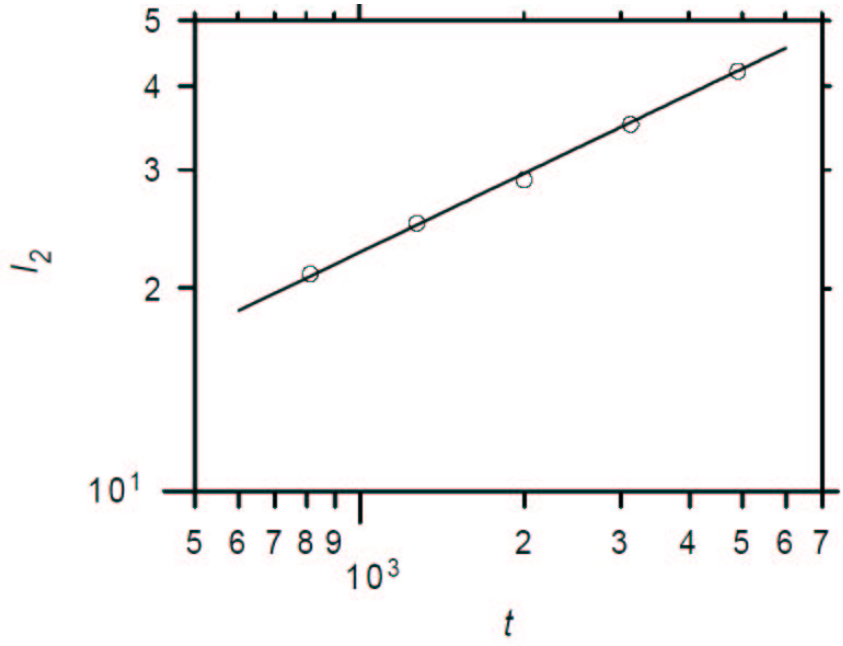

Figure 3.10: The second correlation length $l_2(t)$ for a fractal coarsening system versus time (circles), and its power law fit, $t^{0.39}$ (solid line). From Conti, Meerson, and Sasorov [32].

tween clusters as they break apart. It is the existence of this second length scale which clearly separates fractal coarsening from scale invariant coarsening processes.

Chapter 4

Experimental Setup

A simple Hele-Shaw cell is very easy to make — just slap some spacers between two pieces of glass or clear plastic and glue or clamp it all together. Most of the fingering phenomenon discussed in chapter 2 can be observed qualitatively in fairly crude, low aspect ratio ($w/b < 30$) cells. However, creating a Hele-Shaw cell for precision measurements at high aspect ratios requires attention to a large number of details and subtleties. In addition, the data acquisition and analysis can become quite complex. This chapter discusses the experimental design and data reduction for both of the cells we constructed, a linear cell and a radial cell.

4.1 Linear Cell

4.1.1 Linear Cell Design

The primary design goals for the linear cell were to have many initial fingers, to easily reach the tip splitting parameter regime, and to be able to follow the finger evolution for long times. The first two required a high aspect ratio, the last a long cell; together, this required an unusually large cell.

An overall schematic of the linear system is shown in fig. 4.1. The cell

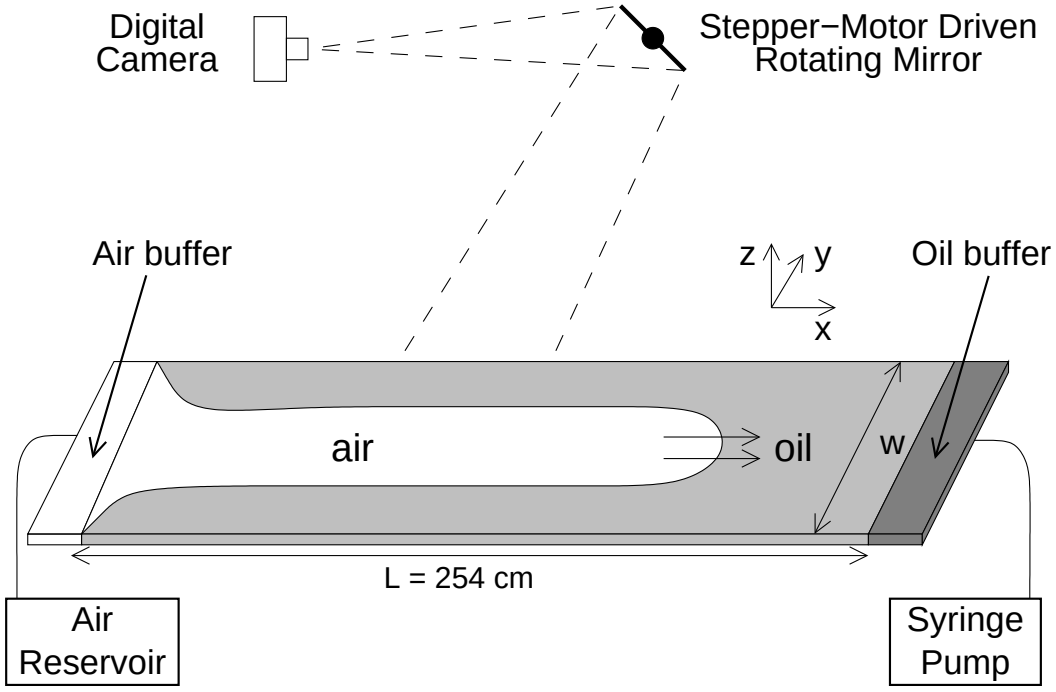

Figure 4.1: A simple schematic of the linear cell, showing the cell, the end buffers, the syringe pump and air reservoir, and the basic concept behind the optical system. The cell is lit from beneath. The entire system sits on an optical table.

is 2.54 m (100") long and can be configured in widths of 20.3 cm (8"), 22.9 cm (9"), and 25.4 cm (10").

The entire system is supported on an optical table. The optical table is floated using gas from an attached nitrogen bottle to isolate the system from floor vibrations. The pressure in the different table legs can be adjusted to tilt or level the table. A bubble level can be used to level the system approximately, but in the end, the cell itself formed a better bubble level. A large bubble can be left in the channel and the optical table adjusted until it

does not drift over time.

Also, for levelling of the cell around the long channel axis, a single steady finger can be drawn repeatedly and the table adjusted until the tip of the finger is exactly centered after propagating most of the length of the cell. For levelling this direction, this proved faster than watching the drift of a bubble. As discussed later, the levelling of the cell around its long axis can be crucial to observing some phenomena; levelling around the short axis is less important.

A schematic of the light and clamping system is shown in fig. 4.2. The cell itself is raised above the table so that it can be lit from below. (Early attempts to light the system from above generated images that were too difficult to analyze.) To do this, eight blocks of aluminum were machined to the same height within a tolerance of 0.001". (The design drawings for this are in appendix A, pg. 178.) These blocks are then bolted to the optical table. Additional blocks of the same height were machined (design in appendix A, pg. 179) to support the cell when it is configured for widths narrower than its full 25.4 cm (10") width.

Between the aluminum blocks are two 243.8 cm (96") long ultra-bright fluorescent light bulbs (Sylvania FS8D12/D41 75 W). Because the ends of the cell were farther from the camera, they were dimmer than the center, enough so that an additional 7 W incandescent bulb was placed under the channel at the air buffer end. (A bulb was not needed at the oil buffer end, because we do not let fingers reach the far end to avoid end effects and therefore don't

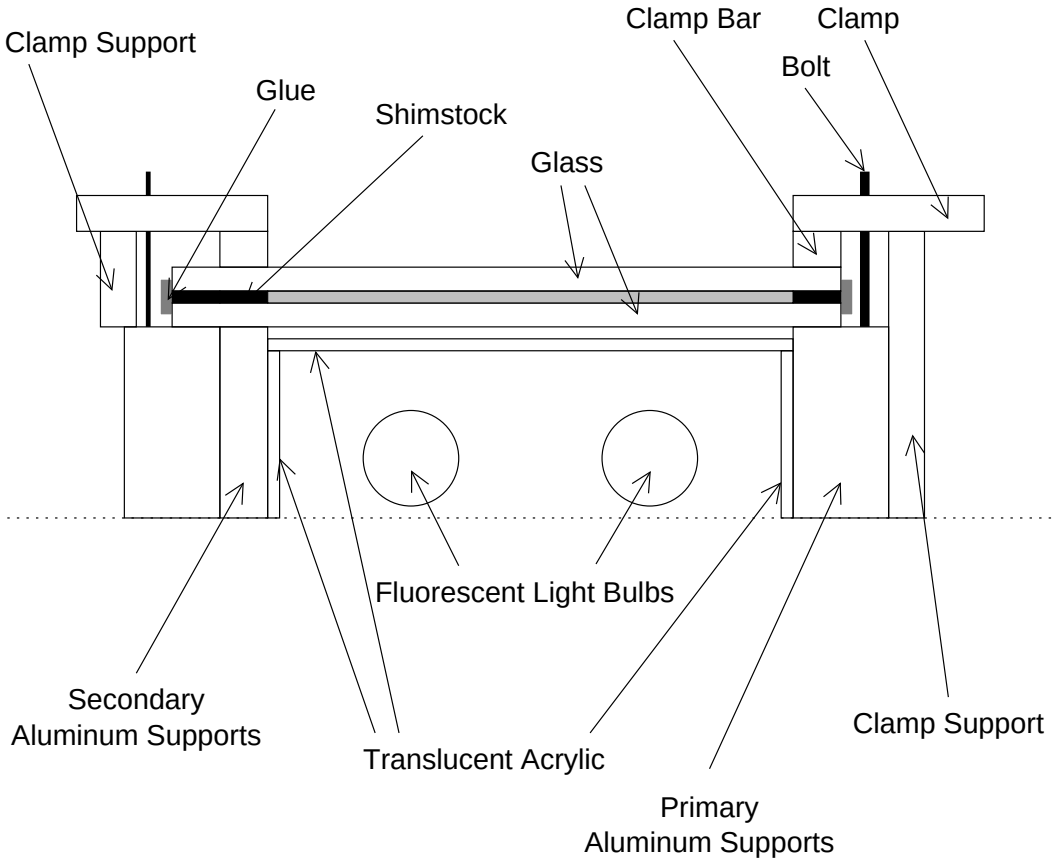

Figure 4.2: A schematic (not to scale) of the cell supports, lights, and clamping mechanism. The cell is shown in a 22.9 cm (9") wide configuration to show the use of the secondary supports (left side) for narrower cells. The clamps on the left side illustrate the original clamping design; those on the right illustrate the improved clamps developed later. The light diffuser (translucent acrylic) is placed just below the glass without touching it.

need to visualize all the way to that end of the cell.) To prevent the lights from heating the cell, two small fans were placed between the blocks at one end; the airflow kept the light area at the ambient temperature.

The light from these bulbs is diffused and spread evenly by a sheet of

0.32 cm (⅛") thick white translucent acrylic located just below the cell. The acrylic sheet is supported at the sides by additional pieces of acrylic, usually attached to the blocks via double-stick scotch tape. (Using the same acrylic to support the sheet was simply a matter of convenience; a better design would be to machine grooves in the blocks that the sheet could slide into.)

The cell itself is formed from two 1.91 cm (3/4") thick sheets of float glass (obtained from Binswanger Glass Company) 2.54 m (100") long and 30.5 cm (12") wide. The gap is created by strips of stainless steel shim-stock (obtained from Lyon Industries). The strips were cut 2.54 m (100") long and sanded at the ends in case the cutting process bent them there.

The width of the cell is controlled by the width of the plates and the width of the shim-stock spacers at the sides. The only way to assure the width is uniform down the channel during assembly is to leave the shim-stock sticking out of the sides at first, then use a long flat object to push them in flush with the glass. This produces minor variations in the width each time; the exact width must be measured after the assembly is completed. The most precise way to do this is through the optics and camera (described later). A list of the combinations of shim stock we used to reach various cell configurations is shown in table 4.1.

The glass plates would be expected to sag under their own weight, but calculations showed that the amount of sagging would be less than 0.2% of the smallest gap depth (see calculations in appendix B). In addition, by supporting both glass plates at the sides in the same way, any sagging of the

w/b	Shim Stock	Schematic
500[a]	2 1"×0.020" pieces	
400W[b]	2 1"×0.025" pieces	
400N[b]	2 2"×0.020" pieces	
320	4 1"×0.025" pieces	
250	4 1"×0.020" pieces	
225	2 1"×0.020" pieces, 2 2"×0.020" pieces	
160	8 1"×0.025" pieces	
60[c]	4 1"×0.025" pieces	

[a]This combination was used in the small alternate cell to reach $w/b = 150$.
[b]400W means "400 Wide", $w = 25.4$ cm; 400N means "400 Narrow", $w = 20.3$ cm.
[c]In the small alternate cell.

Table 4.1: The various cell configurations used for the linear cell, along with the shim stock combinations required to create them. The schematic shows the physical arrangement of the shim stock (and which type, using thin lines for 0.020" shim stock and thick lines for 0.025" shim stock), though the spaces between pieces are obviously just for clarity. (The aspect ratios listed are the nominal ones for 30.5 cm (12") wide glass; the measured aspect ratios were slightly less.)

plates would be identical, thus preserving the uniformity of the gap.

For many experiments, we attempted to change the wetting properties of the spacers by coating them with Scotchguard. This did not have a major effect on the finger dynamics but did change the way in which the interface pinned at the back corners of the channel. With the Scotchguard, the oil still wet the shim-stock, but the interface tended to leave the pinning point nearly parallel to the walls; without it the interface usually left perpendicular to the side walls. (These differences can be seen between fig. 5.3(b) and (c).)

The cell is held together by a series of clamps that attach to the supporting blocks. The force from the clamps is distributed evenly over the length

of the cell by 2.54 m (100") long, 2.54 cm (1") wide, 1.27 cm (0.5") thick aluminum bars. The glass is protected from the bar via a thin length of weather stripping. The clamps can be adjusted so that the bars exert their force over the inner-most strip of shim-stock, regardless of the cell width.

In the original design (left hand side of fig. 4.2), the clamps were counter-supported by aluminum pieces that rested on the support blocks. The clamps and bar were aluminum. The cell had 8 clamps on each side, in an alternating pattern. This design had a couple of small problems. The position of the counter-support pieces was physically awkward. The aluminum bar flexed slightly when clamped down and did not spread the force evenly along the cell. The number and arrangement of clamps also augmented this. Finally, the aluminum clamps and ¼–20 bolts that attached them to the blocks would bend when tightened as much as necessary to obtain a uniform gap inside the cell.

The clamping system was later improved by modifying the support blocks to allow twice as many clamps with ⅜–16 bolts, by using new clamps, bars, and counter-supports made from steel, and by extending the counter-support bars down to the table and bolting them to the sides of the support blocks. The new system did not actually improve the cell uniformity measurably, but it became much easier to obtain good cell uniformity. Most of the experiments described in chapter 5 were done with the original clamping arrangement. (Designs for the clamp and support modifications are in appendix A, pp. 180–181.)

After cell assembly, the uniformity of the cell was checked by examining the interference fringes created when a bright sodium lamp was shone on the cell. The cell uniformity could then be further tweaked by individually adjusting the clamping bolts. Even for the highest aspect ratio cells ($w/b \approx 500$, width 25.4 cm (10"), gap 0.508 mm (0.020")), the cell gap uniformity $\delta b/b$ could be made less than 1%; the root-mean-square variations in gap thickness were typically 0.6% or less.

The glass also bent under the imposed pressure gradient, further lowering the uniformity of the gap. The pump imposes a uniform flow rate which from Darcy's law implies a uniform pressure gradient along the channel. The air reservoir is at atmospheric pressure, so the maximum difference from atmospheric pressure and therefore the largest deflection would occur at the farthest point from the air.

The magnitude of the plate bending could be measured using a dial caliper which had marks down to 0.0001" (2.54 μm) (and estimable to about ¼ of that). The maximum deflections were observed where expected, in the center of the widest channel near the oil reservoir at the start of an experiment. As the interface advanced during an experiment, the bending relaxed. The bending was unmeasurably small at low flow rates; the maximum deflection observed in the single finger regime was 2.2%. (This was for a finger velocity of 0.268 cm/s in the $w/b = 494$ set-up, $1/B = 3630$.) The observed magnitude of the bending agreed roughly with calculated estimates (see calculations in appendix B).

The sides of the cell are sealed using a latex roof patch (StaKool Roofing Patch). This glue is easy to apply, seals well, and is easy to remove – most of it peals off and the remainder dissolves in acetone and methanol. (It does, however, ruin cotton shirts by adhering to them, as it was designed to adhere to a muslin mesh that would initially cover the hole in the roof to be patched.) This sealant seems to have gone out of production, but it appears that another roof patch (KoolSeal Patching Cement) is similar and performs acceptably.

This choice of sealant is unusual, but silicone caulking, the usual sealant for fluids experiments, cannot be used in our system because the silicone oils we use will soften and eventually dissolve it. We did try using a vacuum wax (Apiezon W40) to seal the sides of the cell. While it did seal without requiring time to dry, the "wax" was a tar-like substance that had to be heated to applied and wouldn't dissolve in common solvents. Using it was disastrous, resulting in burns, ruined clothing, and a long overwhelming clean-up job.

The roof patch isn't strong enough to seal the buffers to the ends of the cell; the only usable glue we found for this was a 5-minute epoxy gel (by Devcon). Unfortunately, the epoxy adheres to the glass too well, taking small chunks and slivers of the glass with it when the epoxy is removed during cell disassembly. This has not caused a serious problem yet, as we have taken great care to ensure that the edges where fluids flow in and out have remained pristine. The epoxy is also unforgiving of mistakes – the epoxy must seal the buffer when first pressed against the cell end. Otherwise it will be difficult to seal it completely without removing it.

Fluid (Nominal Viscosity)	Measured Viscosity	Measured Surface Tension
Lot AA076307 (10 cS)	9.56 mPa · s	19.51 mN/m
Lot 00002672 (10 cS)	9.21 mPa · s	19.57 mN/m
Lot AA036105 (50 cS)	50.78 mPa · s	20.63 mN/m
Lot LL014537 (350 cS)	345 mPa · s	20.98 mN/m

Table 4.2: Relevant properties (dynamic viscosity and surface tension) for all of the fluids used in the linear and radial cells. The variations with temperature of these quantities are about 0.09 mPa · s/K and 0.07 mN/m · K [42], less than 1% per degree in all cases.

The fluids used in the experiments were Dow Corning 200 Fluids, silicone oils available with a variety of viscosities. These oils wet glass completely. The viscosity of the oils was measured using a rotary viscometer (Cannon LV2000), using the low centipoise adapter for oils with $\mu \lesssim 50$ mPa · s. The viscometer was calibrated using either distilled water or a calibration fluid (Cannon Viscosity Standard RT50). To obtain accurate measurements of the surface tension, samples of the oils were sent to an outside lab. (In each case, the lab manager was Dr. Christopher Rulison, originally at ThetaDyne Corporation, then at Krüss USA, now at Augustine Scientific.) Oils from different lots with the same nominal viscosity had values of the viscosity and surface tension that differed by a few percent, so it was important not to mix them. Table 4.2 contains the data for all fluids used in both the linear and radial cells. The oils were always filtered to remove dust and other small contaminants before being used in the experiments.

To ensure uniform outflow of oil from the cell, a buffer of oil is glued

to the end of the cell. An air buffer is similarly attached to the other end of the cell. The buffers are designed so that the interior of the top side slopes up like a bowl to a threaded hole at the center. (See designs in appendix A, pp. 182–185.) In the oil buffer, this slope forces bubbles up to the center where they are easily forced out. The hole is closed with an 1/8-NPT plug. The air buffer is attached upside-down, so that the slope here allows excess oil that was pushed through the cell to drain away to a small reservoir.

The air buffer is connected via Tygon tubing to an air reservoir, which is a Mylar balloon partially filled with dry nitrogen. Because the Mylar balloon has no elasticity in such case, the air buffer will be at atmospheric pressure. However, the balloon will prevent dust and other contaminants from entering the system.

The oil buffer is connected to a series of 4 syringes (Hamilton Gastight 100 mL, model 86020) with 1/4" Tygon tubing through three sets of Y connections. The syringes have Luer-lock connections, but this size tube fits easily but snugly over the syringe tips, eliminating the need for a series of connectors there. The syringes are mounted on a syringe pump (kd Scientific Model 230, modified slightly to accommodate the large Hamilton syringes). The syringe pump can inject or withdraw a given amount of fluid at a very precise rate over a wide range of flow rates (1 μL/h to 100 mL/ min), and can be controlled manually or through an RS232 interface to a computer.

At the end of one run, we visually checked the uniformity of the flow across the width of the channel near the buffer using Kalliroscope PM-01

(titanium coated mica flakes), and though we didn't attempt to quantify it, the flow appeared quite uniform. Provided the buffer was large enough, we would expect this; analytically, Gondret *et al.* [46] found that the departure from uniform flow would be negligible more than one gap thickness from the wall for $w/b > 10$. (This may explain why previous experiments got away with using such low aspect ratios.)

One set of experiments was performed with pumping driven by gravity rather than the syringe pump. This was done simply by raising and lowering a pan of oil connected to the oil buffer through a tube. This created a pressure difference between the pan and the buffer that pumped oil at a rate proportional to the difference in height between the oil in the pan and the cell. The pan had a large area so that the change of the fluid height due to the oil flow would be negligible.

However, by imposing a pressure difference rather than a flow rate, the fluid velocity increased as the finger propagated down the channel: the same pressure difference was imposed over a smaller distance, creating a higher pressure gradient and thus a higher flow rate. For this experiment, the plot of finger tip position versus time was slightly but noticeably parabolic; the velocity at the end of the experiment was 27% higher than that at the beginning. This had no apparent effect on the finger width results. However, as discussed in sec. 2.6.2, the distinction between imposing a pressure difference, imposing a pressure gradient, and imposing a fluid flow rate are very important for the radial cell.

Disassembling and reassembling the channel was a major task, requiring up to 18 person-hours of work (from the beginning of disassembly until the system is completely ready to take data again). Three people are required to move the plates during disassembly, and six people are required to move the plates and align the system during assembly. If, after the cell is reassembled and refilled, dust or contamination is revealed by a disturbance of the moving interface, or the onset of secondary instabilities is too low ($1/B \lesssim 3500$), then the entire procedure must be repeated. The complete sequence for cell disassembly and reassembly is:

1. Drain as much oil as possible, remove pump
2. Remove clamps
3. Remove epoxy (buffers), glue
4. Move glass plates off supports (requires 3 people)
5. Thoroughly clean plates, shim-stock (acetone, methanol, distilled water)
6. Clean supports, diffuser
7. Reconfigure supports, diffuser for different cell width (if necessary)
8. Prepare shim-stock with Scotchguard (if desired — usually yes)
9. Re-assemble cell, including careful alignment of plates and shim-stock (requires 4-6 people: 2-3 to move glass, 2 to keep shim-stock in place, 1-2 to use compressed air bottles to remove dust)
10. Re-attach clamps, glue sides (must dry at least overnight)
11. Inspect and adjust cell uniformity using interference fringes under sodium lamp

12. Clean buffers, re-attach using epoxy
13. Clean all glassware (syringes, oil containers)
14. Filter oil
15. Re-attach pump (use new tubing, connectors)
16. Refill cell, remove bubbles
17. Perform image overlap alignment

The lowest aspect ratio that could be reached in this system was $w/b \approx 160$. Larger gap thicknesses could only be obtained with the available shim-stock by stacking three layers of shim-stock atop each other, which would be too difficult to do uniformly. Smaller widths could not be obtained because the clamping system could not clamp securely enough when extended farther from the edge. To obtain lower aspect ratios, a smaller cell was constructed using the same equipment. The support blocks were moved inward to support two plates of 1.91 cm (3/4") thick float glass 101.6 cm (40") long and 12.7 cm (5") wide. Shorter strips of shim-stock, shorter clamp bars, and a shorter, narrower diffuser were cut. The same buffers were used; the extra width was covered with spare acrylic pieces and sealed with epoxy. All other parts of the system (including the optical system described below) were unchanged. Aspect ratios down to $w/b \approx 60$ could be reached in this smaller cell. The root-mean-square variations in gap thickness were typically 0.8% or less in this channel.

4.1.2 Linear Cell Data Acquisition

All data acquisition for this experiment was done with digital imaging. The design of the optical system posed a challenge, because we wanted to view the entire channel while still having high resolution on the interface. The basic idea is illustrated in the system schematic (fig. 4.1). A fixed camera points at a mirror mounted on a shaft. Rotating the mirror allows the camera to image different parts of the cell. A sequence of fixed images of different parts of the cell can then be acquired (grab image, move mirror, grab image, move mirror, etc.). If this is done quickly enough (relative to the interface motion in the cell), then these images can be joined together to create a picture of the entire cell at one point in time.

A schematic of the key component of the optical system, the mirror control, is shown in fig. 4.3. The shaft is designed to hold the 10.2 cm (4") square mirror (utility grade, front surfaced) so that the reflecting surface is on the axis of rotation of the shaft. The mirror is attached to the shaft using the 5-minute epoxy. The shaft is supported by two high precision (ABEC-7) rotary bearings mounted in blocks of aluminum. The stepper motor (Compumotor, motor 006875-02, indexer M57-51, I/O card PCA 71-003901-01) is attached to the shaft via a rigid shaft-coupler. A flexible shaft-coupler was originally used, because a rigid shaft-coupler requires precise alignment of the motor shaft and mirror shaft and is therefore more difficult to set up. However, the flexible shaft-coupler allowed the mirror to vibrate too much; the camera image would be motion-blurred after the sudden stops required to step down the channel.

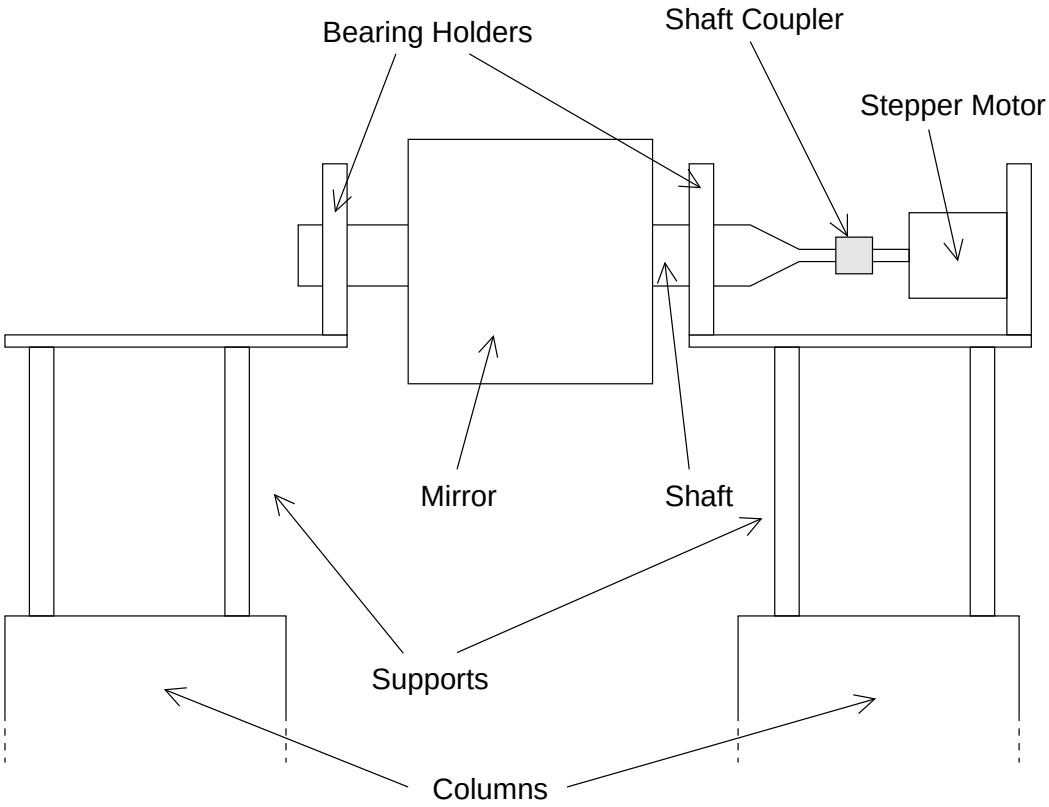

Figure 4.3: A schematic of the optical system for acquiring images in the linear cell, shown from the perspective of the camera, which is 92.7 cm (36.5") away from the mirror axis. A 10.2 cm (4") square mirror is mounted on a shaft on a pair of high precision bearings. The shaft is attached via a rigid coupler to the stepper motor. The entire system is raised high above the cell by a system of columns and supports (cross-braced with the camera supports); the mirror axis is 193.4 cm (76.125") above the center of the cell. Not shown are a cross-piece connecting the two sides at the back so that the shaft isn't carrying any additional load, and an angled black backdrop to eliminate the visual background.

(Appendix A includes designs for the shaft, pg. 187, and the shaft-coupler, pg. 186.)

The entire optical system needs to be raised high above the cell to

reduce perspective effects and eliminate problems with depth of field. A pair of tall aluminum columns were found unused in the lab and were used as a sturdy foundation for the mirror system. A set of cross-braced aluminum poles supplies the rest of the needed height. The bearing holders and mirror holder sit on aluminum platforms, connected at the back with a cross-piece. The camera is supported on a bar atop two long steel pipes attached to the table with aluminum holders. The camera support is cross braced to the mirror supports for stability. The camera height is set by the supports so that the lens's center is at the same height as the center of the rotation of the shaft. The alignment of the camera in the other directions is discussed below.

A 85 mm fixed focal length lens was bought, appropriate for ideal focus on a spot a quarter of the way down the length of the channel (halfway between the end of the channel and the spot directly under the mirror). Even with the long mean optical path created, a high f-stop (small lens aperture) is required ($N = 16$) to have sufficient depth of field to bring both the channel center and ends into focus(see calculations in appendix B).

The camera is a [!!Digital Video Camera Company] DVC-1300 which acquires 1030×1300 10-bit greyscale images at up to 12 frames per second[1]. The camera has a serial computer interface, which (with provided software) allows a number of camera settings to be adjusted, particularly the frame exposure time and the camera gain. The camera is controlled by EPIX video

[1]Though the camera has 10-bit color resolution, we only used 8 bits because of software constraints. This was more than sufficient.

board (model PIXCI-D), using C++ code written using EPIX's XCLIB library interface. The stepper motor that rotates the mirror is also controlled through the computer via low-level I/O commands to an indexer card.

For this image acquisition system to work, the camera and stepper motor must be extremely well synchronized. The camera frame exposure time was shortened to 16.6 ms, 1/5 of the camera frame period (which is set by how fast the camera can read out the data to the computer). The ideal sequence has the camera receive an image for 16.6 ms, then, during the 66.7 ms remaining in that frame, the motor turns the mirror to its next position with enough time left for vibrations to damp down. The system is then ready to begin grabbing the next frame available. Each section of the channel is thus imaged 1/12 s apart.

This ideal was impossible to achieve with this equipment. The stepper motor and it's computer interface dated to the mid-1980's and was thus incredibly slow. When issued a move command, the card took over 30 ms just to calculate the pulse sequence it needed to send to the motor to make the requested move, i.e., there was a 30 ms pause before the motor would even start to move, which was completely fatal to grabbing consecutive frames. Also, the interface to the EPIX frame grabbing card (and perhaps the card itself) was not designed to give precision timing for the acquisition of individual frames, especially consecutive frames. After much tweaking, the system could grab every other frame reasonably reliably; consecutive sections of the channel image were thus 1/6 s apart, and grabbing an image of the entire channel took

1.7 s. The system was theoretically thus limited to studying fingers that did not move appreciably during that time. In practice, you could do much better; the back part of the finger usually evolves very slowly, so only motion at the tip matters. The true image time was therefore really the time at which the last section of the channel image was grabbed. This all breaks down however, if there is significant movement at the back of the interface, as can occur in the pinch-off events discussed in section 7.1.

Because of the high f-stop and short exposure time, a high camera gain was needed to create a sufficiently bright picture. The gain was manually adjusted so that the brightest pixels in the image from the center of the channel (the brightest image) were just below the saturation threshold.

The lab has a set of fluorescent lights immediately above the experiment. These are disconnected to eliminate reflections from those lights off the glass. Reflections from other lab lights are still visible at the ends of the cells, so cardboard blockers are set there during data acquisition.

To avoid changes in the ambient light intensity during data acquisition, the remaining lab lights were left on, with a sign over the switches requesting that they not be disturbed. The experiment was physically blocked off during a run to prevent people from disturbing the system. (I came into the lab one day to find someone leaning against the optical table, completely oblivious to the loud hissing the table was making, much less that this was disturbing an experiment in progress).

With the amount of data collected, a consistent nomenclature is required to avoid confusion. A single picture from the camera, showing just part of the channel, is called a frame. A collection of frames showing a larger section of the channel is called an image. A collection of images taken over time during interface evolution is called a run. A collection of runs taken during one instantiation of the cell (after re-assembly to before disassembly) is called an experiment. Hence the raw image files are named something like `x19_q004.5_r02_i12_f02.bmp`, indicating experiment 19, a flow rate of 4.5 mL/min, run number 2 at this flow rate, image number 12 of this run, and frame number 2 of this image. Similar nomenclature is used for all derived files (e.g., the image formed from the concatenation of all of the frames in the above image would be `x19_q004.5_r02_i12.img`).

The sizes of the steps required by the motor to scan the channel were set manually so that each frame overlapped the next by 1/2" – 1". One limitation of the set-up was that, when viewing the far end of the channel, the ends of the mirrors could be seen in the frame due to the mirror angle. This required several short frames be taken to reach far enough down the channel.

The camera is fixed horizontal at a certain height by the optical setup. It is then still free to move left or right by displacement (i.e., in the y direction) or by rotation (i.e., around the z-axis). The camera is aligned with the mirror by running a thin wire down the center of the channel and adjusting the camera until that wire was vertical and in the same horizontal location in every frame. This will only occur if the camera is centered on the mirror

left-right and aimed perpendicular to the mirror axis. This procedure is quite tedious and fortunately only need be done if the camera is removed.

At the beginning of each experiment, a number of images are taken with various calibration markers (described in sec. 4.1.3.1) on the channel. These are then used to set the parameters for the frame concatenation step of the image analysis (below). After setting the mirror steps and doing the alignment procedure, the motor must keep the mirror in place to ensure repeatability. If the mirror was bumped or the motor suffered a fault or power loss, this calibration procedure must be redone entirely for all later runs. The motor did have a slow drift with repeated use, but it only amounted to a few pixels over the course of an experiment and didn't cause any trouble for the image analysis.

A single C++ program (in Windows console mode) controlled and synchronized the syringe pump, camera, and stepper motor. The program would read lines of parameters from a text file, one for each run to be performed. These parameters (flow rate, withdrawal volume) were manually chosen for each run in an experiment. For each run, the program would initialize the syringe pump and take a background image of the channel with no finger.

The program would then start the pump and begin taking images at regular intervals during the run. The interval was set so as to take 30–40 images over the course of the run. The computer would not image the entire channel at first; the program estimated where the finger tip would be based on an expected width, the flow rate, and the elapsed time and would instead try

to take only those frames where the finger was in view. The program always over-estimated this for safety, so there were still many blank frames in each image, but not as many as there would have been otherwise. The computer saved the frames to disk during the run, so it couldn't perform a scan of the channel faster than every 4–5 seconds — the computer needed that time to write to the disk. For some runs, we borrowed enough memory (384 MB) to allow the entire run to be saved in memory and written later, allowing us to take images about 2 seconds apart. (The computer has since been permanently upgraded to 512 MB of memory.)

The syringe pump's interface seemed to have a delay of about a second in responding to commands, so the apparent $t = 0$ point for each run was not necessarily exactly when the pump started. This was not important for the phenomena studied here so long as the images were separated by constant time intervals.

After the run, the pump would push back a volume of oil equal to that extracted plus a small amount (~ 0.2 mL) to ensure that the interface always began the next run at the end of the channel. The computer would pause briefly to allow the system to settle completely, then automatically perform the next run.

In principle, the experiment could be initiated and left to take an entire data run over the course of several days; in practice, regular monitoring was needed to ensure that various glitches didn't occur. The problems we encountered were: the syringe pump jamming (rare), a fault/power loss in motor

(very rare, fortunately), a bubble in the channel at the start of the run (moderately common at higher flow rates), the interface not being at the channel end at the start of the run, which also usually implies that there is air in the oil buffer (rare, but could happen if the withdrawal volume was chosen too large), and the syringes being nearly out of fluid (common after many runs).

Components of an improved optical system were acquired and partially assembled, but this was never completed and tested. A new mirror 10.2 cm (6") long and 10.2 cm (4") wide was attached to the shaft. The ends of this longer mirror never enter camera view even when viewing the far end of the cell, so viewing the entire length of the cell now requires fewer steps. A new stepper motor (Compumotor, motor OS21B-SNL10, indexer Gemini GT6) was bought but never used. The interface to the motor is much more modern, eliminating the motor reaction time problem previously mentioned. The motor was chosen for its torque and stability specifications, which should be sufficient to turn the mirror fast enough without jitter to allow each section of the channel to be acquired in consecutive frames of the camera. Thus the entire channel could be imaged in 0.75 s instead of 2 s as before. Completing assembly of the new components will be straight-forward; programming the timing to improve the acquisition speed may or may not be.

4.1.3 Linear Cell Image Processing

The data reduction problem in the linear cell is immense. The complete set of raw images we have taken thus far fill up about 400 CDs, approximately

a quarter of a terabyte. The process below describes how this was converted to a set of interface files (consisting of lists of points on the interface). However, even the interface data takes up 1.44 GB *when archived and compressed*.

After a set of runs are taken, all of the frames in that run (several thousand bitmap files) are manually examined. This is not as awful a task as it might seem. Using MicroPlanet's Gravity Image Gallery (part of a Usenet newsreader available free online), it is possible to examine sequential images rapidly and check all the frames in an experiment in 1–3 hours.

The frames are examined this way for several reasons. First, the frames in the background image are checked to see that the interface began at the end of the channel and that there were no bubbles in the channel. If not, that run is discarded (and the following runs will likely need discarding as well). This may require additional runs be performed to replace this data. Second, the camera and mirror motor will occasionally be slightly out of synchronization, resulting in a blurred frame. This usually occurs only a few times over a dozen runs; when it occurs, all the frames in this image are discarded. Finally, because the computer estimates the finger position conservatively when deciding how many frames to take in an image, up to a quarter of the frames in a run may be blank. These are deleted, which can result in gigabytes less raw data, freeing disk space and requiring far fewer CDs be burned for long term raw data storage. The images are then uploaded to one of the Center's Linux computers for the rest of the analysis.

4.1.3.1 Image Concatenation

Several special images are taken before each data run with various calibration markers (described below) on the channel. To set up the parameters for the frame concatenation, a large set of manual measurements are made on these images. This system works because the high precision in the repeatability of mirror positions means that measurements made on these calibration images can be applied to all images in the run thereafter.

The channel width (in pixels) is found by measuring the width at the optical midpoint of the channel (directly beneath the center of the mirror). To find the optical midpoint, an image is taken with a thin wire wound tightly around the columns supporting the mirror and motor. The support design is symmetric front to back, so the center of the mirror is directly above the center of the columns. The optical midpoint is therefore halfway between the wires. The optical midpoint is also needed for later calculations of the length perspective correction.

A ruler was set on the channel at the optical midpoint. By examining this, the conversion from image pixels to physical length scales could be measured. Our resolution was 4.8 pixel/mm, or at least 2–3 pixels per gap depth.

For each frame in one of the calibration images, the four corner points of the cell are taken. Assuming the cell edges appear as straight lines in the frame, we now know the width of the cell in pixels for each row in the frame.

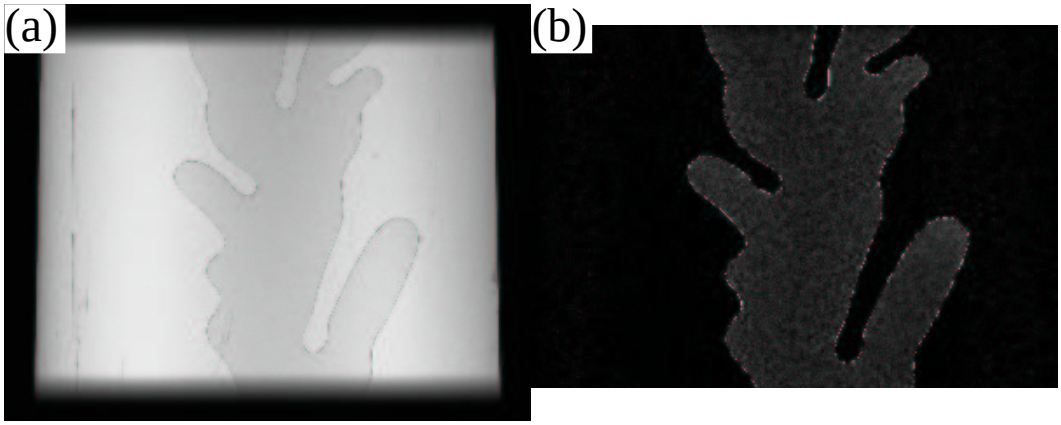

Figure 4.4: (a) A raw frame before any processing. (b) The same frame after background subtraction, inversion, and correction of perspective effects across the width.

When processing the frames, the first step is to subtract the background frame. (Actually, the frame is inverted for convenience in the same step by instead subtracting it *from* the background frame.) The effect of perspective across the width is then corrected by taking each row of pixels and using a bicubic interpolation to stretch it from its current width to the previously found channel width. This step also crops out the part of the image wider than the cell. The frames at the far end of the channel may contain the mirror ends (as mentioned previously); these frames are also cropped during this step to remove that. This changes each frame as shown in fig. 4.4.

The input to the concatenation procedure is simply the number of pixels of overlap between the adjacent frames. The concatenation procedure then simply combines the frames into one image, taking the average of the two images in regions where two frames overlap. The number of pixels to overlap

is determined manually for each pair of frames in an image.

To find this, one of the calibration images is taken with a special grid (printed on transparencies) overlaying the channel (a section of which is shown in fig. 4.5). The approximate overlap amounts are guessed (usually taken from the previous calibration), then the frames are put through the concatenation program and the output examined. The overlap amounts are then refined iteratively. The final value for each pair of frames is always checked against overlapping one pixel more or one pixel less. An example of how this procedure works can be seen in fig. 4.6. After setting the overlap amounts using the grid calibration image, other images are checked to see if they overlap well, and the overlap amounts are occasionally tweaked.

The final processing step is to rotate the combined image so that the interface appears to move from left to right (for convenience sake), then save the image in a file.

Clearly, setting up this image processing procedure involves a great deal of manual configuration. We never found a way to automate the configuration, so it works simply by processing all subsequent images using the parameters from the calibration images. I cannot overemphasize that the success of the procedure relies on the mirror position repeatability.

4.1.3.2 Interface Finding

We now have an image of the channel at one point in time (actually a brief interval, as discussed). From this we wish to extract the position of the

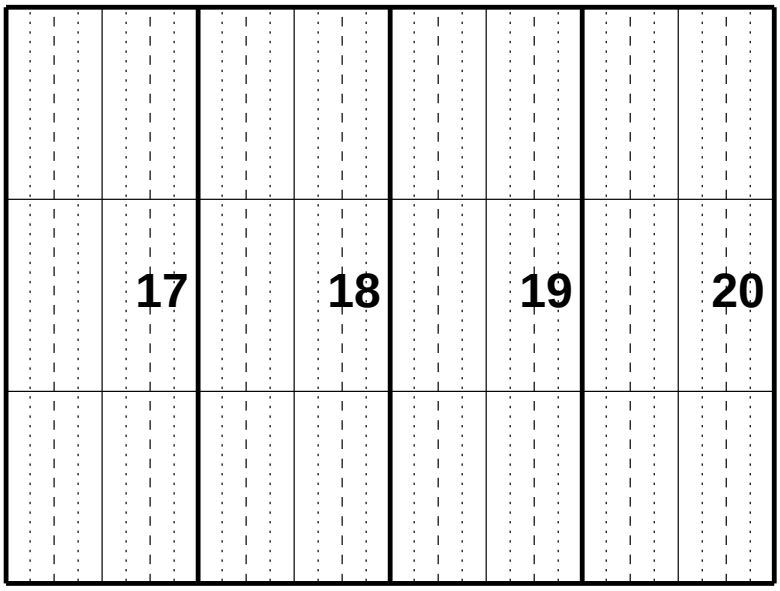

Figure 4.5: A section of the grid overlayed on the channel to aid in the manual determination of the frame concatenation parameters. The markings indicate inches and fractions of inches, but are not used for measurement because they are distorted slightly when printed onto transparencies.

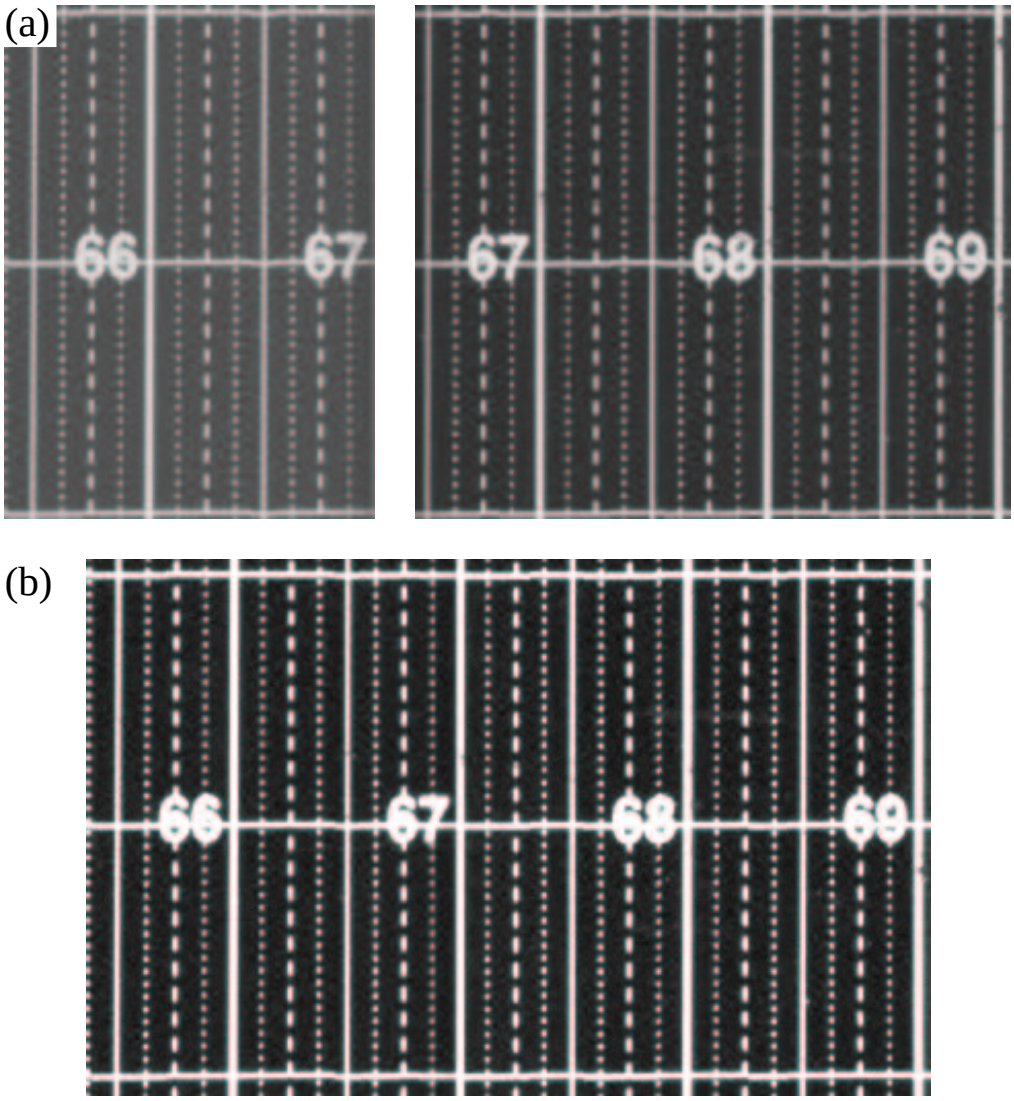

Figure 4.6: (a) Sections from two adjacent processed frames, showing about a half inch of overlap. (The intensity variation between them is mostly an artifact of image processing necessary to create this figure.) (b) The corresponding section of the combined image.

interface as a set of adjacent points.

We quickly realized standard "interface finding" algorithms were not appropriate. These are more properly called edge finding algorithms. They are designed to find "interfaces" like that in the image shown in fig. 4.7(a), i.e., the algorithms find the border between two regions with different intensities. Our images appear like fig. 4.7(b), having two regions of similar (but not identical) intensity separated by a bright line. The interface width in our images is 2–3 pixels at most, on the order of the gap thickness; most typically there is a single pixel much brighter than its side neighbors — that is the interface location. In principle, it might be possible to turn our image into an image like fig. 4.7(a) by integrating along rows and columns; in practice you would really need to integrate perpendicular to the interface, which presumes you know where it is. Some sort of iterative scheme could probably be developed along these lines, but a change in perspective provided another view.

Instead of viewing our images as in fig. 4.7(b), I found it useful conceptually to make the intensity a third dimension and picture our image as in fig. 4.8. The interface is then a ridge; we become hiker/surveyors who wish to follow the ridge line. The algorithm is then quite simple: start taking steps along the ridge; on each step go up as much as possible, or if you can't go up at least go down as little as possible. The program I wrote finds an initial point on the interface by looking for bright pixels along a row. It then steps along the interface in this manner, heading out from the initial point twice in opposite directions.

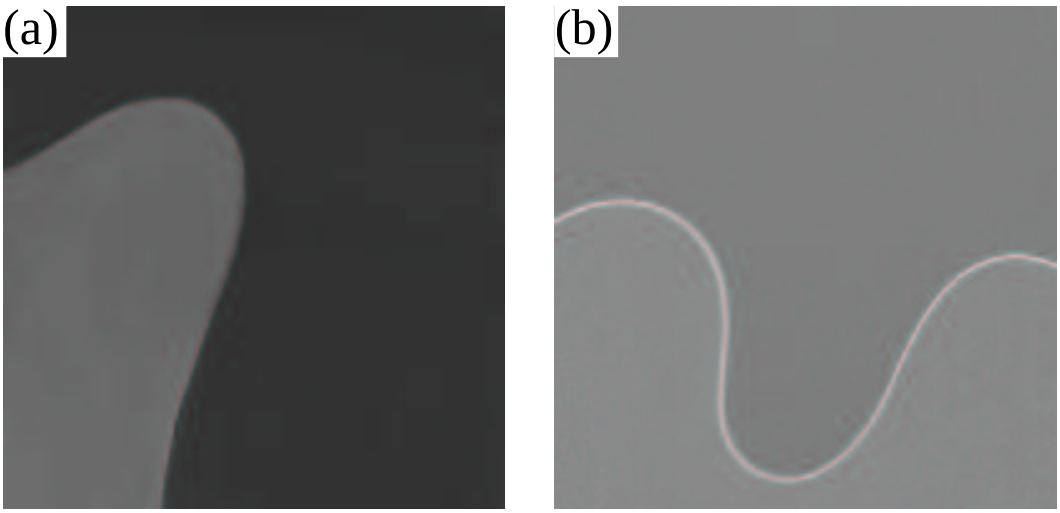

Figure 4.7: (a) An image for which standard edge detection algorithms would be appropriate. They find the curve between two regions of differing intensity. (b) Our interface is instead a thin bright line separating two regions of nearly equal intensity. Standard edge finding algorithms perform poorly here.

The real program has a number of additional subtleties: it has to keep its average direction of travel in mind to avoid getting caught in small loops, it has to re-find the interface if it gets lost in background noise (if there's a space where the ridge is worn down to the level of the noisy "plains"), it has to deal gracefully with self-intersection in some cases without getting caught in an infinite loop, etc.

The result is a list of adjacent x-y integer coordinates, starting with the point nearest the origin (the bottom left corner of the channel). A close-up of the results of the interface tracking overlayed on the original image can be seen in fig. 4.9.

This algorithm has a few limitations. It cannot deal with topological

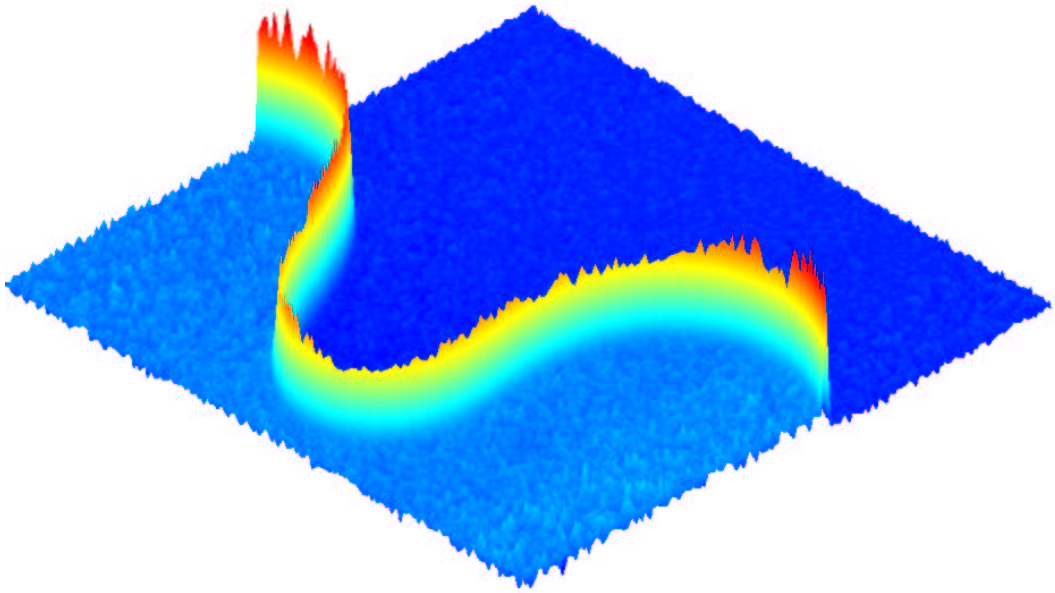

Figure 4.8: The interface from fig. 4.7(b) viewed instead as a three dimensional surface plot with the pixel intensity as the third dimension (in false color). Conceptualizing the interface like this enabled me to find a metaphor (ridge walking) which inspired a simple and elegant interface finding algorithm.

changes, e.g., a finger pinching off to form a finger and a bubble. It only looks for a single connected interface. It might be modifiable to find multiple interfaces, though I suspect this would require a bit of user intervention (at the very least, telling it how many interfaces there are in a given image). The program also cannot deal well with the endpoints at the back of the channel. This is primarily an issue with the original images, which are dimmer and noisier at the very end of the cell (partially because the buffer and glue could be seen behind the last bit of the cell because of the camera perspective).

The effects of perspective were fixed along the width (the y-direction), but not yet along the length of the channel (the x-direction). The formula for

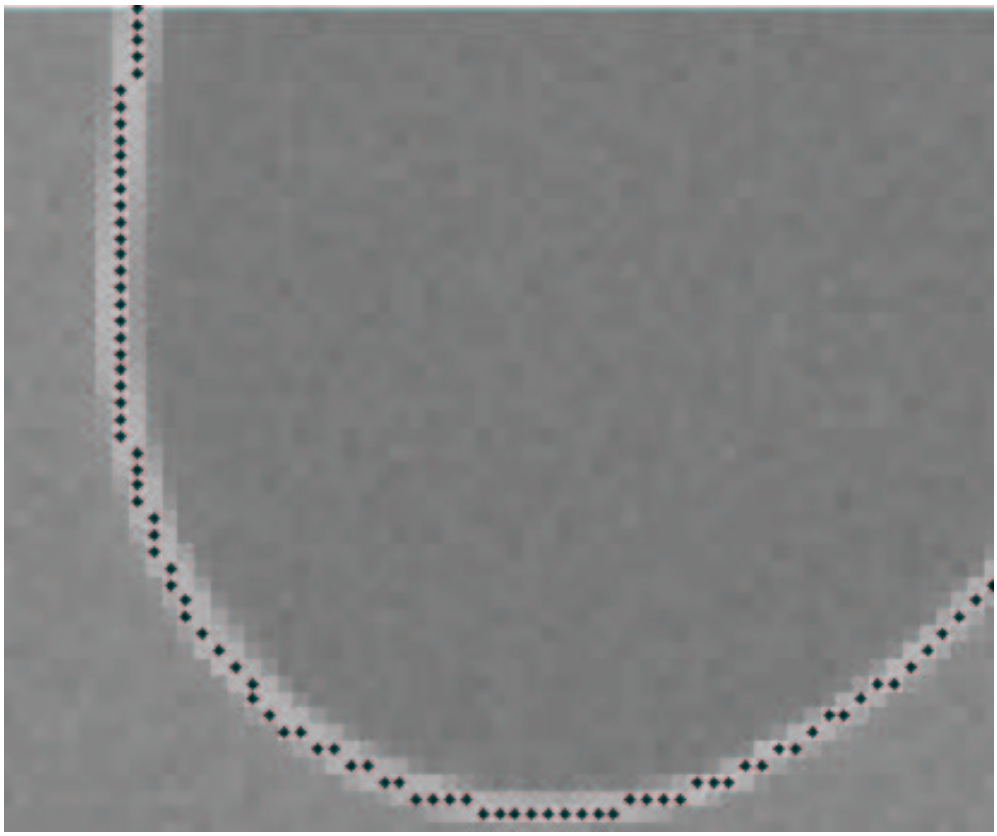

Figure 4.9: The results of the interface tracking program used on fig. 4.7(b), overlayed on a section of that picture. The interface is represented by a list of adjacent points with integer coordinates.

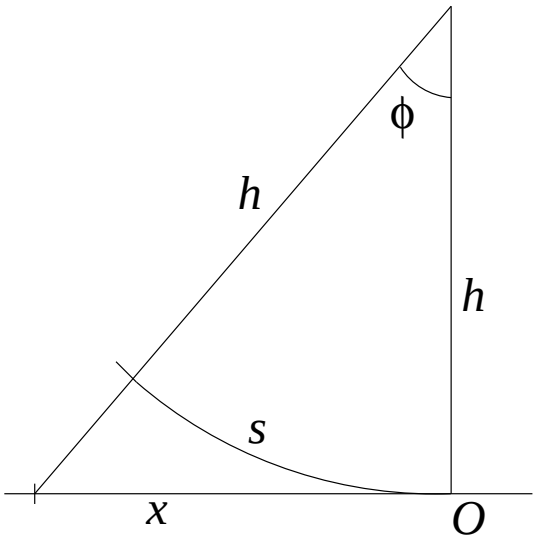

Figure 4.10: A diagram showing the derivation of the formula for the correction of perspective along the length of the linear cell, $x = h \tan(s/h)$.

this correction is simple (see fig. 4.10), $x = h \tan(s/h)$, where x is the new (corrected) x-coordinate relative to the optical origin O, s is the old (apparent) x-coordinate, and h is the optical path length (in this case, the length from the camera to the mirror plus the length from the mirror to the cell). A small correction for displacement due to refraction of light through the top plate of glass is also applied here; see fig. 4.11. Also during this step, the conversion of pixels to physical lengths is done; the resulting output file contains a list of points in millimeters from the origin. From there, they can be analyzed further in any way desired.

For some purposes, particularly calculations of local curvature, we used a smoothing algorithm (a filtering algorithm that is low-pass with respect to curvature) to get sub-pixel accuracy for the interface. We verified that

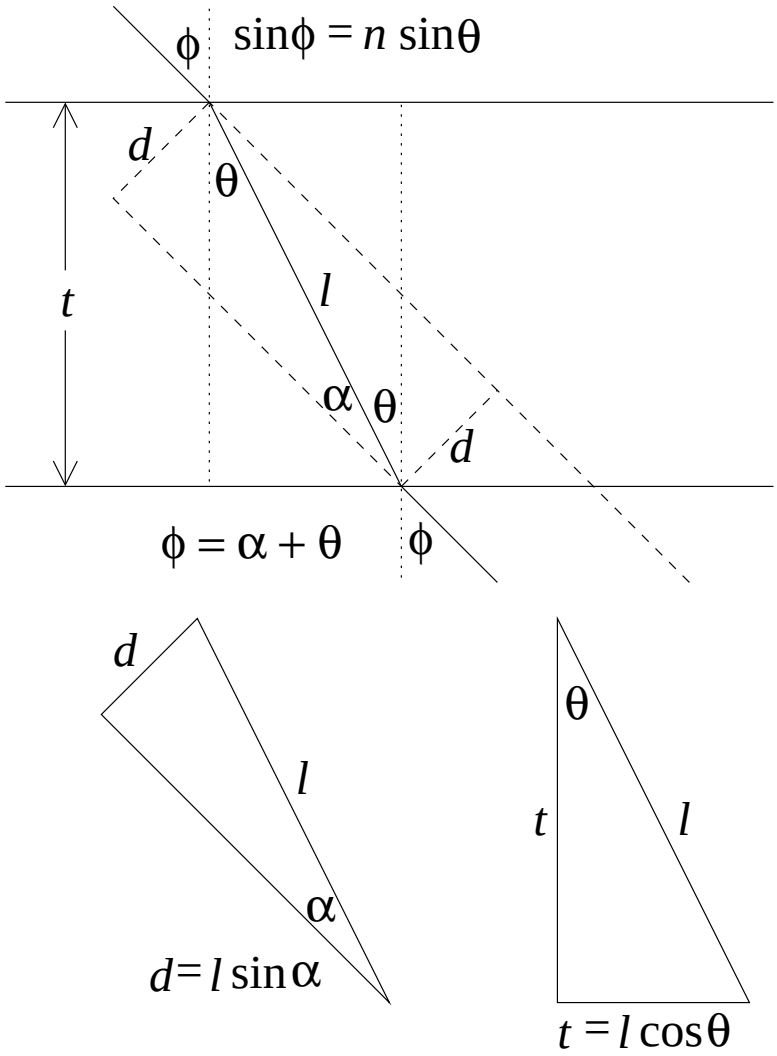

Figure 4.11: Features in the channel will be shifted out a distance d from their true locations because of the displacement caused when refracting through the thick upper glass plate. From the diagram, we can determine that $d = t \sin\phi \left(1 - \cos\phi / \sqrt{n^2 - \sin^2\phi}\right)$, where $\phi = s/h$ from fig. 4.10. Because this is a change in the apparent position, this correction must be applied before the length perspective correction. The effect is small, about a half centimeter at the end of the channel.

rounding the coordinates of the filtered interface gave us back the original interface. However, the optical system has such high resolution that pixel resolution was usually more than sufficient.

Finally, the interfaces are graphed and exported to postscript files, four or five per page, for easier examination. An overview of the entire image processing process is shown in fig. 4.12.

4.2 Radial Cell

4.2.1 Radial Cell Design

The primary design goal for the radial cell was to grow a fractal viscous fingering pattern, more highly branched than any previous experiment had achieved. This required a thin uniform gap, high driving pressures, and high fluid viscosities. Achieving this required an unusually robust cell design. We did improve upon past experiments, as can be seen in contrasting fig. 2.26 and fig. 4.16(a).

An cross-section schematic of the radial system is shown in fig. 4.13. The system was attached to an optical table, but the table was not floated. (One of its legs has a leak which prevents that; we tried to patch it without success.)

The glass plates forming the cell needed to be extremely uniform so a small gap could be used and extremely thick to resist bending because of the imposed pressure gradients. The glass we found for this was from Glass Fab Inc. (Rochester, NY), a company that makes telescope blanks (which are later

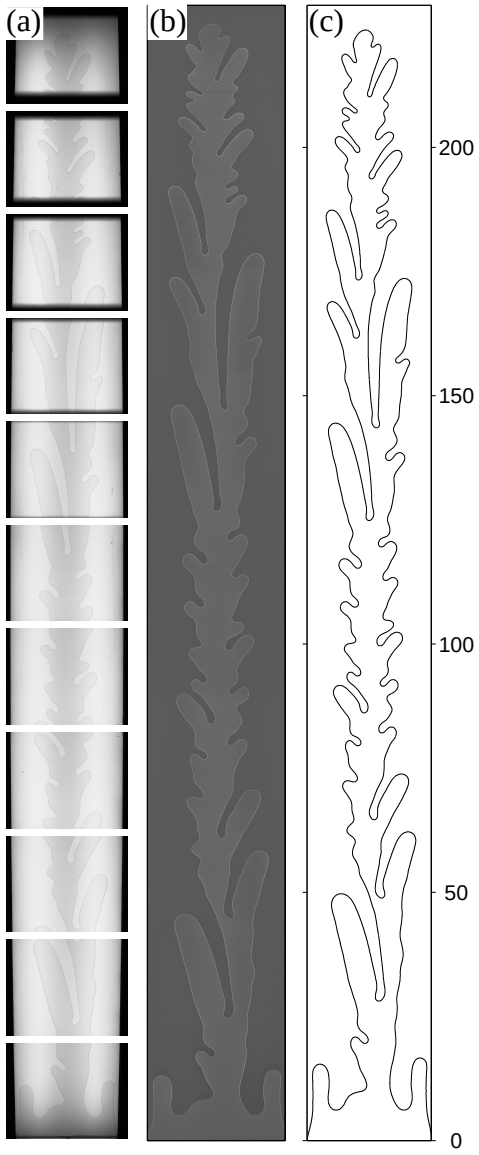

Figure 4.12: (a) A set of raw frames that will form a complete image of the channel. (b) These frames processed into a single image. (c) The interface found from this image after all processing, including the length perspective correction. (That correction is why features on the interface near the channel ends don't line up with the corresponding features on the image.) The numbers on the right are lengths in cm.

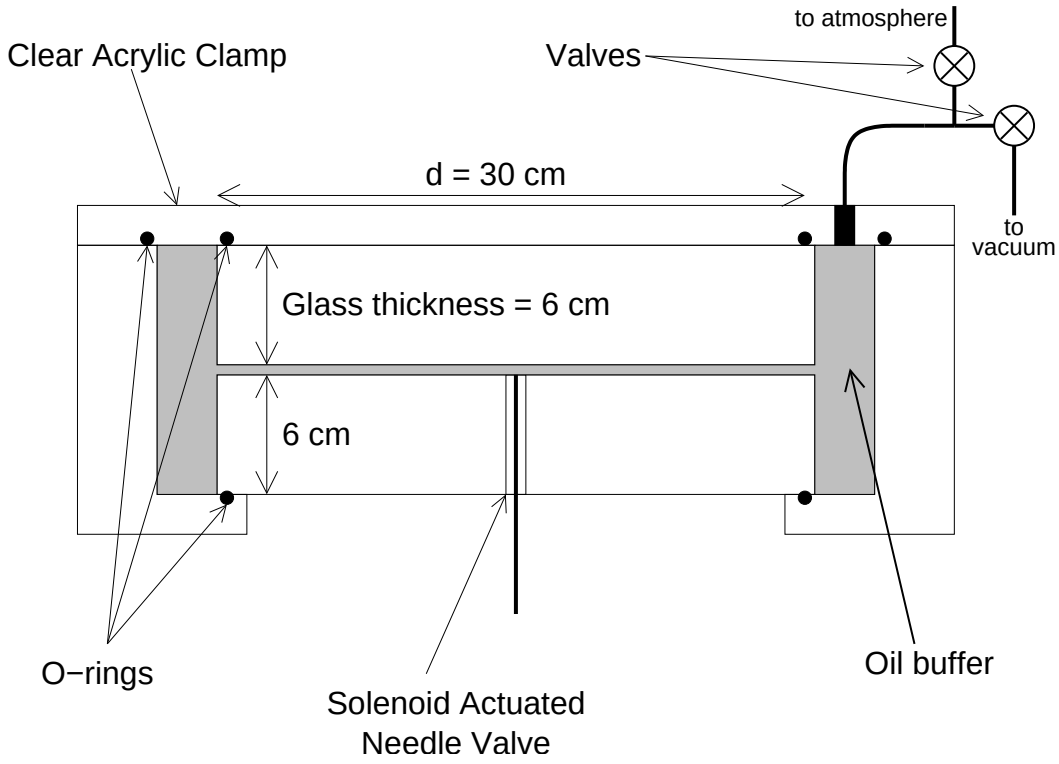

Figure 4.13: A simplified cross-sectional schematic of the radial cell, showing the cell, the glass plates, the surrounding oil buffer, the support and clamps, and the valves that control fluid flow through the system.

ground and polished to become large lenses or mirrors). The pieces are 6 cm thick and 28.8 cm in diameter. They are polished to a quarter wavelength flatness over their entire surface. One of the plates had a 6 mm hole drilled through it at the center for our injection point.

The gap in the cell is created by 16 small pieces of stainless steel shim stock (Precision Brand), each approximately 0.5 cm square. The experiments described here all used 0.127 mm (0.005") thick shim stock. These were placed regularly around the entire edge of the plates.

The cell is enclosed within a large circular aluminum structure. The glass is designed to sit in the center, supported on a 1.34 cm (0.525") wide annular shelf which is 0.635 mm (0.025") below the level of the next part of the cell. This lip was intended to keep the glass in place but proved nearly disastrous later (see below). An 1/8" O-ring rests in a groove in the shelf to seal the bottom of the cell. (Designs for this enclosure are in appendix A, pg. 188–190.)

We place the plate with the injection hole on the bottom, opposite the camera, so that we can avoid the visual interference from the injection hose which is present in *every* radial viscous fingering picture I have ever seen (including fig. 2.26, for example). I still cannot begin to imagine why no one else ever thought of this.

The glass is surrounded by a 1.21 mm (0.475") wide annular volume which is the height of the two glass plates combined (12 cm). This forms a buffer of oil around the cell during the experiment, serving the same purpose as the oil-filled end buffer in the linear system.

There is a drain hole at the bottom of the buffer at one point which can be closed with a 3/8-NPT plug. At mid-height at four evenly placed points around the cell are four access holes, also tapped for 3/8-NPT. These holes are angled upward slightly so bubbles inside would flow easily into the buffer instead of becoming trapped. The original plan was to drive the cell by using a syringe pump to withdraw oil through these holes, but the syringe pump (kd Scientific Model 210, a 2 syringe version of the linear channel pump, also

modified slightly to accommodate the large Hamilton syringes) couldn't pump the oil as fast as we required without stalling. Three of these holes are plugged and sealed shut; the fourth is attached to a syringe (again, Hamilton Gastight 100 mL, model 86020) through a ball valve. This allows us to manually pump oil in and out of the buffer to fill it and remove bubbles, then seal it shut when the experiment is running.

The system is closed, sealed, and held together by a clamp made from 2.54 cm (1") thick transparent acrylic. (Designs for this clamp are in appendix A, pg. 188 & 191.) To seal the top of the cell, the clamp has two grooves for ⅛" O-rings, just inside and outside the annular oil buffer. The clamp is attached to the aluminum enclosure (securing the glass in place) by 24 ⅜-16 bolts. The clamp has one hole through it into the oil buffer, tapped for ⅜-NPT. This was originally to be just an outlet for removing bubbles from the buffer, but after we gave up on using the syringe pump, we used it to attach to the fluid driving system instead.

The clamp was originally intended to be annular, but it proved more useful to keep the central part intact and simply view the cell through the clamp. This made the clamp stronger and protected the top glass plate. The inner O-ring was retained, but mainly to provide a cushion between the clamp and top plate.

This did create a mild assembly problem. Any air trapped in the O-ring grooves is extremely difficult to remove, so we fill the grooves with oil during the assembly process. This however got oil in the viewing area between

the clamp and the top glass plate which interfered with the visualization. Therefore, this gap has to be completely filled with oil without bubbles during cell assembly; it took a bit of experimenting to perfect a technique for doing this.

The O-ring grooves underneath the glass are also filled with oil before cell assembly so that bubbles will not be trapped there. However, during one attempt at cell assembly, the oil on the ledge apparently allowed the glass to slip over so that one edge was resting on the lip which was supposed to keep the glass in place. When the clamp was tightened in this configuration, a pair of cracks, one in each plate, were abruptly created around the nearest piece of shim-stock. Fortunately, these cracks propagated a short distance into the glass and stopped. The cracks create small defects on the surface of the plates in a small area on their edges, but they can just barely be felt by hand. We believe that this does not create a significant disruption of the flow at distant points. To relieve further stress on these points, they are now flanked by shim-stock pieces and placed opposite each other in the cell.

The entire cell enclosure rests on three nuts on three legs, which are 1”-8 threaded rods. These nuts can be adjusted to level the cell. This is again best checked by watching for bubble motion in the cell. Nuts on the rods above the enclosure can then be tightened to hold the cell in place. The bases the rods rest in are attached to the optical table. To remove bubbles from the buffer, it is useful to be able to tilt the entire cell without effecting the levelling adjustment. The leg bases can be unbolted from the table and a screw turned

on one of the bases to raise that end of the cell easily.

The quickest way to eliminate small bubbles from the oil buffer (when the cell is tilted) is to manually withdraw oil from the cell (with the syringe), creating a big annular bubble around the top of the buffer. This will absorb the smaller bubbles. The oil is then re-injected, removing the annular bubble. However, the oil leaves a thick film on the top of the buffer as the annular air bubble is created. This film is immediately Rayleigh-Taylor unstable, so when re-injecting the oil, one must be careful to adjust the inflow rate to account for these drops; otherwise the bubble will pinch off and leave small bubbles behind again. This could only be done manually, not with the syringe pump.

Our first iterations of the experiment used a 1000 cS silicone oil. This proved too viscous; it was difficult to use and had longer time scales for motion than we desired. We used the 350 cS oil listed in table 4.2 for all data acquisition.

We want to drive the system as hard as possible, so we connect the oil buffer to a large bottle pumped down to moderate vacuum (1 – 2 mtorr) by a mechanical pump. This creates the largest pressure difference we can impose via withdrawal alone, i.e., without injecting air into the cell also. Bubbles in the oil buffer are completely fatal to this driving method though. They will expand immensely at the low pressure, and this will offset all the oil volume withdrawn from the system; no oil will come from the cell itself because the resistance to flowing through the cell is so great (because of the thin gap and high viscosity). Only if the entire fluid area is incompressible will withdrawing

oil from the buffer pull oil from the cell.

The fluid flow is controlled by a set of valves. For the injection point, we designed a special needle valve. This valve was glued into the hole in the bottom glass plate. A diagram of this valve is shown in fig. 4.14. This valve presents a flat surface which is set at exactly the surface of the glass plate's interior side. It is closed by a tapered rod that fits into the hole on the valve. Below the hole, the interior part of the valve flares out wider than the rod so that any oil which drains down into the valve will be able to flow out without jamming the rod. The rod is attached to the cell's undercarriage (visible in fig. 4.15). It is held closed normally by a spring but can be pulled down when current is run to a solenoid (scavenged in the lab). The bottom of the needle valve has a hexagonal section so it can be gripped easily by tools; below that is threaded for ⅜-NPT (male) to allow it to be attached to an air supply if injection at greater than one atmosphere of pressure is desired.

At the extraction point, we have a pair of solenoid valves (Graznow 21HN3KY110). The copper pipe leading to these valves is angled so that any bubbles will naturally flow up to and through the valves. One valve opens up to the atmosphere. Opening this allows us to quickly turn off the pressure difference and stop flow in the cell. The second valve connects to the bottle which is our vacuum reservoir. This bottle is large enough that the small volume of fluid pulled into it when this valve is opened will not change the pressure.

The vacuum bottle is also attached to a pressure gauge and to a manual

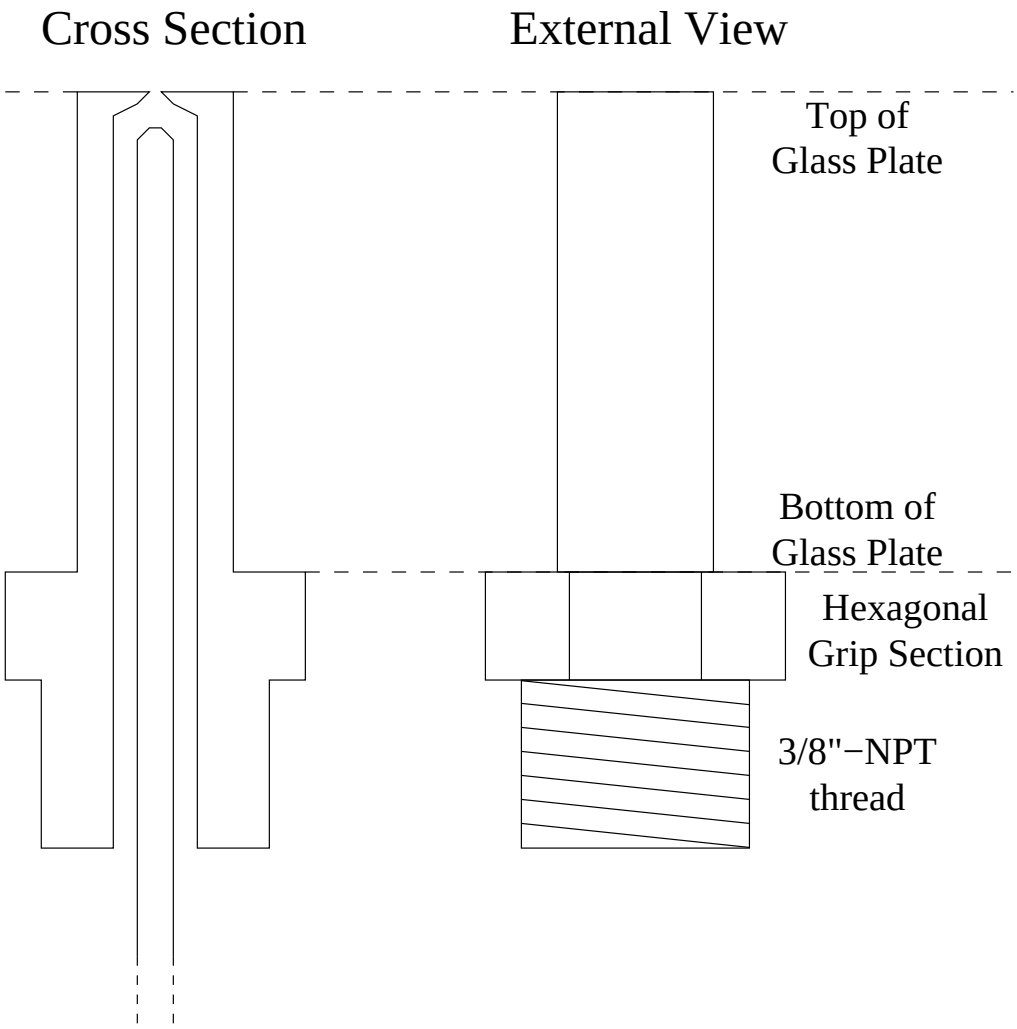

Figure 4.14: A cross sectional and external view of the needle valve. The cross section shows the valve slightly open. Beside the rod which seals the valve there is space for oil to drain out if necessary without blocking the rod. The external view shows the hexagonal section, which is like a nut for gripping, and the ⅜-NPT threaded section. The top of the valve is flush with the top of the plate of glass; this is achieved by making the hexagonal section rest against the bottom of the glass.

ball valve which opens to the atmosphere, which lets us restore atmospheric pressure to the bottle without affecting the system. This valve also let us adjust the pressure in the bottle (after turning off the pump) so that we could perform a special set of experiments at less than full driving.

The solenoid valves and the needle valve can all be controlled by the computer via a National Instruments Data Acquisition (6601 DAQ) board (through a CB68LP connector). This board has a simple C++ interface. Our data acquisition program can thus control the timing of the valves quite precisely and synchronize them with image acquisition as appropriate.

4.2.2 Radial Cell Image Acquisition and Processing

We originally planned to light the cell from below and visualize the interface in the same way we do in the radial cell, but we quickly learned that the cell was so thin that the line of the interface was not easily visible. We then decided to light the cell from above. The index of refraction of the oil and glass are similar, so little light reflects as it passes through oil-filled parts of the cell; these areas appear dark when viewed from above. However, when light passes through air-filled areas in the cell, the index of refraction mismatch creates a strong reflection; these areas appear bright when viewed from above. To enhance this contrast, a black background is attached to the underside of the cell enclosure.

A schematic of the optical setup can be seen in fig. 4.15. The cell is lit by six circular fluorescent lights which are supported by blocks clamped to

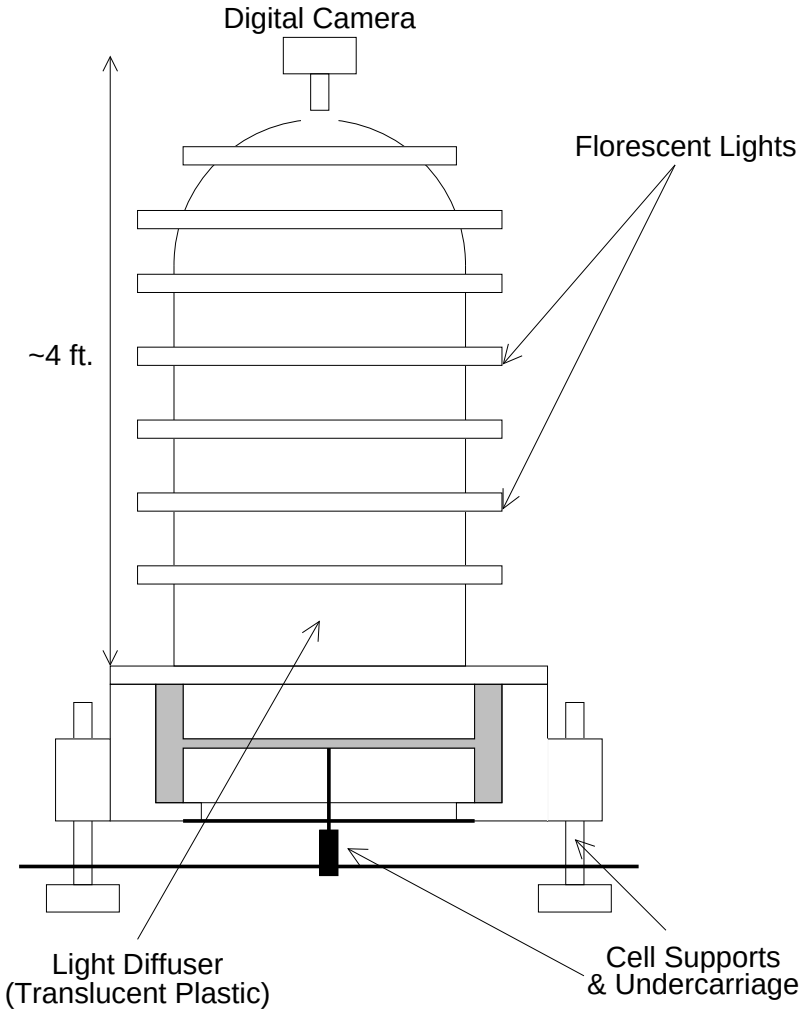

Figure 4.15: A schematic of the optical system for acquiring images in the radial cell.

two tall poles attached to the optical table. These bulbs include five 40 cm diameter, 40 W bulbs (Sylvania FC40W/133 or Phillips FC16T9/CW 40W) with one 25 cm diameter, 22 W (Sylvania FC8T9/CW/RS) bulb at the top.

The light from these bulbs is diffused by passing through a 0.32 cm

(1/8") thick translucent white acrylic piece (obtained from Professional Plastics in Houston, TX), a cylinder 31.5 cm in diameter (outer), 75.7 cm tall, topped with a hemisphere of the same diameter. A small hole is drilled at the top of the hemisphere through which the camera views the cell.

The camera is supported by an assembly attached to the top of the poles that also support the lights. The camera support is designed to easily allow independent motion along all three axes for accurate positioning. The camera is the DVC1300 also used in the linear experiment. It is still controlled by the EPIX video board using XCLIB, its C++ library, but the controlling program is written for Windows GUI mode, since we need to be able to display what the camera is viewing over the course of the experiment. The camera is set for full exposure time (83 ms) and a moderate gain.

We used an adjustable focal length lens ($f = 12.5$ mm – 85 mm, usually set at approximately $f = 20$ mm). While these are often of lower quality than fixed focal length lenses, we had no problems because of that, and it provides us with the flexibility to choose how much of the cell to view. We use a moderate f-stop ($N = 8$) since depth of field is not an issue.

An example of a raw image from the radial cell is shown in fig. 4.16(a) for a highly branched fingering pattern. At the start of each data acquisition run[2], a background image is taken. From this, we manually find the center

[2]The data nomenclature is not as complicated here as it was for the linear cell. The files are named something like `d030112_r02_i12.bmp`, indicating that this is image number 12 of the second run performed on 12 January 2003.

pixel of the cell (easily seen from the hole in the needle valve), the diameter of the valve in the picture in pixels, and the diameter in pixels of the area of the cell actually viewed. For each image in the run, the background image is subtracted, and then the region outside the viewing area is masked off (zeroed) using that data. This creates an image like that shown in fig. 4.16(b).

The diameter of the valve in the picture is combined with the known size of the valve (6.2 mm) to calculate the conversion factor from pixels to physical lengths. Our resolution depends on the zoom chosen for the lens, of course, but was about 4 pixel/mm.

Unlike the images from the linear cell, these processed images are well suited for standard edge detection techniques, including Matlab's `edge` function. For many purposes though, we wished to have the set of all pixels in the air area. This could be obtained by filling in the edge-detected interface (provided the edge detection algorithm returned a closed contour; not all do), but was more easily found by a simple thresholding procedure on the processed image. A histogram of the pixel intensities in fig. 4.16(b) is shown in fig. 4.17. The peak around zero represents the background pixels; the second peak around 25 is generated by the brighter pixels within the fingering pattern. The minimum between these peaks is always clearly defined, and it was taken as a thresholding point: all pixels with intensities lower than or equal to the value at this minimum were set to zero; all pixels with intensities higher than this were set to one. A binary image is obtained, as shown in fig. 4.16(c).

One limitation of this method that can be seen immediately is that,

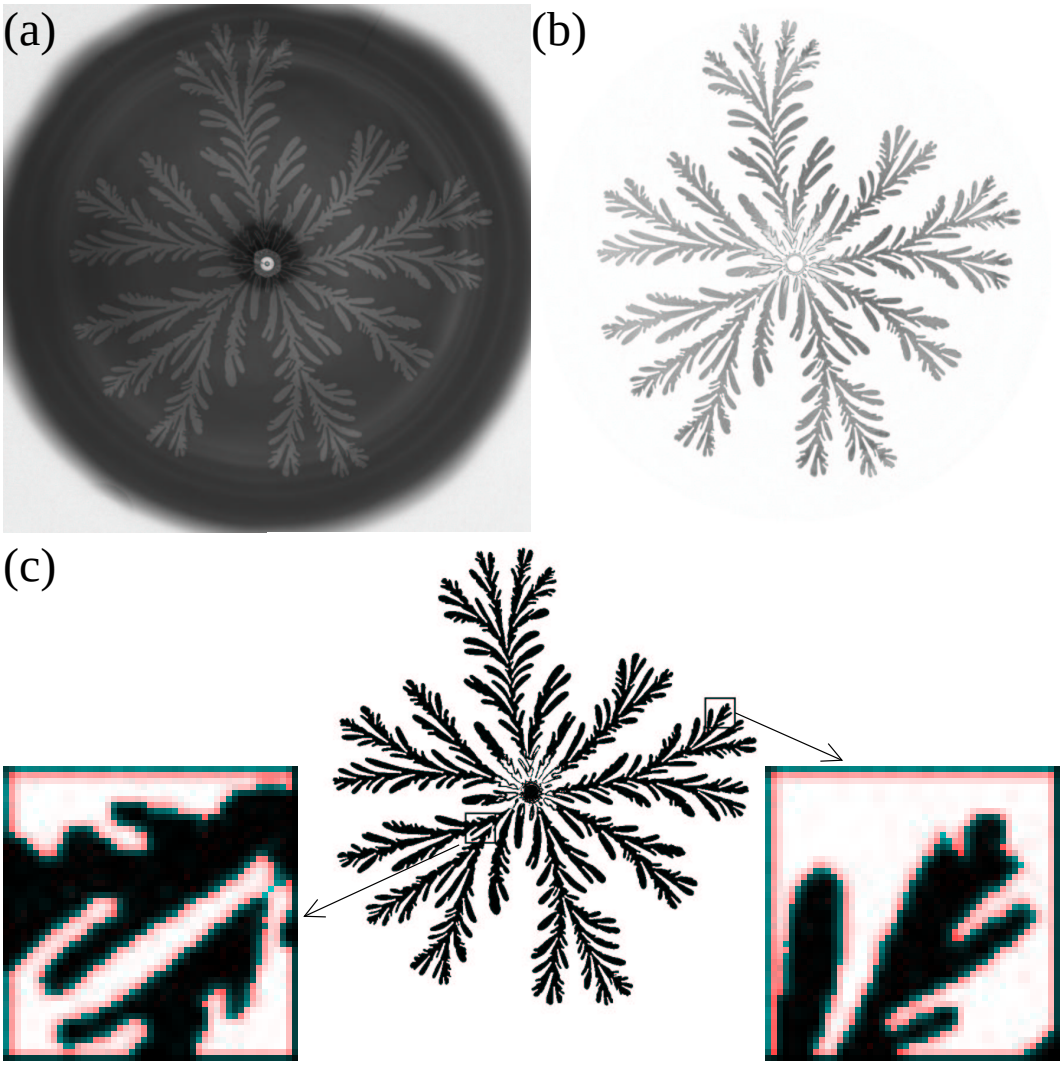
(a)
(b)
(c)

Figure 4.16: (a) A raw image from the radial cell showing a highly branched fingering pattern. The bright edge around the image is the light diffuser. Some unevenness of the lighting is still present in the cell but is eliminated during the background subtraction. The shadow of the camera lens can be seen as a darkened area in the center of the cell. Closer to the center, the hexagonal grip of the needle valve can be seen underneath the cell. The needle valve and its hole are at the exact center. (b) The image from (a) after a background image has been subtracted and the outermost regions masked off. The interference from the shadow of the camera lens is clearly noticeable. (c) The image from (b) after it has been thresholded as described in the text. The valve area has been filled in also. The two sub-pictures are close-ups of the boxed areas, showing the effects of the pixelization. Each box is 50 pixels square, which is 12.9 mm or 102 times the gap thickness.

while there is a definite minimum between the background and pattern pixel intensity distributions, the contrast isn't sufficient to make the distributions go completely to zero there. Thresholding at that point thus means some background noise pixels are kept and some pattern pixels are discarded.

Another obvious limitation (for both thresholding and edge detection) is the dark central region caused by the shadow of the camera lens. While we were able to reduce the area, it always affected some part of the central image. The contrast in this region is extremely low, and though the human eye could sometimes detect the interface here, no computer algorithm was ever reliable. (The human eye could also be fooled and see a line of thick film where the interface was once as its present position.) Closer to the center, the hexagonal gripping section of the needle valve is in the background, further disturbing the image.

A final limitation (again for both methods) is pixelization: the points of

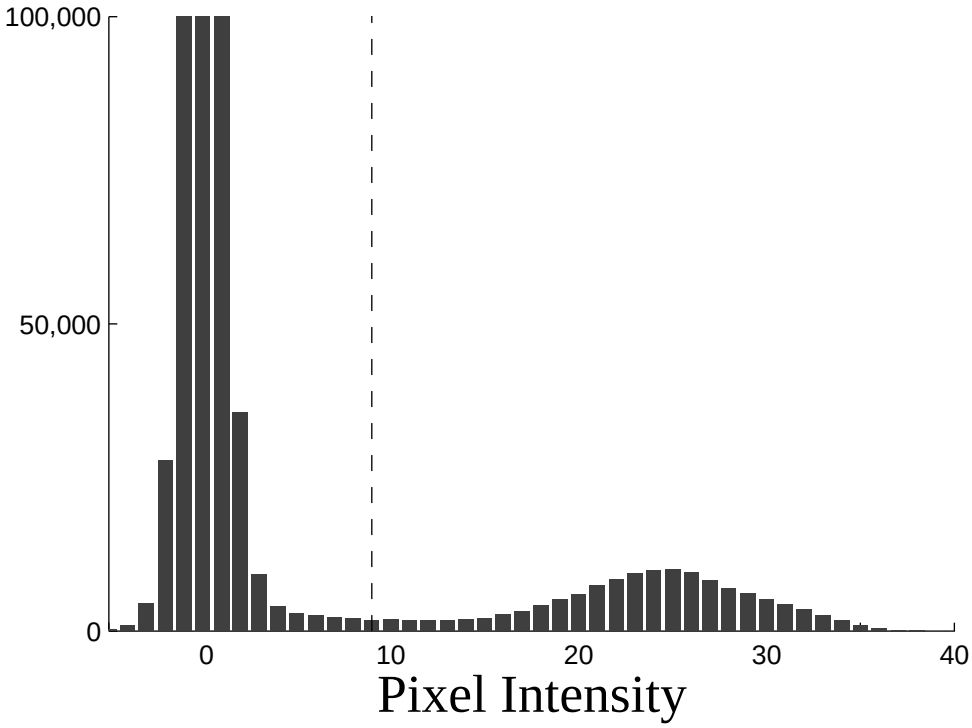

Figure 4.17: A histogram of pixel intensities seen in the background subtracted, masked image, fig. 4.16(b). The first peak represents the background contribution; the three bins near zero are heavily truncated, as the picture has 1048576 (1024 × 1024) pixels. The broad second peak represents the fingering pattern. The dotted line is drawn at the minimum between these peaks, which is used as a thresholding point.

the cluster (or the interface) are always discrete units with integer coordinates. Very small features in the image were thus quite blocky in appearance. In principle, this could have been improved by higher resolution, a sub-pixel accuracy edge-finding routine, or a smoothing algorithm (like we tried for the linear cell interfaces). But in the end, we found that this didn't pose a particular problem for the results described later.

Chapter 5

Fluctuations in Viscous Finger Widths

After we assembled our cell, the first thing we looked for was the classic half-width finger of Saffman and Taylor [122] (see chapter 2). Instead, we saw a finger like that in fig. 5.1! We first thought that this must an experimental problem and made many refinements to the cell (discussed in chapter 4), but the phenomenon persisted and became more robust. We discovered some regularities to the odd behavior of the fingers and realized we had uncovered a new phenomenon: fluctuating viscous fingers [98, 99].

These fluctuations in the width of the evolving viscous fingers have not been reported in previous experiments [122, 135, 106, 64] nor predicted theoretically. The fluctuations intermittently narrow the fingers from their expected

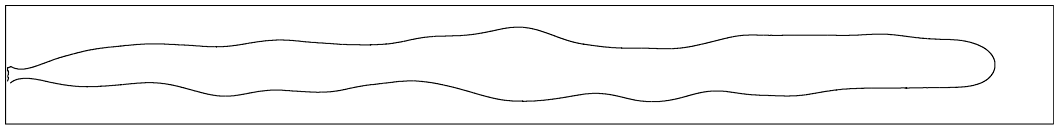

Figure 5.1: An oddly behaved finger in a flow regime where a steady, straight finger would be expected. This was observed in a cell with aspect ratio $w/b = 490$. Its tip velocity was $V = 0.276$ mm/s, giving it a modified capillary number of $1/B = 374$. Its average width (relative to the channel width) is 0.461, while its maximum width is 0.571. (These quantities measured as discussed below.)

width and are largest at low capillary number Ca, falling off as a power law with increasing Ca. Further, at large aspect ratios, the fluctuations are accompanied by substantial departures from the monotonic dependence of the finger width on $1/B$ found previously [135, 41, 85, 86]: for aspect ratios $w/b \gtrsim 250$, which were not examined in previous work, we find that the mean finger width no longer scales monotonically with $1/B$; for smaller aspect ratios, our finger width measurements are in accord with previous results. Because large aspect ratios should more closely approach the ideal of two-dimensional flow, our observations pose a challenge to the assumptions underlying theoretical analyses of viscous fingering.

5.1 Data Analysis

For each experiment we performed (recall nomenclature of section 4.1.2), we took data over a wide range of flow rates. For each flow rate, up to four runs (time sequences) with 20–30 digital interfaces were recorded.

For each interface image in the time series with a single, well developed finger, we found the instantaneous finger width by averaging measurements taken in a narrow window that was 5% of the channel width beginning 1.2 channel widths behind the tip. (See fig. 5.2.) This measurement window was chosen to be small compared to the length scale of the fluctuations (approximately a third of a channel width); the results were not sensitive to the window's exact location. From each time series of instantaneous widths, we determined the time average $\langle\lambda\rangle$ and the root-mean-square (rms) fluctuation

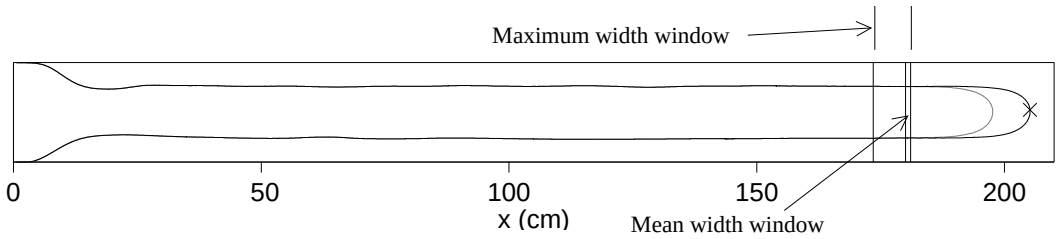

Figure 5.2: We measure several quantities on each interface with a well developed finger. We find the tip position ($\times$) for each interface and find the tip velocity by taking the slope of the fit line for position *vs.* time. We find the finger width for each interface by looking in a small window 1.2 channel widths back from the tip (front pair of lines) and averaging width measurements across that window. Finally, we find the maximum width for a given interface by looking in a window that begins 1.2 channel widths behind the current tip position (front line) and ends 1.2 channel widths behind the previous interface's tip (previous interface is grey, end of window is back line).

from the mean δ_λ.

We also wanted to find the maximum width obtained in the run but without letting the relaxation/drift of the back of the interface affect our measurement. To do this, for each interface in the time series we found the maximum width observed in a window beginning 1.2 channel widths behind the tip and ending 1.2 channel widths behind the previous (in time) tip position. (See fig. 5.2.) We then took the maximum width $\lambda_{\max}$ as the maximum of these values.

We calculate the tip velocity for each run by finding the tip position for each interface and taking the slope of the best fit line for position *vs.* time. From this we calculate the capillary number $\mathrm{Ca} = \mu V/\sigma$ and the modified capillary number $1/B = 12\mu V w^2/\sigma b^2$.

Each experiment was analyzed for flow rates up to the point of tip splitting, beyond which the finger width λ was no longer well defined. However, the first tip instabilities observed with increasing $1/B$ are asymmetric narrowing modes, not actual splitting (section 2.5), and this instability is difficult to distinguish from the fluctuations by eye. Because of this, our data at high $1/B$ include values averaged over such instabilities.

Finger widths determined in consecutive runs agreed within the measurement accuracy. Mean width values agreed within 0.5% for data sets repeated after channel disassembly, cleaning, and reassembly (i.e., for different experiments at the same aspect ratio). Our high image resolution generated finger width values accurate to 0.1% in the larger channel and 0.3% in the smaller channel.

5.2 Results

Typical interface image sequences are shown for $w/b = 158$ and 490 in Fig. 5.3. For both aspect ratios the finger width λ fluctuates visibly at low flow velocities (Fig. 5.3 (a),(c)). In the smaller aspect ratio system the width appears to become steady as the finger velocity is increased (Fig. 5.3(b)), appearing exactly like the classic "half-width finger" of Saffman and Taylor. However, with sufficient resolution, fluctuations can still be measured for all velocities up to the onset of tip instabilities. In the higher aspect ratio system the width fluctuates visibly for all flow rates (Fig. 5.3(d)). The onset of tip instabilities in both cases occurs at $1/B \approx 4000$, similar to values seen in

previous experiments [135, 106, 64].

For all the aspect ratios studied, we find that the rms fluctuation of the finger widths is described by $\delta_\lambda = A(\mathrm{Ca})^\beta$ with $A = (1.1 \pm 0.3) \times 10^{-4}$ and $\beta = -0.64 \pm 0.04$, as fig. 5.4 illustrates. We also observe that the instantaneous velocity of the finger tip fluctuates from the average velocity; within the experimental uncertainty these velocity fluctuations scale with Ca in the same manner as the width fluctuations, as shown for one channel configuration in fig. 5.5. Interestingly, a dependence of the form $\mathrm{Ca}^{-2/3}$ appears frequently in theories of viscous fingering [13, 51, 109, 37, 134, 105].

The fluctuations in finger width are accompanied by a substantial deviation from the expected relation between finger width and velocity. Our results for the width of the viscous fingers for high w/b are not described by a single curve as a function of $1/B$ as predicted (section 2.4.1), and the differences between data for different aspect ratios are far greater than those reported previously for low w/b [135]. Fig. 5.6 illustrates this, showing the dependence of the mean finger width $\langle\lambda\rangle$ on $1/B$ for values of w/b between 58.4 and 490.

In particular, the mean finger width exhibits a surprising maximum as the tip velocity is decreased for large aspect ratios (fig. 5.6, 5.7). The value of $\langle\lambda\rangle$ at the peak, $\langle\lambda\rangle_{\mathrm{peak}}$, is plotted *vs.* w/b in the inset of fig. 5.6.

To further compare our work with past results, we must account for the film-wetting effects discussed in section 2.4.3. We use Tabeling and Libchaber's correction to the modified capillary number, $1/B^* = (1/B)/[\pi/4 +$

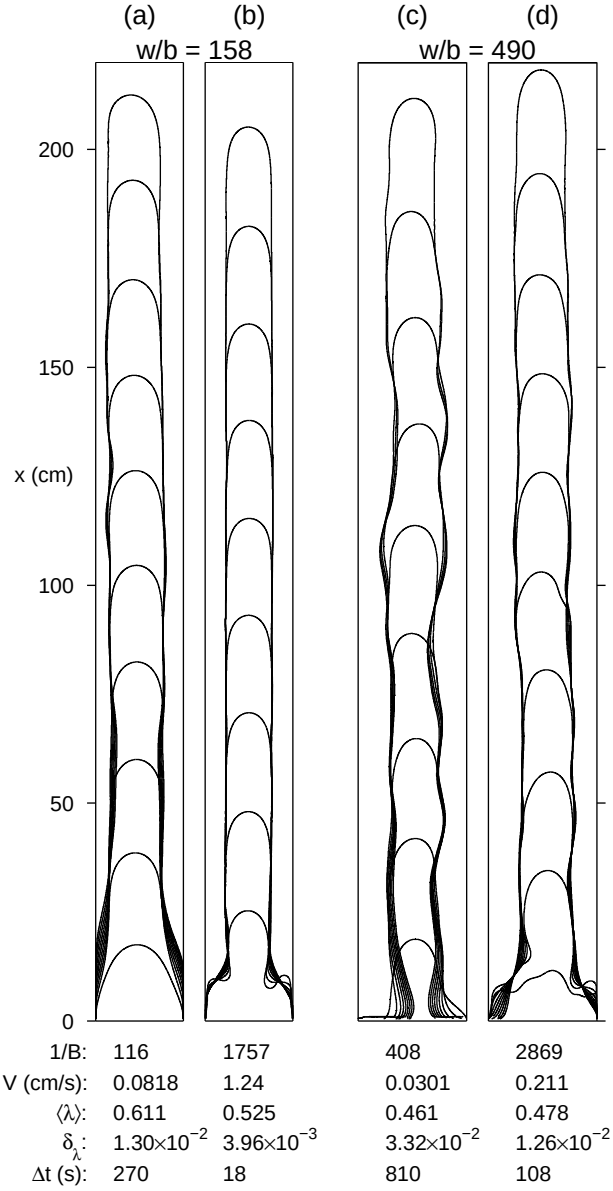

Figure 5.3: Finger images recorded at regular time intervals for different values of aspect ratio w/b and modified capillary number $1/B$, with corresponding values of the tip velocity V, the mean finger width $\langle\lambda\rangle$, the rms fluctuation of the finger width δ_λ, and the time Δt between successive curves.

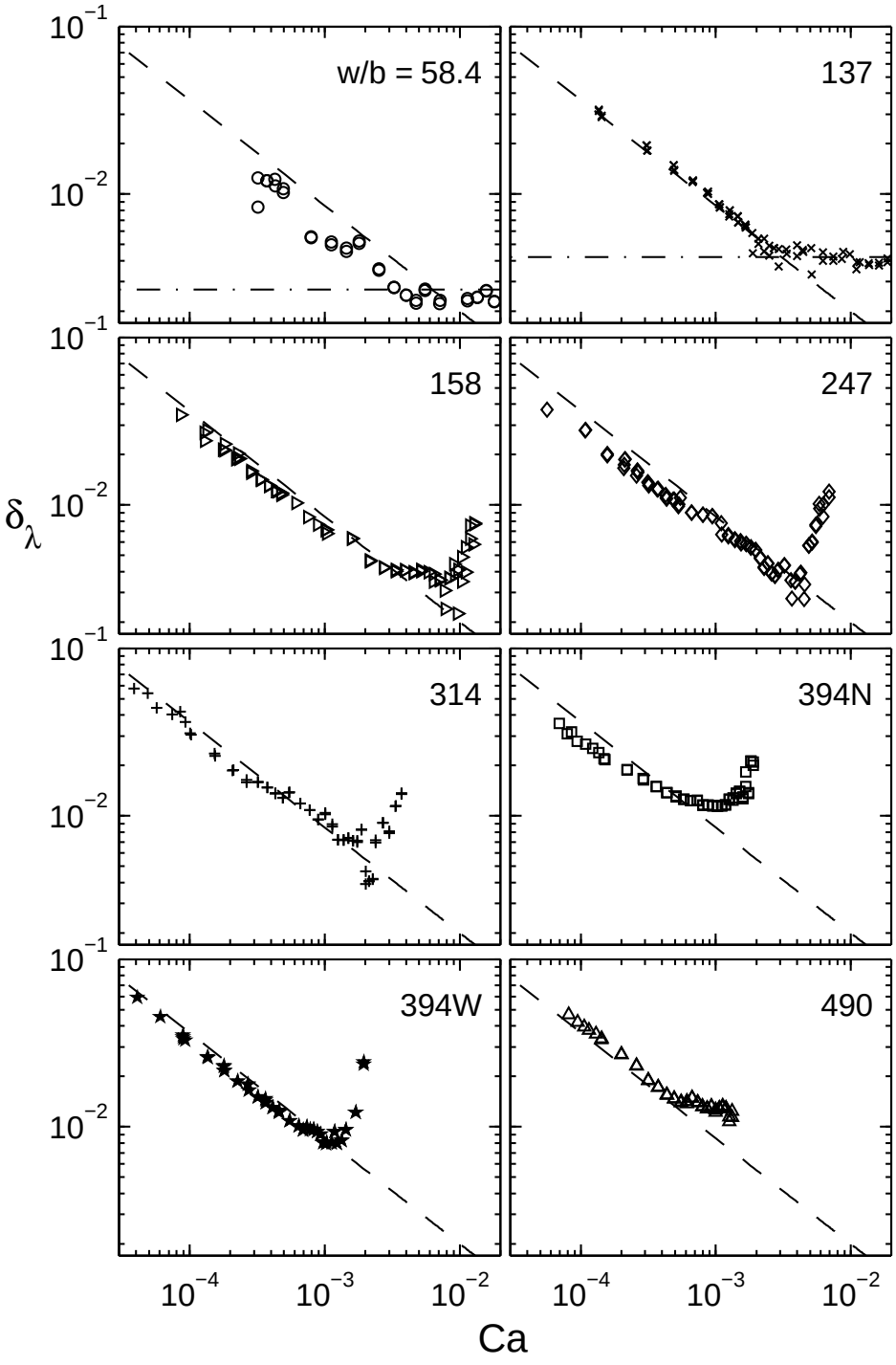
w/b = 58.4
137
158
247
314
394N
394W
490
δ_λ
Ca
10^{-1}
10^{-2}
10^{-3}
10^{-4}

Figure 5.4: The rms fluctuation of finger width δ_λ as a function of capillary number Ca, where the dashed lines describe the best fit to all of the data sets within the observed scaling region, $\delta_\lambda = (1.1 \times 10^{-4})\mathrm{Ca}^{-0.64}$. (The data for 394N and 394W have the same aspect ratio but different widths; see caption of fig. 5.6 or table 4.1.) The horizontal dash-dotted lines in the top two graphs correspond to the limits of measurement accuracy for that channel and geometry; this limit is below the lower edge of the graphs for the other data sets. Fluctuations with $\delta_\lambda \lesssim 10^{-2}$ are not obvious visually. An upturn in δ_λ occurs at high Ca, signalling the onset of the secondary instabilities in the tips of the fingers.

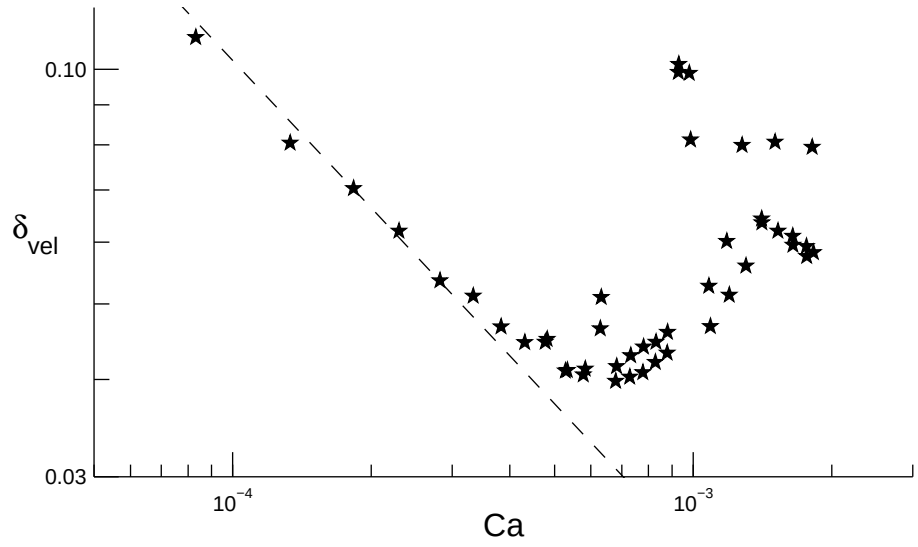

Figure 5.5: The rms fluctuation of the instantaneous finger velocity over time δ_{vel} as a function of capillary number Ca for a channel in the 394W configuration. The dashed line follows $\mathrm{Ca}^{-0.64}$, showing that the velocity fluctuations scale with Ca in the same way the width fluctuations do.

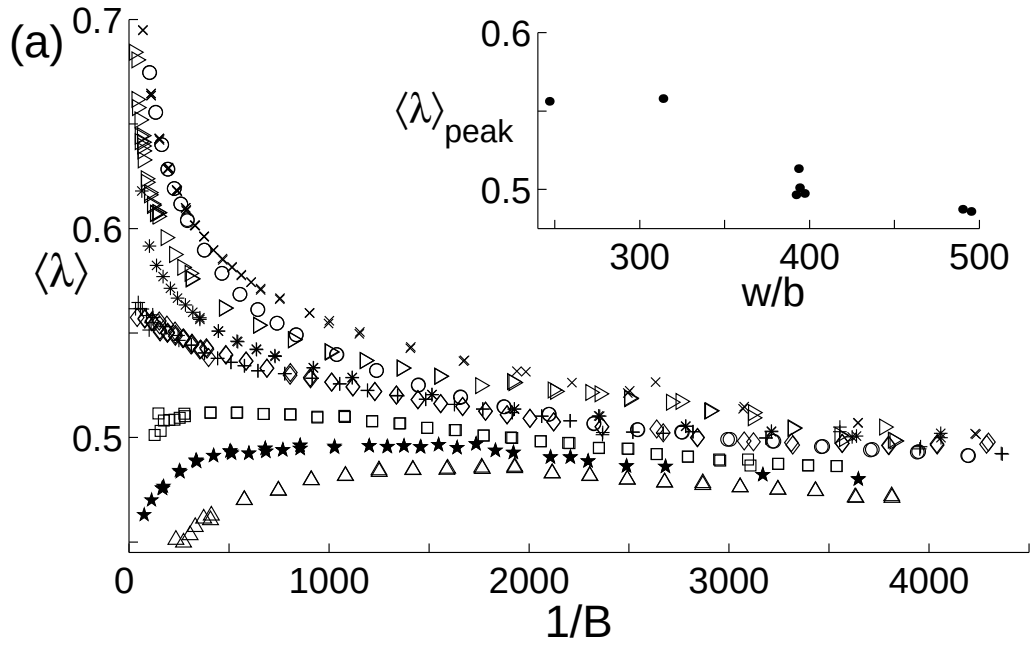

Figure 5.6: Mean finger width $\langle\lambda\rangle$ *vs.* $1/B$ for various aspect ratios w/b. Higher aspect ratios give smaller $\langle\lambda\rangle$ values. The large w/b data exhibit a peak width $\langle\lambda\rangle_{\rm peak}$ as a function of $1/B$; the inset shows dependence of $\langle\lambda\rangle_{\rm peak}$ on aspect ratio w/b. Aspect ratio symbols: $\circ$ 58.4 ($w = 7.4$ cm), $\times$ 137 ($w = 7.0$ cm), $\triangleright$ 158 ($w = 20.1$ cm), $*$ 214 ($w = 22.6$ cm), $\Diamond$ 247 ($w = 25.1$ cm), $+$ 314 ($w = 19.9$ cm), $\square$ 394N ($w = 20.0$ cm), $\star$ 394W ($w = 25.0$ cm), $\triangle$ 490 ($w = 24.9$ cm).

$\alpha\lambda(w/b)(\mathrm{Ca})^{2/3}]$ [134, 105]. (Tabeling and Libchaber found the adjustable parameter α by fitting; we use their value $\alpha = 1.7$.) Using this correction, they obtained agreement between their experimental measurements of λ and the theoretical predictions of McLean and Saffman [85, 86] for $1/B^* < 100$ ($1/B < 250$) (fig. 2.15); we obtain similar agreement for $w/b = 58.4$, as the inset of fig. 5.7 illustrates. Fig. 5.7 shows the dependence of the mean finger width $\langle\lambda\rangle$ on $1/B^*$ for all aspect ratios. At high $1/B^*$, the film wetting correction also collapses the data to a common curve for all $w/b > 58.4$, though a slight displacement downward of the large w/b data remains.

While our $\langle\lambda\rangle$ results do not exhibit the classical scaling with $1/B^*$, the maximum value of the fluctuating finger width observed during finger evolution, $\lambda_{\max}$, does, as shown in Fig. 5.8. $\lambda_{\max}$ does not exhibit a peak with decreasing $1/B$, and while $\lambda_{\max}$ has more statistical noise than $\langle\lambda\rangle$, the $\lambda_{\max}$ data collapse onto similar, monotonically decreasing curves that agree with the McLean-Saffman prediction at low $1/B^*$. The $\lambda_{\max}$ data fall below the McLean-Saffman curve at high $1/B^*$, but not as much as the data for $\langle\lambda\rangle$. These $\lambda_{\max}$ data suggest that the fluctuations represent an intermittent narrowing of the fingers from their "ideal" width.

The finger width fluctuations and the peak in $\langle\lambda\rangle$ versus $1/B$ have proven robust under many variations of experimental conditions. Both high and low viscosity oils gave the same results for the same geometric configuration. Changing the contact angle where the interface is pinned at the back of the channel (see section 4.1.1, pg. 84) again gave the same results for the same

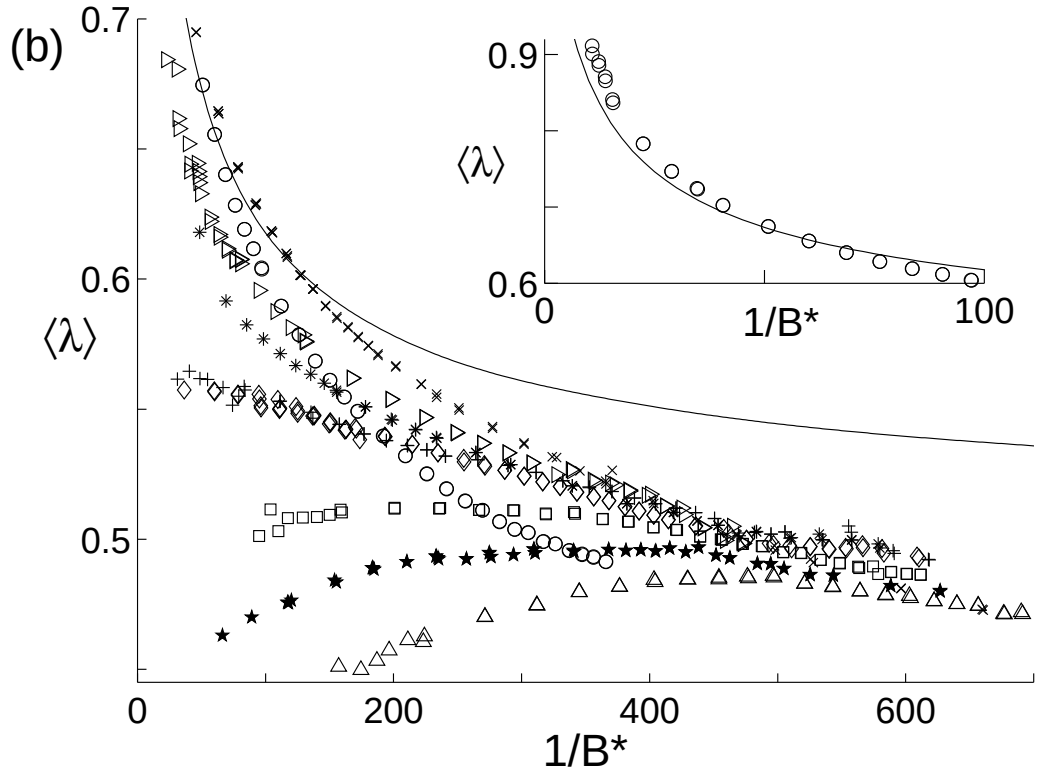

Figure 5.7: Mean finger width $\langle\lambda\rangle$ *vs.* $1/B^*$, which includes film wetting corrections. The solid line is the theoretical curve of McLean and Saffman [85]. The inset extends the $w/b = 58.4$ curve to lower forcing. Aspect ratio symbols are same as in fig. 5.6.

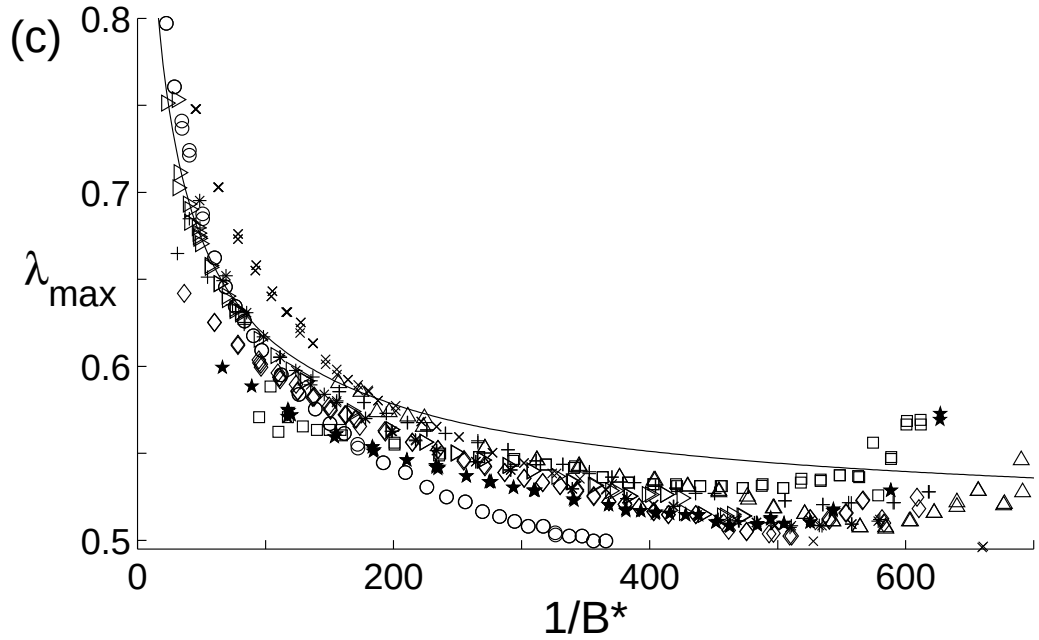

Figure 5.8: Maximum width $\lambda_{\max}$ of the fluctuating finger width observed during evolution as a function of $1/B^*$. Data for $w/b > 137$ collapse roughly onto the same curve, which follows the McLean-Saffman theory more closely than the low aspect ratio results. Aspect ratio symbols are same as in fig. 5.6.

geometric configuration. (The difference between the two types of pinning can be seen between fig. 5.3(b) and(c).) To ensure that the syringe pump was not imposing the observed velocity fluctuations, we pumped one data set by gravity siphoning (see section 4.1.1, pg. 90), again with identical results.

The effect of variations in the gap between the plates was examined for several aspect ratios by over-clamping the channel along the sides, which increases the intrinsic gap variations by a factor of 2.5 (measured interferometrically); both the finger width fluctuations and the location of $\langle\lambda\rangle_{\text{peak}}$ with respect to $1/B^*$ were unchanged, although $\langle\lambda\rangle$ values decreased by about 4% near the peak.

Though the fluctuation power law we observed remained unchanged for *all* experimental variations, we did discover that measurements on two channels with $w/b = 394$ but different values of w and b yielded different results. The $\langle\lambda\rangle$ values for both set-ups departed the common curve at approximately the same point with decreasing $1/B^*$, but at lower $1/B^*$ the behavior was different – compare 394W (394-wide) with 394N (394-narrow) in Fig. 5.7. This difference suggests that either the width for a given w/b and Ca is not unique, or perhaps a third parameter, as yet unknown, is necessary to describe the problem for high w/b and/or low Ca. Consistent with this are the $\langle\lambda\rangle$ data for $w/b = 247$ and 314, which superpose closely even though they have no geometric parameters in common.

It is unlikely that the fluctuations are caused by an instability of the film wetting layer because the film is very thin at low capillary numbers, where the

fluctuations are largest. Film wetting fluctuations would also cause deviations in the growth rate of the area of the fingers, which we do not observe. (While the film wetting laws break down at high and low Ca (section 2.4.3), they do not do so in a way that would explain our fluctuation results).

We speculate that the fluctuations in finger width may be a consequence of long-time relaxations of the interface at the back of the channel, observable particularly in Fig. 5.3(c). We also speculate that the peak in $\langle\lambda\rangle$ observed for decreasing $1/B$ at large aspect ratios may also occur at small aspect ratios, but at values of $1/B$ too small to be reached.

To summarize this chapter, we have discovered fluctuations that intermittently narrow evolving single fingers; the magnitude of these fluctuations follows a power law with the capillary number for all aspect ratios studied. We also have found a departure from the classic scaling of finger width versus $1/B$ for large aspect ratios ($w/b \gtrsim 250$); the average finger width narrows at low $1/B$, while the maximum finger width increases. These phenomena are not predicted by existing viscous fingering theories even though the phenomena are most pronounced for parameters that more closely match the theoretical assumptions.

Chapter 6

Coarsening of Fractal Viscous Fingers

In section 3.2.3, we presented a new scenario of domain coarsening discovered by Conti, Meerson, and Sasorov [31, 32] and extended by Lipshtat, Meerson, and Sasorov [75]. They found in their simulations that a fractal initial condition relaxing under a local conservation law will not show the scale invariance typical of domain coarsening systems. This has wide ranging applications as there are many physical systems which undergo relaxation from a fractal initial state. However, no experimental work has been done to test the predictions of the simulations.

To study this scenario in a simple physical system, we have examined the coarsening due to surface tension of fractal patterns generated in our radial Hele-Shaw cell. This is the first study of the relaxation of viscous fingering patterns. We have found that the relaxation of viscous fingers is also not scale invariant and possesses two length scales that have the same scaling as was found in Lipshtat *et al.*'s work on the coarsening of fractals [129].

6.1 Data Acquisition and Analysis

We generate our fractal fingering patterns using the apparatus described in section 4.2.1. We open the buffer to the vacuum reservoir while opening the needle valve to allow air at atmospheric pressure to flow into the cell. The resultant highly branched patterns have a minimum finger width more than two orders of magnitude smaller than the cell size.

The exact valve sequence for this experiment is

1. open the needle valve,
2. open the vacuum valve,
3. allow pattern to grow,
4. close vacuum valve,
5. open atmosphere valve briefly to remove pressure difference and stop pattern growth,
6. close the atmosphere and needle valves,
7. pattern begins to relax due to surface tension.

This is all controlled by a program written specifically for this experiment. You click a button once to take a background image, click that button again to start the pattern growth, and click that button a final time to stop the pattern growth and begin acquiring images of the system as it relaxes. Images are acquired for the first few seconds at the camera's full frame rate 12 frames/s. Then the rate decreases as the relaxation slows down, becoming as slow as one frame every 250 s. Since we expected one of the length scales to change as approximately $t^{1/3}$, we spaced the images out as a cubic function

of time to compensate. We acquired images for a total time of 10^5 s.

The images are processed as described in section 4.2.2. For each image (i.e., for each time t), we calculate the circularly averaged correlation function, $G(r,t) = \langle [\rho(r',t)][\rho(r'+r,t)] \rangle$, (cf. eqn. 3.1), where $\rho = 1$ in the air phase and $\rho = 0$ in the oil phase. This is normalized so that $G(r=0,t) = 1$. (Recall that the physical/intuitive meaning of this correlation function was discussed in section 3.2.2.)

This correlation function is calculated using standard numerical techniques. The image is put through a 2D fast Fourier transform (FFT), then the square of the magnitude is taken at each pixel. At this point, appropriate averaging of the resulting image would give us the structure function for the original image; however, we did not use this quantity in the final analyses. We then take the real part of the inverse 2D FFT and average this over all points equidistant (rounding down to integer lengths) from the center. Symbolically, if I is the original image this is essentially $G(r) = \langle \text{ real}[\text{ IFFT}\{ \text{ } |\text{FFT}(I)|^2 \text{ } \} \text{ }] \rangle_\theta$.

Avner Peleg [110] provided use with the same code to calculate the correlation functions that was used by Conti *et al.* [31, 32] and Lipshtat *et al.* [75]. Unfortunately, this code was written in FORTRAN with comments in Italian. I first performed a straight-forward, one-to-one translation from FORTRAN to Matlab. The result took over a half hour to calculate the correlation function for a single image! Of course, after performing such a simple translation, the resulting code was not in Matlab's proper idiom. (Programming languages, like human languages, have their own idioms and styles to be followed.) After

re-writing the code to be idiomatically correct, it processed a single image in 17 minutes and 7 seconds. This was still disastrous, as we had thousands of images to process.

There were several possible approaches to resolving this. One would be to translate the code into C++, a much more efficient compiled language. However, even using any of several high-quality numerical libraries freely available, it seemed likely that it would take a while to develop and debug such code. Instead I continued using the Matlab script and applied the code optimization strategies discussed in Steve McConnell's *Code Complete* (ch. 28 & 29) [84]. The code tuning steps that improved the run time are shown in table 6.1. The biggest improvements came from eliminating an intermediate calculation (the structure function) whose results were not being used, and from reducing the size of the zero-padded images from 2048×2048 to 1280×1280, thus ignoring the conventional wisdom about FFTs being faster for a data set whose size is a power of two. (The images were just larger than 1024×1024 and could be cropped, but then there was an unacceptable aliasing artifact at $r = 512$ pixels.)

This was the most aggressive code tuning I have ever performed. These modifications took about half a day, then the processing of all the images took about 4 days. Otherwise, it would have taken over a month. This aggressive optimization does have a cost. The first idiomatically correct version was an elegant script 20 lines long. The final version is a 150 line monstrosity that I am frightened to even look at again.

Optimization	Time	Improvement	Comment
Original Code	17:07	—	First code in Matlab idiom
Use FFTshift routines	13:45	20%	Eliminates calculations in inner loop
Use vectorized functions to eliminate a matrix copy	12:11	11%	
Precalculate radius bins	9:12	25%	Eliminates calculations in inner loop
Unroll inner loop	8:22	9%	Matlab's for-loop performance is poor
Change zero padding from 2048 to 1280	3:20	60%	Defying conventional wisdom about FFTs and powers of 2
Eliminate structure function calculation	1:54	43%	Wasn't being used in final analysis
Final Code	**1:54**	**89%**	**9× faster**

Table 6.1: Code tuning steps performed to correlation function calculation routine to provide reasonable processing times. (The improvement process is not this linear; changes that increased the run time are not shown.)

6.2 Results

The observed coarsening of a viscous fingering pattern is shown in fig. 6.1. The similarity to the DLA coarsening shown in fig. 3.6 is striking. In both cases the initial highly branched fingering pattern becomes smoother as time progress, and the cluster breaks into fragments while its radius of gyration r_g remains constant. (In the experiment r_g actually decreases slightly, 2% in 2×10^4 s.) Recall that Conti *et al.* [31] argue that a scale invariant relaxation *must* involve a significant decrease in r_g (pg. 74). The absence of such decrease in our experiments is the first indication of a breakdown of scale invariance.

Properties of the clusters are deduced from the correlation function, $G(r,t)$. At early times we find $G \sim r^{-0.29}$ over more than a decade of length scales (fig. 6.2), indicating fractal scaling with dimension $D = 1.71 \pm 0.03$ (cf. pg. 70). Using a cluster mass method, we obtain $D = 1.70 \pm 0.03$. The issue of the fractal dimension of viscous fingering patterns and its relation to DLA will be discussed further in section 7.3.

At very small scales $G(r,t)$ decays linearly (fig. 6.3) with an inverse slope proportional to the smallest length scale, $l_1(t)$, which increases with time (Porod law [17]); for lengths smaller than l_1 the interface appears smooth.

Despite the dramatic time evolution of a cluster (fig. 6.1), the correlation function reveals that the large-scale structure remains frozen (see fig. 6.2 and 6.4). The combination of an increasing lower cutoff and a frozen tail must

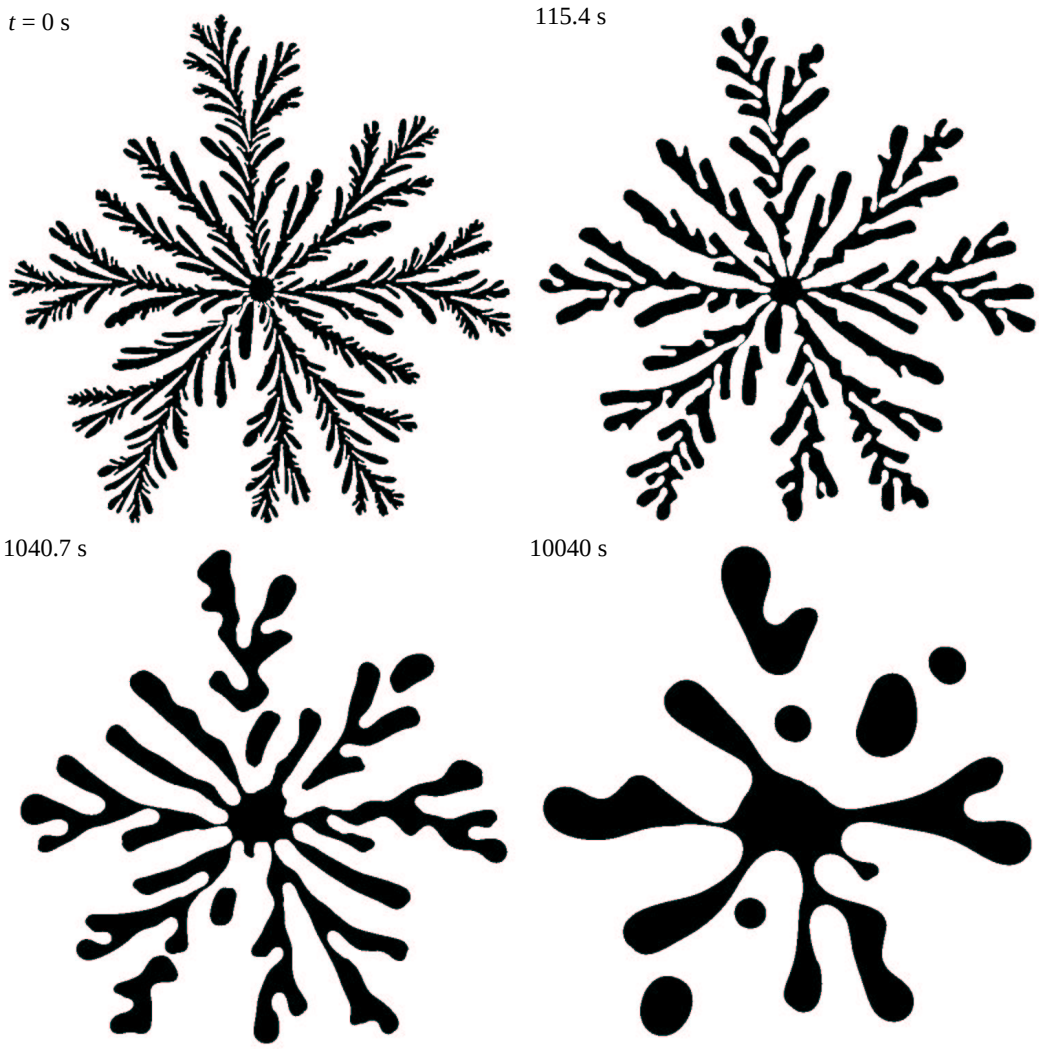

Figure 6.1: Images of a viscous fingering pattern (cluster diameter 200 mm) relaxing due to surface tension. The times were chosen to correspond with the times in fig. 3.6, the DLA coarsening images provided by Conti, Meerson, and Sasorov [33]. Their simulation uses a dimensionless time step that corresponds to 2.1 seconds in the viscous fingering relaxation. The relaxation in both systems is characterized by the smoothing of small scales, fragmentation of the cluster, and a constant radius of gyration.

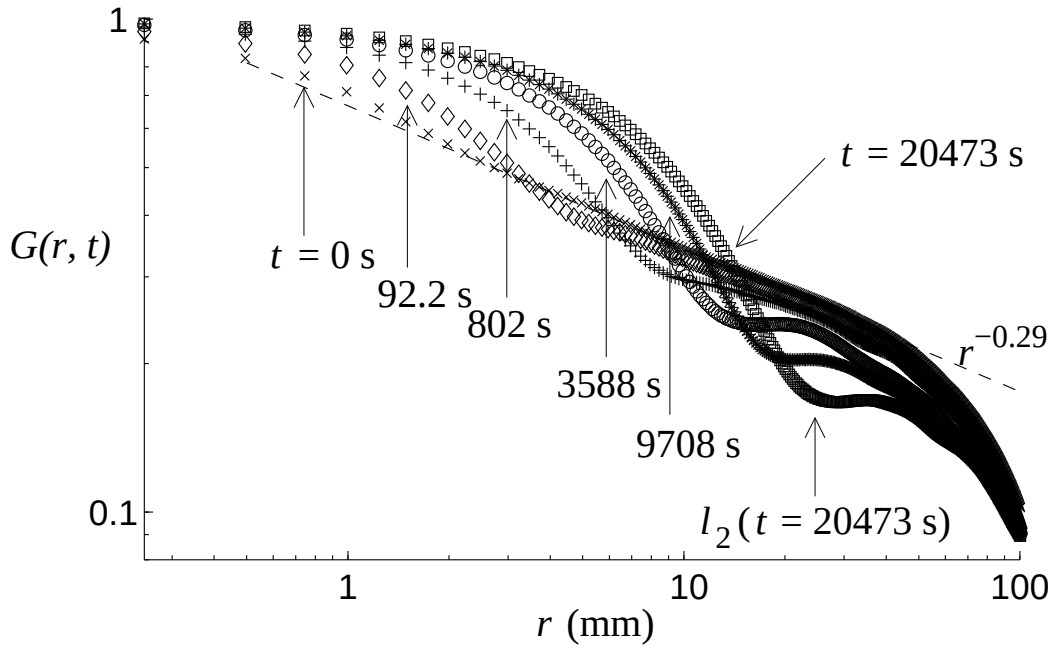

Figure 6.2: Correlation functions at different times t, averaged over 16 experimental runs. The dashed line shows a fit to the fractal scaling region for the $t = 0$ curve, where $G \propto r^{-0.29}$, yielding a fractal dimension of $D = 1.71 \pm 0.03$. The scaling regime shortens and eventually disappears as $G(r, t)$ develops a minimum.

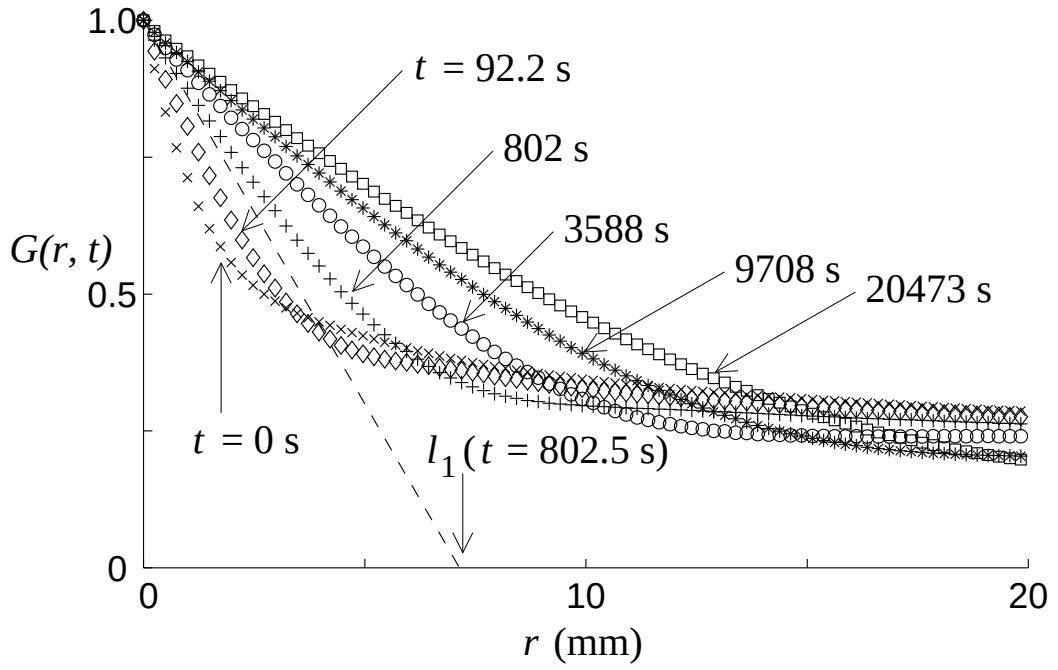

Figure 6.3: The correlation functions on a linear plot, showing a linear decay for the smallest scales. $l_1(t)$, the length scale below which the cluster is smooth (non-fractal), is obtained by measuring the inverse slope of a linear fit to $G(r,t)$ at small scales (Porod law [17]). The dashed line shows such a fit for $G(r, t = 802\text{ s})$, which yields $l_1 = 7.14$ mm.

lead to the appearance of a second length scale: Because of the conservation of volume, the integral of $rG(r,t)$ with respect to r is invariant in time. The thickening of small scales while largest scales remain frozen thus requires the dilution of intermediate scales and hence the formation of a dip in $G(r,t)$. The local minimum of $G(r,t)$, visible in plots of $G(r,t) - G(r,0)$ (fig. 6.4), corresponds to half the distance between adjacent arms of a cluster. We define l_2 to be the location of this minimum. This definition of the larger length scale differs from that of Lipshtat *et al.* [75], who obtained a length ℓ_2 by finding the smallest radius beyond which $|G(r,t) - G(r,0)|$ was smaller than a predetermined threshold. The length scale ℓ_2 was thus associated with the boundary between the dilute and the frozen parts of the correlation function. Our method for obtaining l_2 is more robust and less arbitrary than the method for determining ℓ_2, but we find that within the uncertainty the two lengths are proportional, which indicates that the inter-arm spacing determines the location of the correlation function's frozen tail.

At $t = 0$, both l_1 and l_2 are equal to the cutoff length scale l_0 of the fractal cluster, but at long times we find $l_1 \sim t^{0.22\pm0.02}$ and $l_2 \sim t^{0.31\pm0.02}$ (fig. 6.5). Nearly the same exponent values were obtained for the two length scales in Lipshtat *et al.*'s diffusion-controlled coarsening of non-DLA fractal clusters, 0.22 ± 0.01 and 0.32 ± 0.01 [75]. The different growth rates of l_1 and l_2 exclude any global re-scaling that would lead to the same form for $G(r,t)$ at all times, as can be seen in fig. 6.2.

In a scale invariant coarsening process, information about the initial

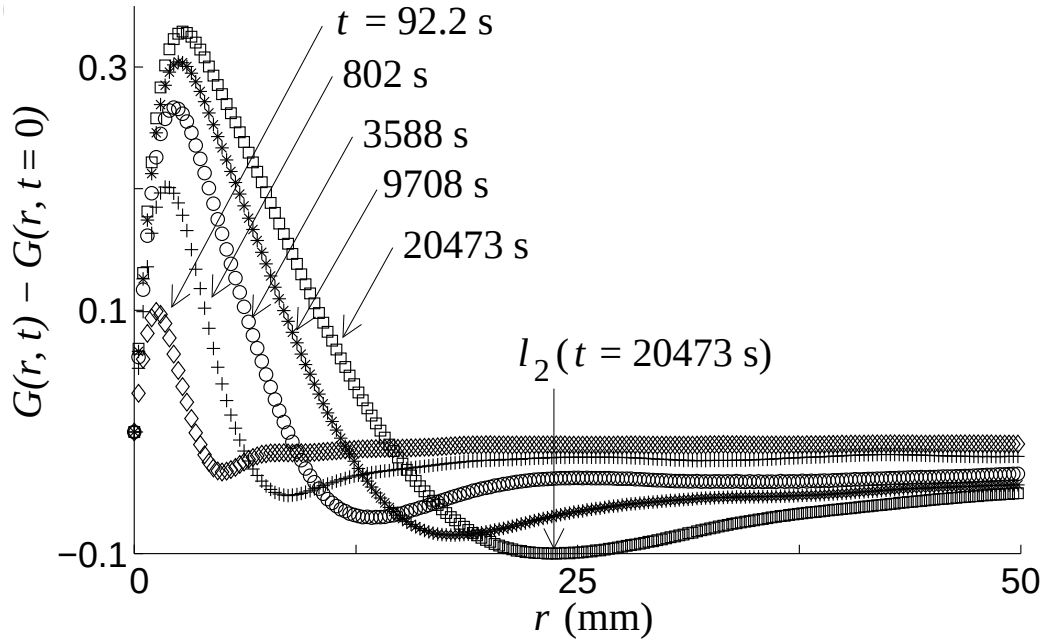

Figure 6.4: The difference $G(r,t) - G(r,0)$ has a minimum that is taken to be $l_2(t)$, which is about half the inter-arm distance.

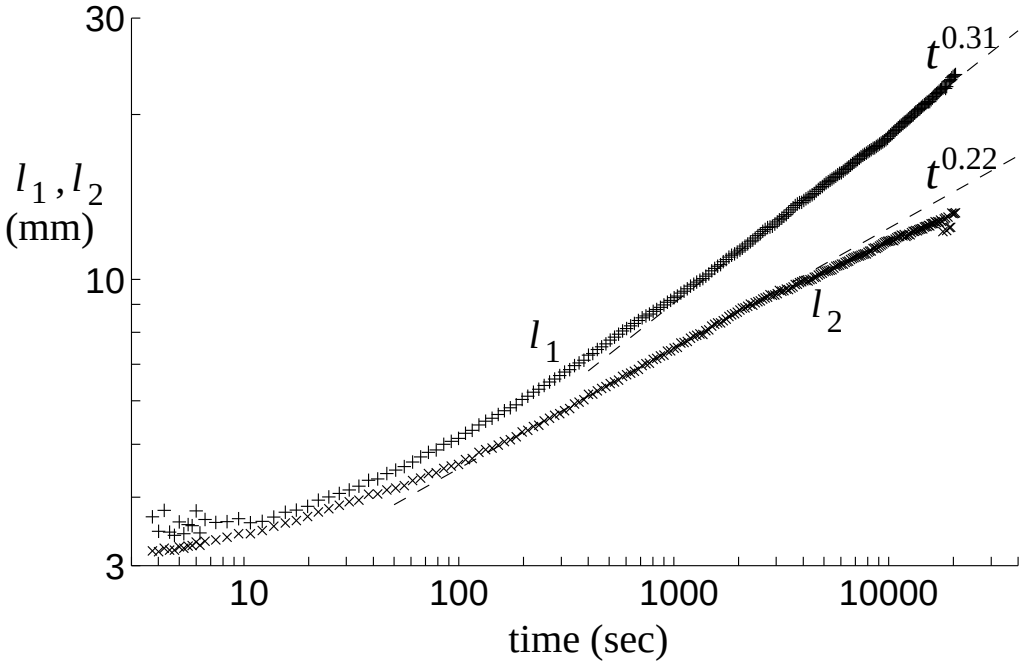

Figure 6.5: The time evolution of the two length scales with power law fits at long times (dashed lines). At late times ($t \gtrsim 4000$ s), l_1 grows more slowly as the smaller bubbles approach their equilibrium size after fragmentation.

structure is quickly lost, but this is not the case in the relaxation of viscous fingering patterns: the longer the system evolves, the larger l_2 is compared to l_1 (fig. 6.5). The initial conditions of the cluster are *not forgotten*; instead, they determine a unique combination of l_1 and l_2 at any time.

The effect of the initial conditions at late times is illustrated by the clusters in fig. 6.6. Different initial pressure differences produced clusters with different minimum length scales l_0 but did not affect the cluster fractal dimension [81]. We allowed each cluster to evolve until the lower length scale reached the same value, $l_1(t) = 14.0$ mm. Clusters that evolved from a smaller l_0 had to evolve over longer times, so l_2 became larger for those old clusters, which have greater fragmentation and arm separation than the young clusters. Thus information about the initial configuration is retained. In principle a cluster's age could be estimated from measurements of l_1 and l_2 at a late time, but a precise determination of age would require an understanding of the evolution at early times, before the onset of the power law scaling ($t \lesssim 100$ s).

To summarize this chapter, we observe the loss of scale invariance in the coarsening of fractal viscous fingering patterns. There are two length scales: a small length scale below which the cluster is smooth, and a larger length scale corresponding to half the distance between adjacent cluster arms. These two length scales are described by power laws with different exponents. The existence of the larger length scale is generated by the cluster fragmentation, which is a consequence of volume conservation together with the local smoothing in the relaxation process. The breakdown of scale invariance sug-

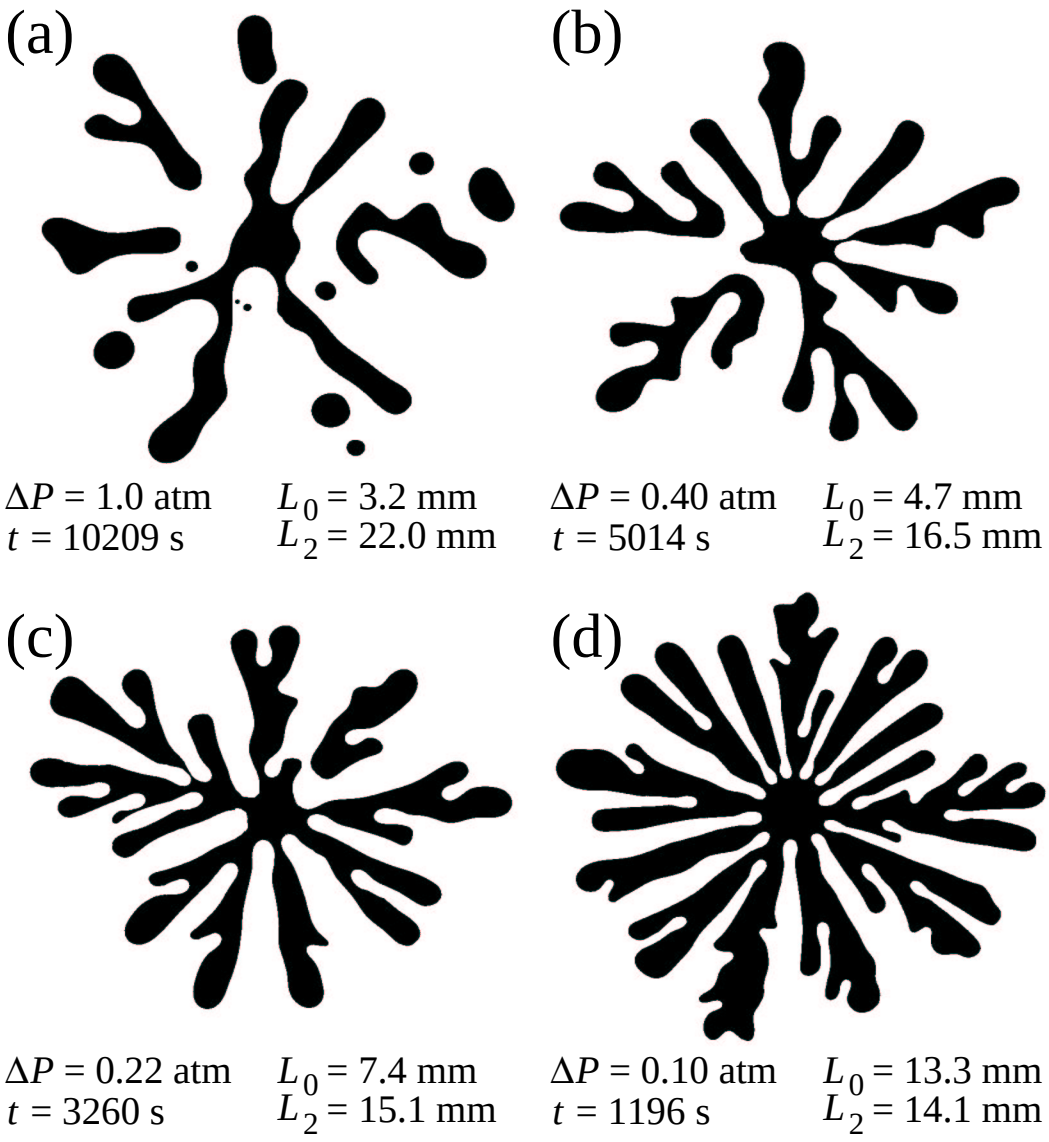

Figure 6.6: Four clusters generated with different pressure differences ΔP. The clusters have different initial length scales l_0, but the lower cut-off length has evolved in time to the same value, $l_1 = 14.0$ mm. The different evolution times lead to different lengths l_2, mirrored by enhanced fragmentation of older clusters. In contrast to scale-invariant coarsening, the initial conditions are not forgotten.

gests a scenario in which the present configuration of other fractals, such as in geological systems, might include information about their age and initial morphology.

Chapter 7

Other Viscous Fingering Phenomena

We have briefly investigated a number of other viscous fingering phenomena; this chapter discusses our findings thus far.

7.1 Pinch-off Events

In addition to the finger width fluctuations discussed in chapter 5, we have observed another unexpected phenomenon in our cells: finger pinch-off events followed by reconnection to a different finger [99]. An example of such an event is shown in fig. 7.1.

For sufficiently high flow rates, several fingers compete during the early stages of growth until one gets ahead, suppressing the growth of the other initial fingers. However, if the initial competition stage was long, the suppressed fingers will continue to interact with the active finger. As the active finger continues to grow, it narrows at the back, and the adjacent short finger grows towards it. This process is very slow at first and gradually accelerates; the final pinch-off and the connection of the previously suppressed finger to the resulting bubble occurs very quickly.

The dynamics of the finger tip appear unaffected during these events,

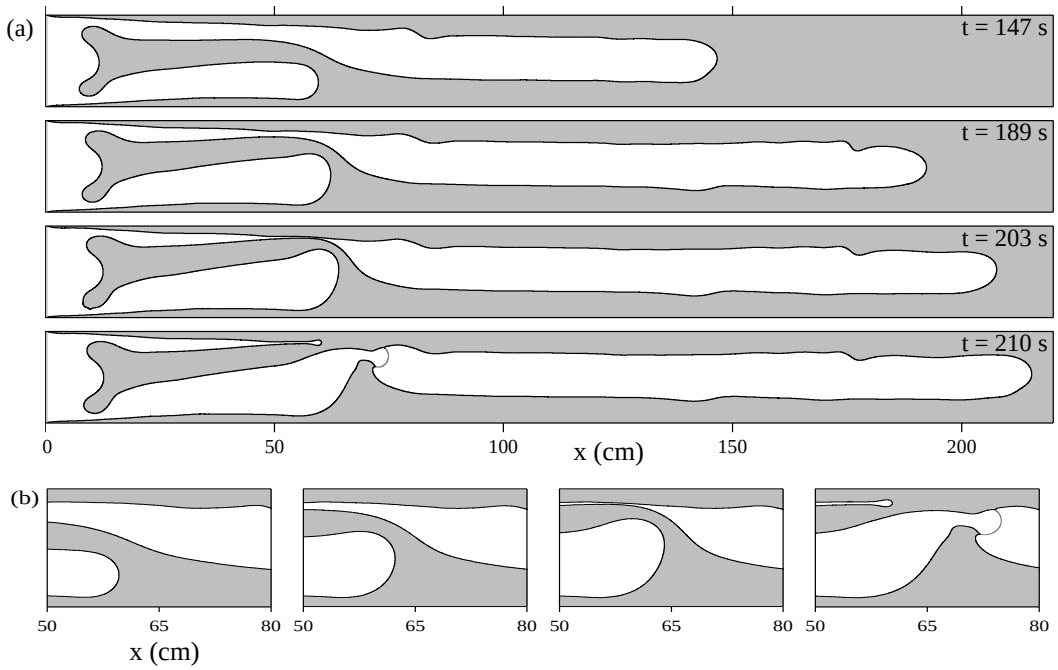

Figure 7.1: (a) A time sequence from a run where a pinch-off event occurred; the times since the beginning of the pumping are shown. The back of the growing finger narrows while the adjacent suppressed finger grows. The process accelerates as it continues; the pinch-off and subsequent reconnection happens in less than two seconds (which is faster than the time resolution we had for these data). The grey line in the last interface shows where the interface between the middle finger and the disconnected bubble finally broke; this point could be clearly seen on the image as a thick film left behind at that point. (b) A close up view of the pinch-off at the same times.

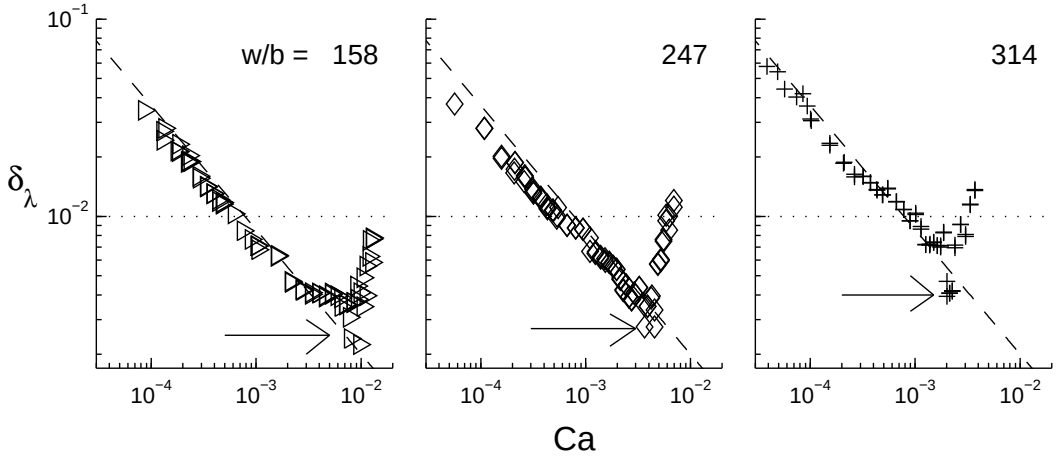

Figure 7.2: The data for some of the aspect ratios in fig. 5.4 are repeated here to demonstrate the slight suppression of secondary instabilities when a pinch-off event occurs. The upturns in δ_λ signal the onset of the secondary instabilities in the tips of the fingers. The arrows point to data from runs where pinch-off events occurred; though other runs at these flow rates are part of the upturn, these runs continue following the power law to lower δ_λ.

though the onset of secondary instabilities is apparently slightly suppressed. This can be seen in fig. 7.2; all of the data points indicated by arrows had pinch-off events, and they continue to follow the fluctuation power-law when other runs at similar flow rates without pinch-off events depart that curve, beginning the upturn that marks the onset of the secondary instabilities. At higher flow rates, pinch-offs at the back of fingers and tip instabilities both occur, apparently independently of one another.

Pinch-offs may or may not occur on a particular run at a given flow rate, since this depends on the configuration of the initial finger competition, which can be different each time. In particular, the levelling of the cells is

crucial: a small tilt around the long axis will give fingers on the higher side of the cell an early advantage; the shorter dormant fingers resulting from this do not interact as quickly.

Pinch-off events are not mentioned in any of the previous literature; we believe that we observe them because our cell has an unusually high ratio of length to width, allowing sufficient time for evolution towards the pinch-off to occur before the finger reaches the end of the channel. Also, seemingly unimportant asymmetries across the width of the cell, like the levelling mentioned above, can disrupt the long period of finger competition and thus suppress the pinch-off events. We have observed the pinch-off phenomenon in different cells at both high and low aspect ratios. These events can occur at flow rates where the plate bending due to the imposed pressure gradient is unmeasurably small. Pinch-off events can also be seen in the radial cell (fig. 7.5). The cause of this phenomenon is still unknown.

We did not study this phenomenon further for several reasons. After completing our work on fluctuating fingers, we wished to work on something more conventional instead of examining yet another unexpected phenomenon. Also, the original optical system was not well suited for studying pinch-off events. The final stages of these events occur within a few seconds, faster than that system could scan the channel and save the frames to disk. The new optical system, which is intended to scan the channel faster and save the frames in memory, might perform better for studying pinch-off events.

To summarize, we observe finger pinch-off and reconnection events at

the back of the linear cell. These are apparently due to an interaction between adjacent fingers that has not yet been explored. Like the fluctuations, the pinch-off phenomena have not been predicted by existing viscous fingering theories, nor have they been observed in simulations or other experiments.

7.2 Testing the Singular Perturbation of Surface Tension

In section 2.4.2, we discussed the debate over the role of surface tension in the analysis of the viscous fingering problem. What can experimentalists hope to contribute to such an apparently pedantic mathematical debate? We cannot after all turn surface tension off. However, as we discussed in section 2.5.1, there seems to be a way to turn off the selection effect due to surface tension. Recall that by perturbing the finger tip with a bubble, wire, or groove, fingers with the shape of the zero-surface tension solutions of Saffman and Taylor (eqn. 2.28) for $\lambda < 1/2$ can be created. What would happen if the tip perturbation were then removed? The zero surface tension solution is unstable and the finger should evolve towards $\lambda = 1/2$. If the singular perturbation view of surface tension is correct, the interface should evolve quickly, in $O(1)$ time. If not, the interface, since it has the shape of a zero surface tension solution to start, should only evolve in a time $O(1/\sigma)$, which can be quite long for low values of the (non-dimensional) surface tension.

In fact, we have qualitatively observed the situation where anomalous fingers with bubbles at their tips evolve back to the half-width finger when the

bubble breaks. In these cases, the evolution is quite fast; it reaches $\lambda \approx 1/2$ before it travels another channel width. However, the bubble represents a significant perturbation of the interface shape when it bursts, and when (or if) the bubble bursts cannot be externally controlled. However, if a wire or groove were extended halfway down the length of the channel, one would get the zero surface tension shapes and then watch them evolve when they travelled beyond the end of the wire or groove. This concept, illustrated in fig. 7.3, was the basis of an experiment we attempted.

The experiment proved more difficult to perform than originally expected and was eventually abandoned, though there is still no *a priori* reason it could not be done with appropriate resources.

We initially tried to perturb the finger tip with a wire extending partway in the channel. However, in the experiments of Zocchi *et al.* [149], they used a thin wire suspended under tension at the cell's mid-height. Obviously, this cannot be done for a wire that doesn't span the length of the channel. We let our wire sit on the bottom plate instead. For thin wires (similar to Zocchi *et al.*'s size), the finger was perturbed little; the wire didn't always extend beyond the thickness of the wetting layer even. For thicker wires, the finger split in two around the wire; apparently these wires filled too much of the gap and behaved more like side walls.

That left only grooves to try. In some preliminary work in small test cells, fingers did follow the grooves nicely, but uniformity of the groove was important. We didn't think this could be achieved by hand and found a

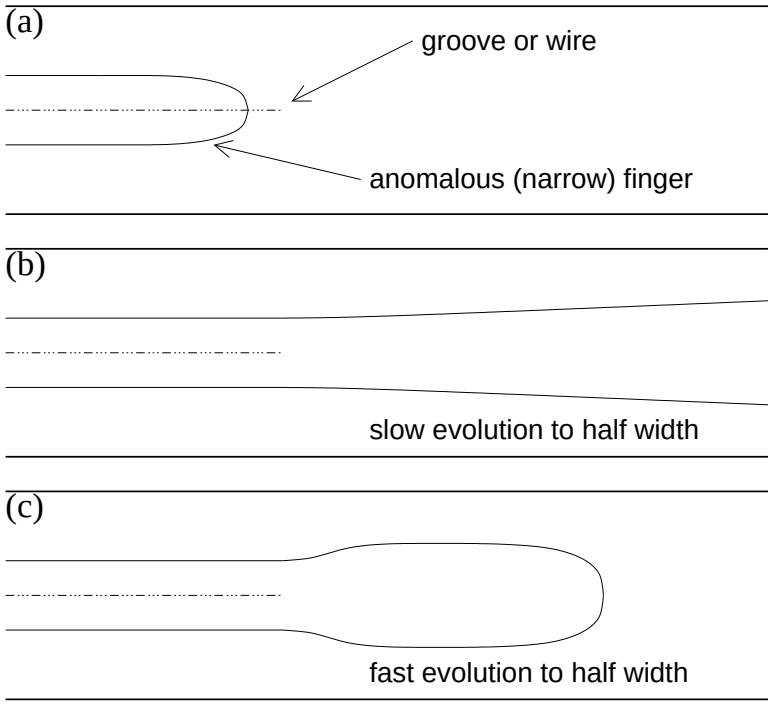

Figure 7.3: (a) An anomalous (narrow) finger is created along a wire or groove. It has $\lambda < 1/2$ and takes the shape of the zero surface tension solution of Saffman and Taylor (eqn. 2.28); the selection effect due to surface tension has been turned off. (b) The finger travels beyond the end of the wire/groove and evolves slowly back to $\lambda = 1/2$ on a time scale of $O(1/\sigma)$. The effect of surface tension cannot be singular if this occurs. (c) The finger travels beyond the end of the wire/groove and evolves quickly back to $\lambda = 1/2$, on a time scale of $O(1)$. The effect of surface tension is apparently singular in this case.

company called AquaJet who said they could create a uniform groove with a regular end in the glass. However, after several months, they announced that they had broken every test piece they had tried, even after obtaining new tools, and that they would not risk attempting the procedure on the large glass plate we had provided them. At this point, work on the radial cell had begun in earnest, so we never searched for a new company to etch the uniform groove.

7.3 Viscous Fingering Fractal Dimension and DLA

In section 3.1 and chapter 6, we briefly discussed the connection between diffusion limited aggregation and viscous fingering (aka Laplacian growth). Many theorists are currently discussing the exact relationship, especially whether Laplacian growth is the continuum limit of DLA: are DLA and Laplacian growth truly in the same "universality class" [39, 7, 5, 72]?

The simplest place to start investigating this experimentally is by studying the fractal dimension of highly branched radial viscous fingering patterns and comparing them with DLA clusters. Surprisingly little work has been done in this area; only Couder [34] has significant work on this, as we discussed in sec. 2.6.2.

Using a cluster mass method on 16 initial patterns from the relaxation experiment, we obtain $D = 1.70 \pm 0.03$, where the uncertainty is mainly due to statistical spread among the values for different images. (Each fit is statistically accurate to ± 0.01.) As we said on pg. 149, we obtain a fractal dimension

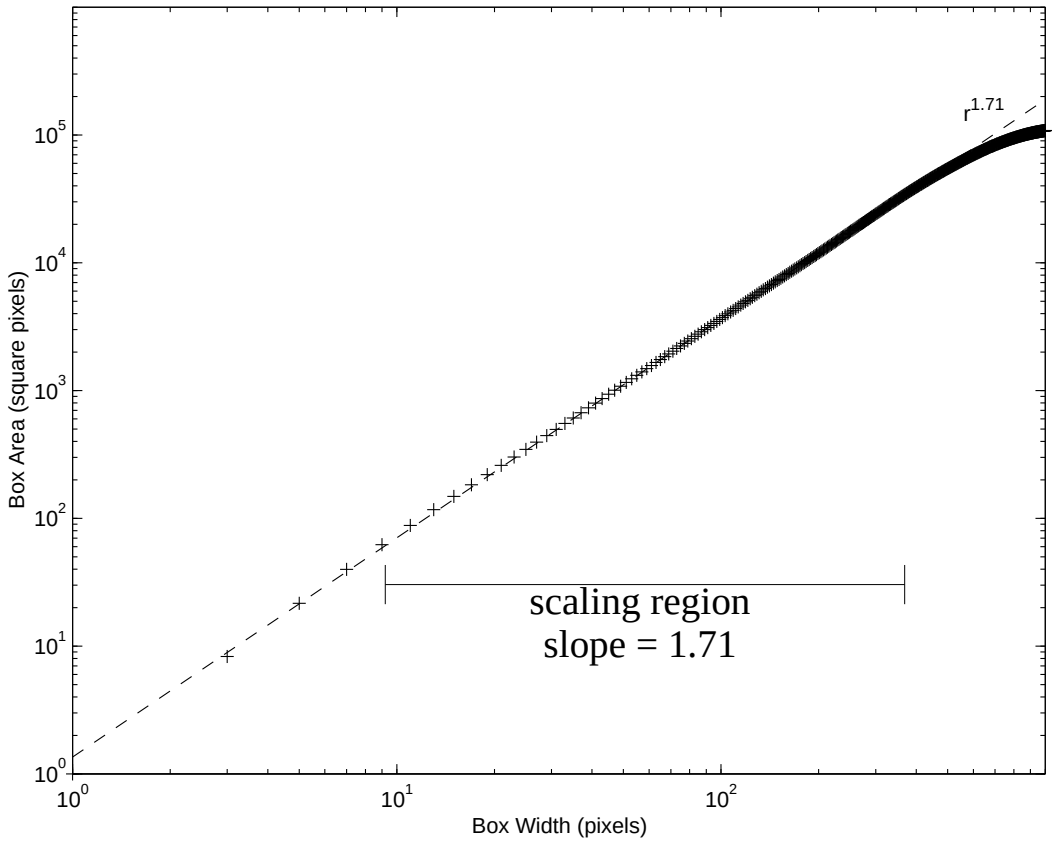

Figure 7.4: The cluster area contained inside a box of a given width plotted against that width, averaged over 25,000 points in the cluster. The slope of the scaling region gives the cluster mass fractal dimension (which should be equivalent to the box counting dimension [48]).

$D = 1.71 \pm 0.03$ from the slope of the correlation function[1], where this function is the average of the correlation functions from each pattern. This uncertainty comes from the fitting. We did examine the dimension obtained from individual correlation functions, and though the fits are not good, they do vary between individual images in the same way the cluster mass dimension does.

One thing we have noticed is a small systematic difference between patterns whose fractal dimension was below the mean and those whose fractal dimension was above the mean. Some of the radial fingering patterns exhibited pinch-off and reconnection events (see fig. 7.5). The dimensions obtained for these patterns are systematically smaller than for patterns that did not experience pinch-offs. The difference is not large enough to make the distribution of values obtained bi-modal, but it likely broadens the distribution quite a bit.

We tested the cluster mass algorithm by using it on objects whose fractal dimension is known analytically (e.g., a 2D Cantor set). We found that it systematically under-reports the dimension by about 1.5%. This is a typical problem for such calculations on finite size clusters [65]. Given that, my best estimate for the fractal dimension (D_0) of viscous fingering patterns is $D = 1.70 \pm 0.03$ (statistical) $\pm$ 0.03 (systematic).

This work will be continued by Dr. Olivier Praud. His preliminary analyses indicate that the radial patterns are monofractal with a dimension $D = 1.69 \pm 0.01$ [117]. However, he has not yet applied to this figure an esti-

[1]This dimension is actually the correlation dimension D_2, not D_0. The correspondence of these values is consistent with viscous fingering patterns being monofractal (all D_q's equal).

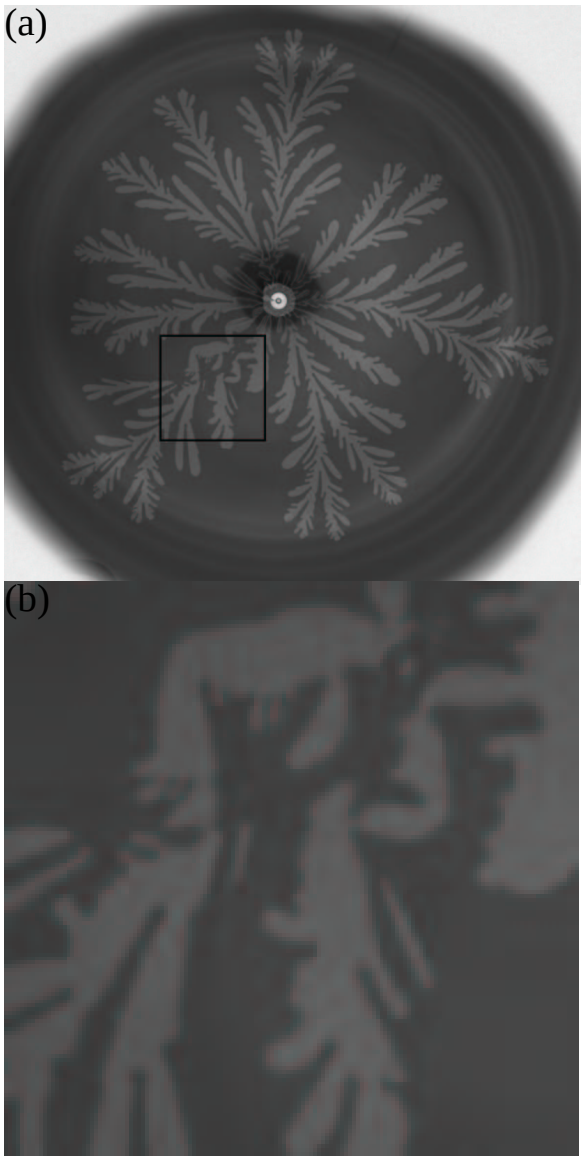

Figure 7.5: (a) A raw image from the radial cell showing the aftermath of a series of pinch-off and reconnection events (inside box). The results of computing the fractal dimension of these patterns give a small but systematic shift to lower values. (b) Close-up view of pinch-off region.

mate of the systematic uncertainty due to the under-valuing problem discussed above.

All of these findings are consistent with radial viscous fingering having the same fractal dimension as DLA. The current understanding is that DLA is a monofractal [6], i.e., D_q has the same value for all q, and that the fractal dimension of DLA [39] is $D = 1.713 \pm 0.003$[2]. While this is definitely not sufficient to show that DLA and viscous fingering are in the same universality class, it clearly does not rule that out.

And it argues strongly against their being different, as argued by Barra *et al.* [7], since a key part of their argument is the difference in fractal dimensions that they calculate. (However, again recall that they have partially withdrawn their claims [72] — probably because of what they saw in our experiment when they visited us!).

[2]Later work by the same group [72] gives $D = 1.713 \pm 0.03$ — a larger uncertainty by a factor of 10!

Chapter 8

Open Questions and Conclusions

8.1 Open Questions

There are still many unanswered questions about viscous fingering in both the linear and radial geometries. We address a few of these here before concluding. Our list is by no means exhaustive.

Many open questions have been raised by the discoveries discussed in previous chapters. The broadest are the most fundamental: what are the causes of the new phenomena we observe, the fluctuations and the pinch-off events? And each in turn raises a host of accompanying queries.

Is there a length scale associated with the fluctuations? Do they exhibit any periodicity or have an interesting distribution? What is the third control parameter that seems necessary to fully describe them?

For the pinch-off events, over what range of parameters can they be seen? Why are they so sensitive to the symmetry of the cell? What forces drive the motion? This can be further developed as part of a general question regarding the interactions between fingers, including the competition between them. (Casademunt and Magdaleno have done some interesting theoretical work related to this issue, pointing out how analytic solutions with multiple

fingers, while unstable, may change the topology of the solution space and affect the competition dynamics [21, 78].)

What is the role of surface tension? As we discussed in section 2.4.2, Mineev [92] has a set of well behaved analytic solutions to the zero surface tension problem which he claims can faithfully reproduce the dynamics of the system. We have been collaborating with him to match our experimental data to his solutions. (This was in fact one of our original motivations for beginning this experiment.) Preliminary results seem to suggest that they can in fact describe the evolution, but there have been a number of technical difficulties (primarily numerical) in bridging the gap between the analytic solutions and the experimental data. Work on this is ongoing.

Another collaborative effort with Mineev concerns his (unpublished) work on the time evolution of a series of moments of the fingering patterns [89]. For the radial geometry he defines a series of moments as

$$M_n = \int_D z^{-n} \, (\mathrm{d}x \, \mathrm{d}y), \tag{8.1}$$

Where D is the area occupied by the oil (i.e., outside the interface). This can be calculated equivalently as

$$M_n = \frac{i}{2} \oint_{\partial D} z^{-n} \, \bar{z} \, \mathrm{d}z. \tag{8.2}$$

(There are equivalent definitions for the linear geometry.) Then the time evolution of these moments is given by

$$\dot{M}_n = i\sigma \oint_{\partial D} z^{-n} \, \partial_s \kappa \, \mathrm{d}s = \sigma \, n(n+1) \oint_{\partial D} z^{-n-2} \, \mathrm{e}^{i\theta} \, \mathrm{d}z. \tag{8.3}$$

In the absence of surface tension, the moments are constant.

We could test these predictions with an experiment in the radial cell. We start with a circular interface initially, then quickly perturb the interface by extracting a small amount of oil. The perturbed interface will then begin relaxing back to a slightly larger circle. We can then compare the time evolution of the moments versus the expected evolution given by eqn. 8.3. While this experiment is simple conceptually, it has proven more difficult to perform than anticipated. (I had hoped to include the results of this as part of this dissertation.) The film-wetting creates a number of non-trivial effects, and setting up an initially circular interface is actually somewhat difficult — perhaps unsurprisingly, since the system was designed to maximize the interfacial instability to create a fractal pattern! Work on this project will be continued by Matthew Thrasher, a new graduate student.

Another open question concerns the statistics of the tip splitting instability (fig. 8.1). One can examine the distribution of fjord widths, fjord direction (angle with respect to the channel axis), and the fjord lengths (the last has been studied some by Lajeunesse and Couder [67]). We can then ask what regularities (if any) underlie these distributions and how they vary with parameters such as $1/B$. This may give us insight into the underlying mechanisms of the instability. Our linear cell's capacity to easily take large data sets will be invaluable in collecting these statistics.

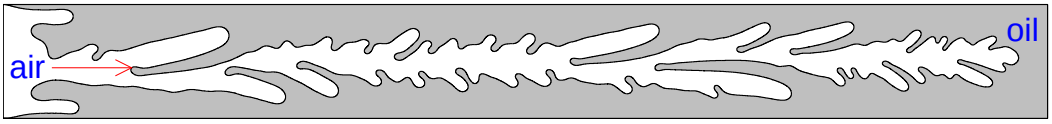

Figure 8.1: A viscous fingering pattern from our experiment showing a repeated sequence of tip splitting. The resulting fjords have a variety of widths, angles, and lengths; studying the statistical distributions of these may give insight into the instability and the role of surface tension in the system.

8.2 Conclusion

We have studied a number of interesting phenomena that occur in viscous fingering in Hele-Shaw cells. In the linear cell, we have discovered several phenomena that were not observed in previous experiments. At low flow rates, growing fingers undergo width fluctuations that intermittently narrow the finger as they evolve. The magnitude of these fluctuations is proportional to $\mathrm{Ca}^{-0.64}$, where Ca is the capillary number, which is proportional to the finger velocity. This relation holds for all aspect ratios studied up to the onset of tip instabilities. At higher flow rates, finger pinch-off and reconnection events are observed. These events appear to be caused by an interaction between the actively growing finger and suppressed fingers at the back of the channel. Both the fluctuation and pinch-off phenomena are robust but not explained by current theory.

Our experiments in a radial Hele-Shaw cell have measured the coarsening due to surface tension of fractal viscous fingering patterns. These patterns initially exhibit fractal scaling over two decades with fractal dimension

1.70 ± 0.03. The patterns at late times depend on the structural form at the onset of coarsening, providing information on the age of the fractal. Unlike most coarsening processes, this relaxation is not dynamically scale invariant; it exhibits two distinct dynamic length scales that grow as different powers of time: $l_1(t) \sim t^{0.22}$, $l_2(t) \sim t^{0.31}$. The measured exponents are in agreement with the results of recent numerical studies of diffusion-controlled coarsening of fractal clusters [75].

While these results are interesting and extend knowledge of the field, the design and construction of the two robust experimental systems described here are also major achievements. With these systems, many other interesting viscous fingering phenomena can be investigated.

Appendices

Appendix A

Design Drawings

The use of color was necessary to the drawings but may not come through on grey-scale hard copies of this dissertation; check the electronic version for full color.

The designs were all originally approximately a full page and have been reduced to fit the mandated dissertation margins.

Some of these designs were later modified, either during machining or afterwards.

Designs are only available for those pieces machined in the main shop. Pieces machined by me in the student shop, such as the original clamps, did not have such elaborate plans drawn.

Mickey Moore
471−5425
mgmoore@chaos.ph.utexas.edu
Advisor: H. Swinney

Raw Material Provided (8 Aluminum bars, approx. 4" x 2" x 27") for 8 identical pieces.

Notes:

1. The primary critical dimension is the height (3.75"). The value itself is not critical, but they must all be the same to within +− 1 thousandth. Also critical is the location of the holes marked A, which must be 1.5" from one edge to within a few (~2−3) thousandths.
2. The holes marked A are counter−bored 3" deep and drilled the rest of the way for a 1/4−20 through hole.
3. The holes marked B are tapped at least 1" deep for 1/4−20 bolts.

End On View

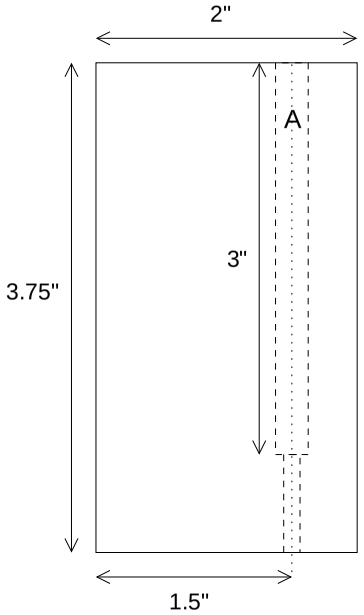

Top View

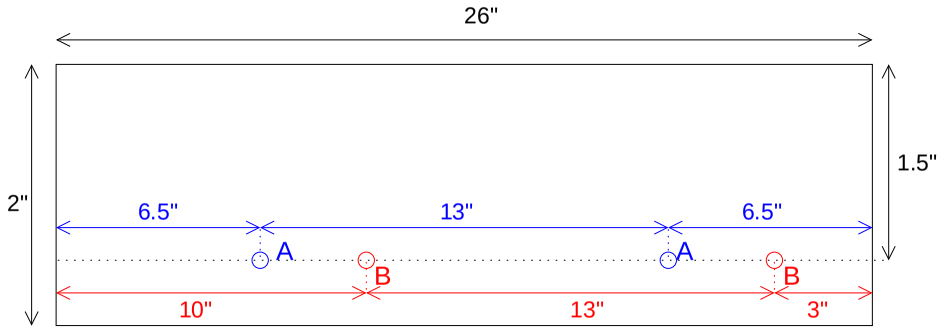

Mickey Moore
471−5425
mgmoore@chaos.ph.utexas.edu
Advisor: H. Swinney

Raw Material Provided (8 Aluminum bars, approx. 4" x 2" x 26.5") for 8 identical pieces.

Notes:

1. The primary critical dimension is the height, 3.735" +− 1 thousandth.

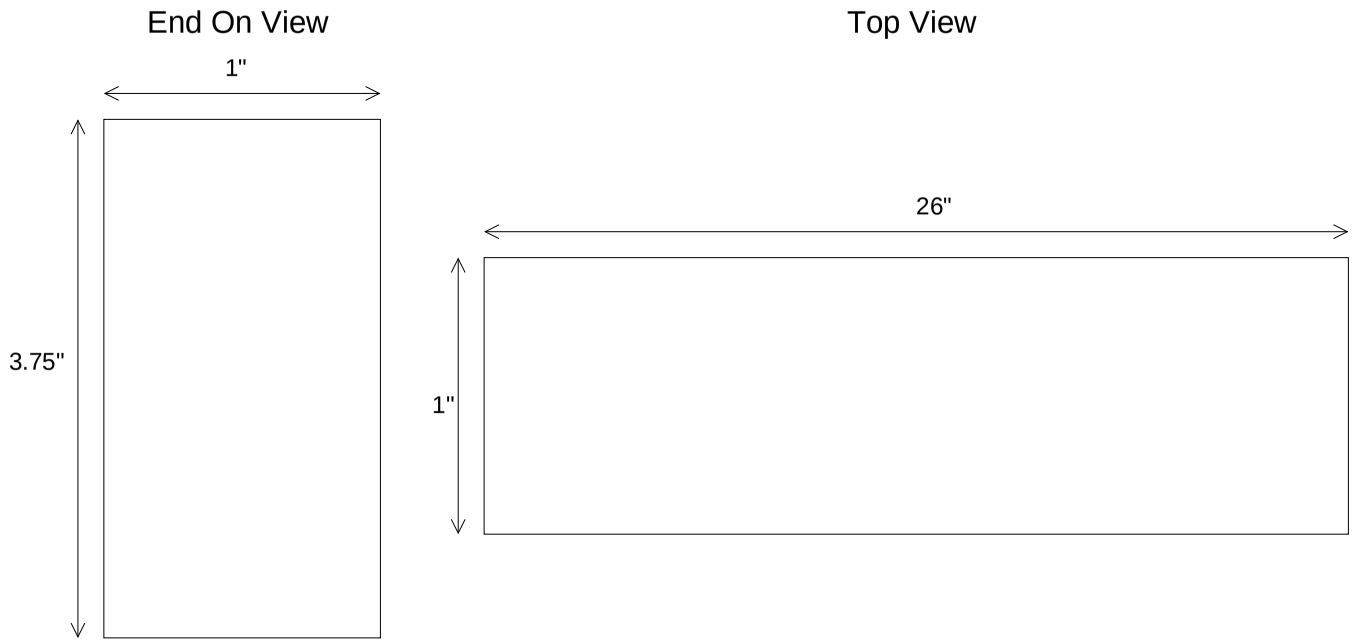

Designed: 13 August 2001

Mickey Moore (Advisor: H. Swinney)
471−5425, mgmoore@chaos.ph.utexas.edu

Pre−existing Pieces (8 identical)

The holes marked in blue are pre−existing. Those marked in red are new.
The holes marked A remain unaffected.
The holes marked B are (re−)tapped at least 1" deep for 3/8−16 bolts.
The holes marked C are tapped at least 1/2" deep for 1/4−20 bolts on long side closest to top holes.

Top View

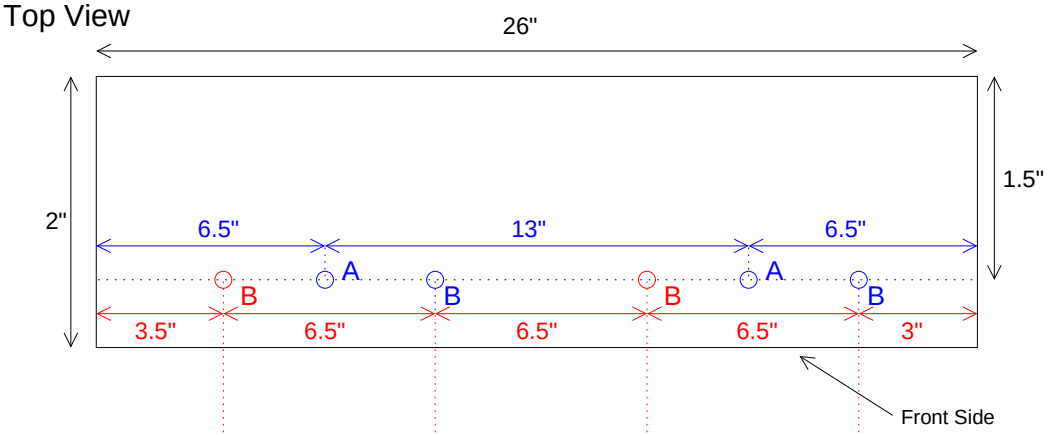

Front Side View

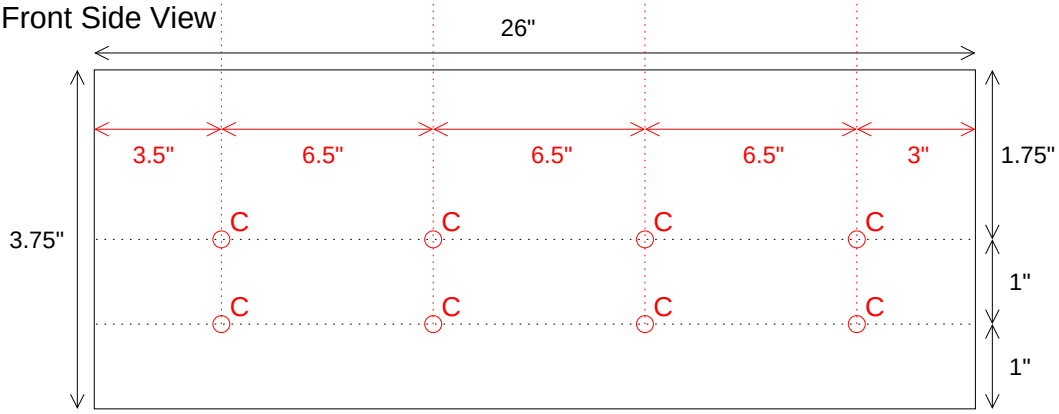

Designed: 07 July 2000
Submitted: 07 August 2000

Mickey Moore (Advisor: H. Swinney)
471−5425, mgmoore@chaos.ph.utexas.edu

Raw material provided (1018 cold−rolled steel bar stock, 1" x 1/2")
64 total pieces; 32 of each of the following:

Clamp Supports:

Holes marked A are free fit clearance holes for 1/4−20 bolts.

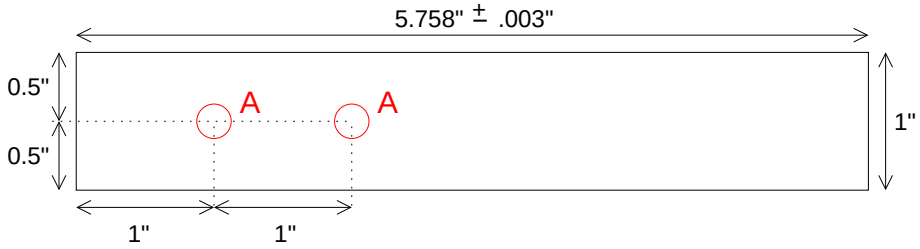

Clamps:

Slot marked B is 25/64" wide (for close fit clearance of 3/8−16 bolts) and 2.375" long (tip to tip) to allow 3/8−16 bolts at least 2" of travel.

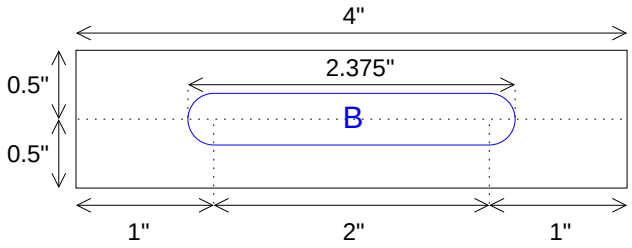

Mickey Moore
471−5425
mgmoore@chaos.ph.utexas.edu
Advisor: H. Swinney

Piece Name: Oil Buffer, ver 1.1 (for Viscous Fingering Experiment)

Material: 2 pieces of 3/4" thick plexiglass, 3" wide and 12" long

---

Piece #1:

Instructions: 1) Mill out green area (11" X 2.5" X 0.5")
2) No dimensions critical unless noted.
3) Corners shown as rounded: round to about 1/4" radius (not critical)
4) Now done with piece #1 until page 4.

View from Above

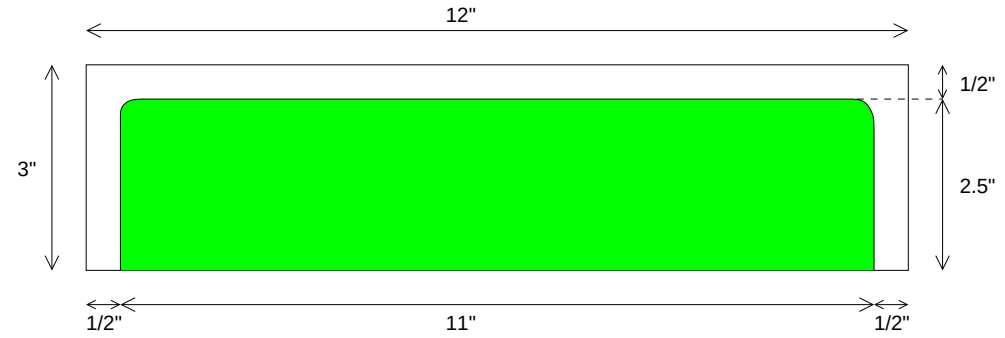

View from (long) side

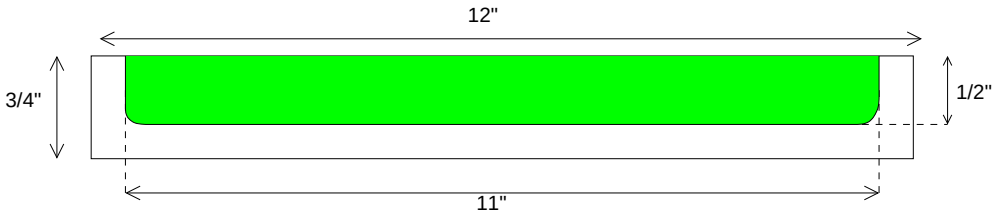

Mickey Moore
471−5425
mgmoore@chaos.ph.utexas.edu
Advisor: H. Swinney

Piece Name: Oil Buffer, ver 1.1 (for Viscous Fingering Experiment)

Material: 2 pieces of 3/4" thick plexiglass, 3" wide and 12" long

---

Piece #2:

Instructions: 1) Mill out blue area (11" X 2.5" X 0.375").
2) No dimensions critical unless noted.
3) Corners shown as rounded: round to about 1/4" radius (not critical)

Further Instructions for piece #2 follow!

View from Above

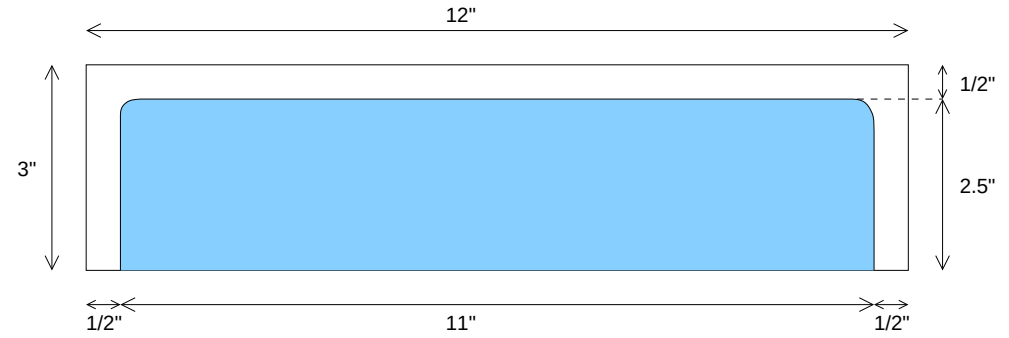

View from (long) side

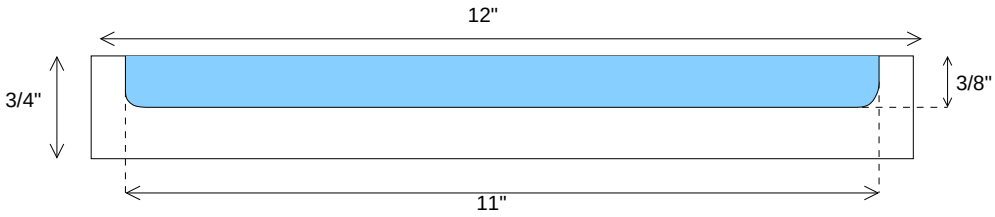

Mickey Moore
471−5425
mgmoore@chaos.ph.utexas.edu
Advisor: H. Swinney

Piece Name: Oil Buffer, ver 1.1 (for Viscous Fingering Experiment)

Material: 2 pieces of 3/4" thick plexiglass, 3" wide and 12" long

---

Piece #2 −− Continued:

Instructions: 1) Blue & red areas previously milled.
2) No dimensions critical unless noted.
3) Corners shown as rounded: round to about 1/4" radius (not critical)
4) The tricky part: the milled surface of the blue area must now be sloped uniformly from all edges (both long and short) down to center hole. Surface will need smoothing as well. What you did with previous jobs was wonderful; Just do that again!
5) Hole labelled A is centered in blue milled area and is tapped for 1/8" NPT.

View from Above

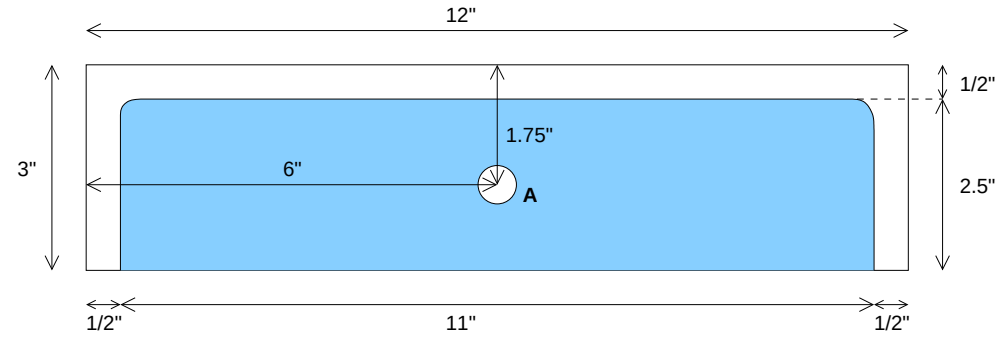

View from (long) side

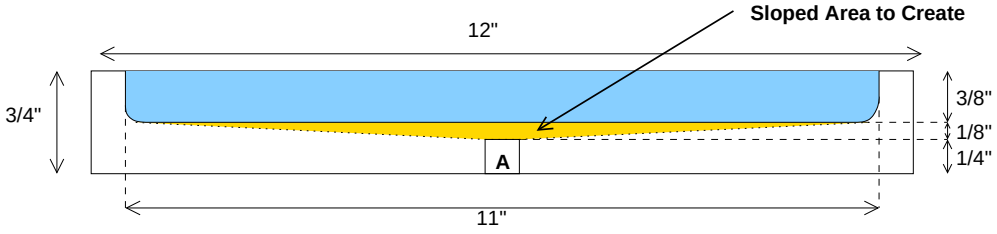

Mickey Moore
471−5425
mgmoore@chaos.ph.utexas.edu
Advisor: H. Swinney

Piece Name: Oil Buffer (for Viscous Fingering Experiment)

Material: 2 pieces of 3/4" thick plexiglass, 3" wide and 12" long

---

Joining Pieces #1 & #2:

Instructions: 1) Shaded areas previously milled
2) Epoxy plexiglass pieces together as shown. **Epoxy must be uniform over all of seam, which must be air−tight.**
3) After epoxy is fully hardened, drill and tap hole B as shown, centered on long side along seam, tapped for 1/8" NPT.

View from Long Side

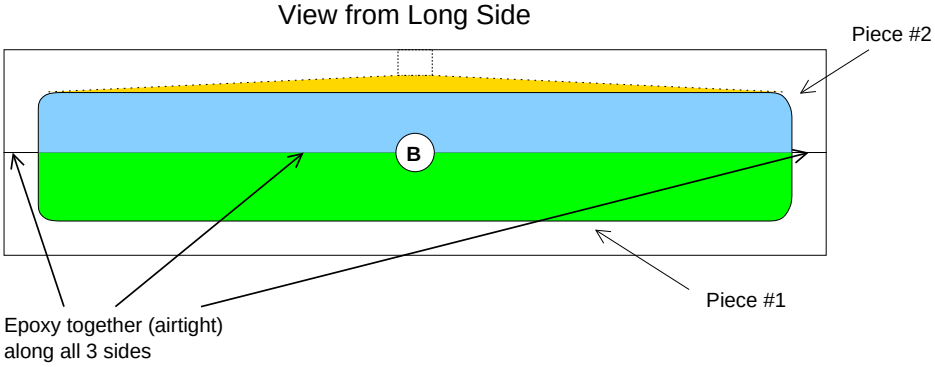

View from Short Side

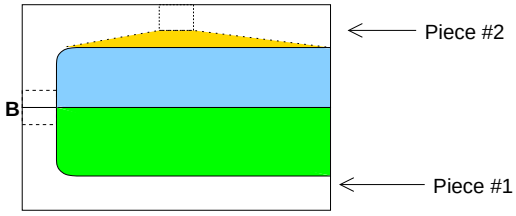

Mickey Moore
471−5425
mgmoore@chaos.ph.utexas.edu
Advisor: H. Swinney

Shaft Coupler

Brass Rod: 0.550" diameter, 1" long

Notes:

1. 0.250" hole drilled/bored along centerline of piece, with tolerances shown.
2. Slot shown on end view is ~0.025" wide, is cut along length of piece, through one side and ~0.050" deep into the other side.
3. Holes marked A are tapped for 2−56 screws on one side of the slot, with 2−56 close fit clearance on the other side of the slot. Clearance side needs an indentation for screw head, and holes should be in opposite directions.

Side View

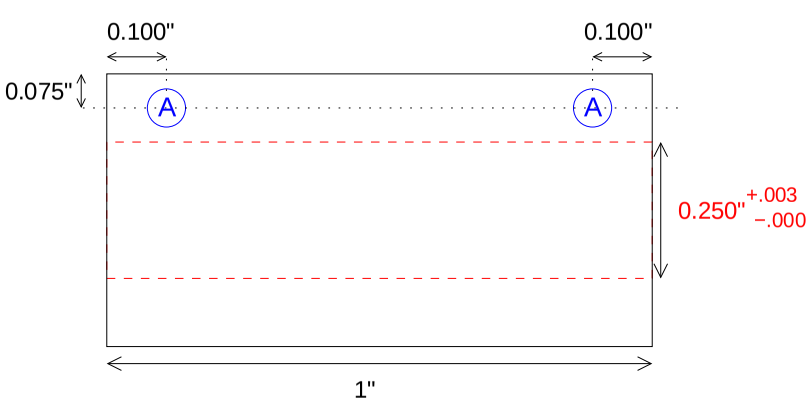

End View

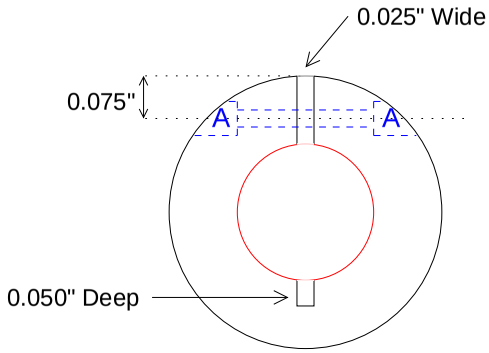

Mickey Moore
471−5425
mgmoore@chaos.ph.utexas.edu
Advisor: H. Swinney

Aluminum Rod: 1" diameter

Notes:

1. Part is cylindrically symmetric except for Surface A (which is flat).
2. Critical dimensions marked with (approximate) tolerances.

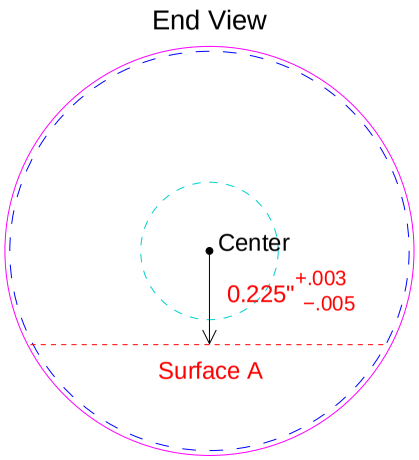

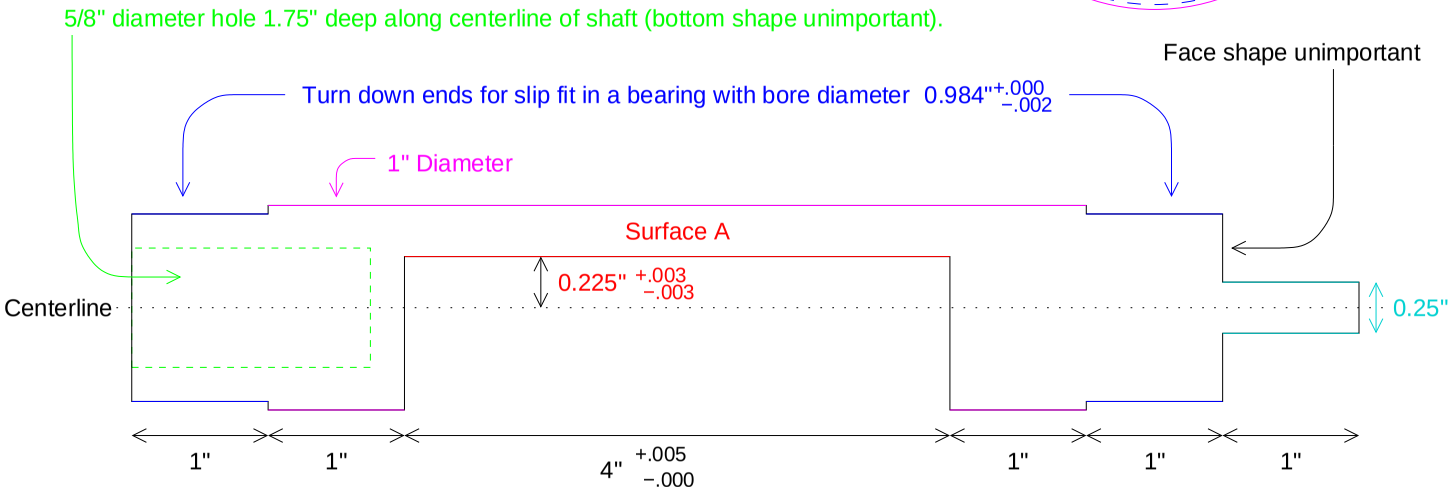

Mickey Moore
471−5425
mgmoore@chaos.ph.utexas.edu
Advisor: H. Swinney

Ring Buffer and Clamp: Cross Sections

Ring Buffer Material: Aluminum
Clamp Material: Clear Acrylic

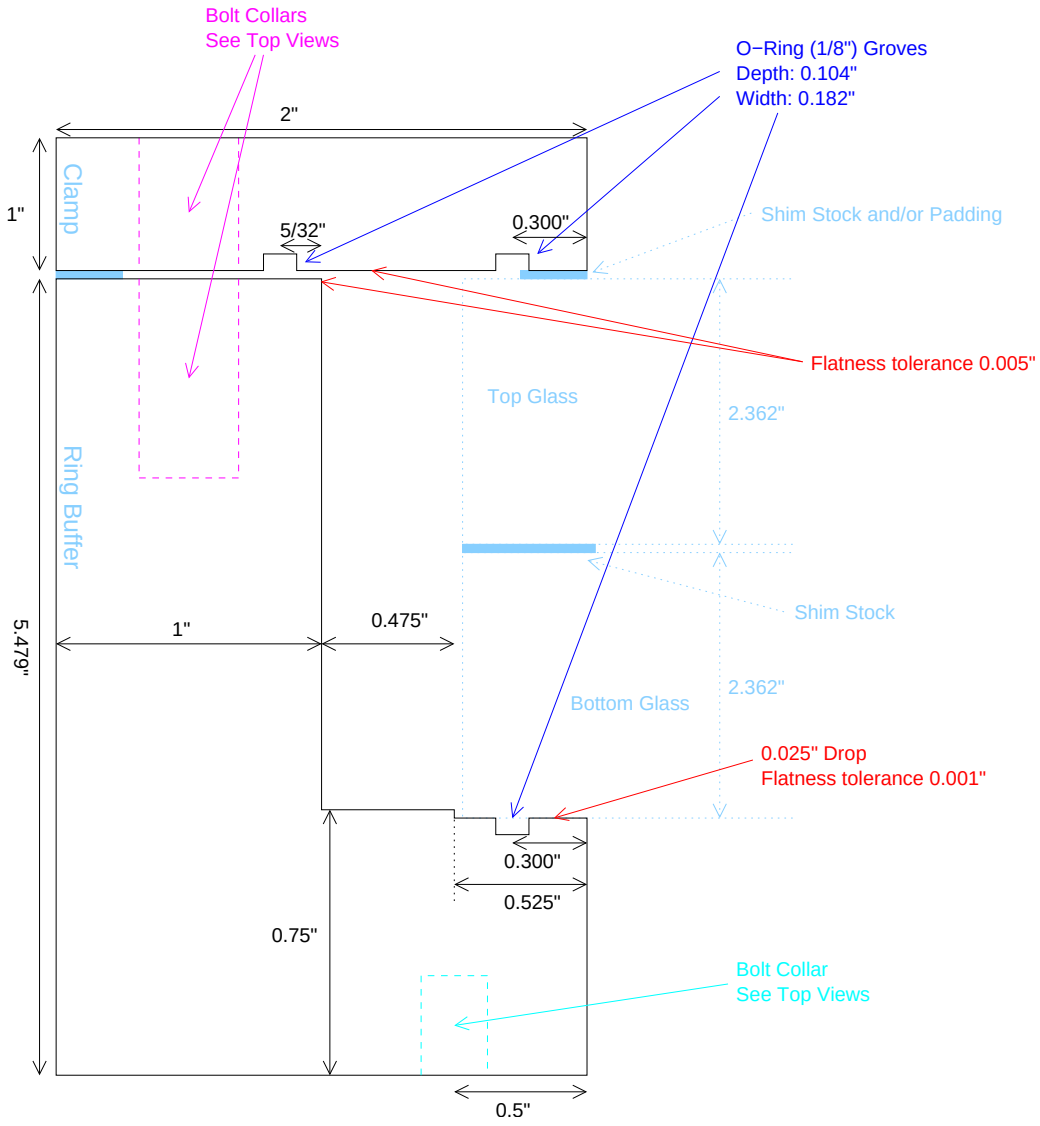

Mickey Moore
471−5425
mgmoore@chaos.ph.utexas.edu
Advisor: H. Swinney

Ring Buffer Top View

Total Diameter (Excluding Tabs): 14.811"

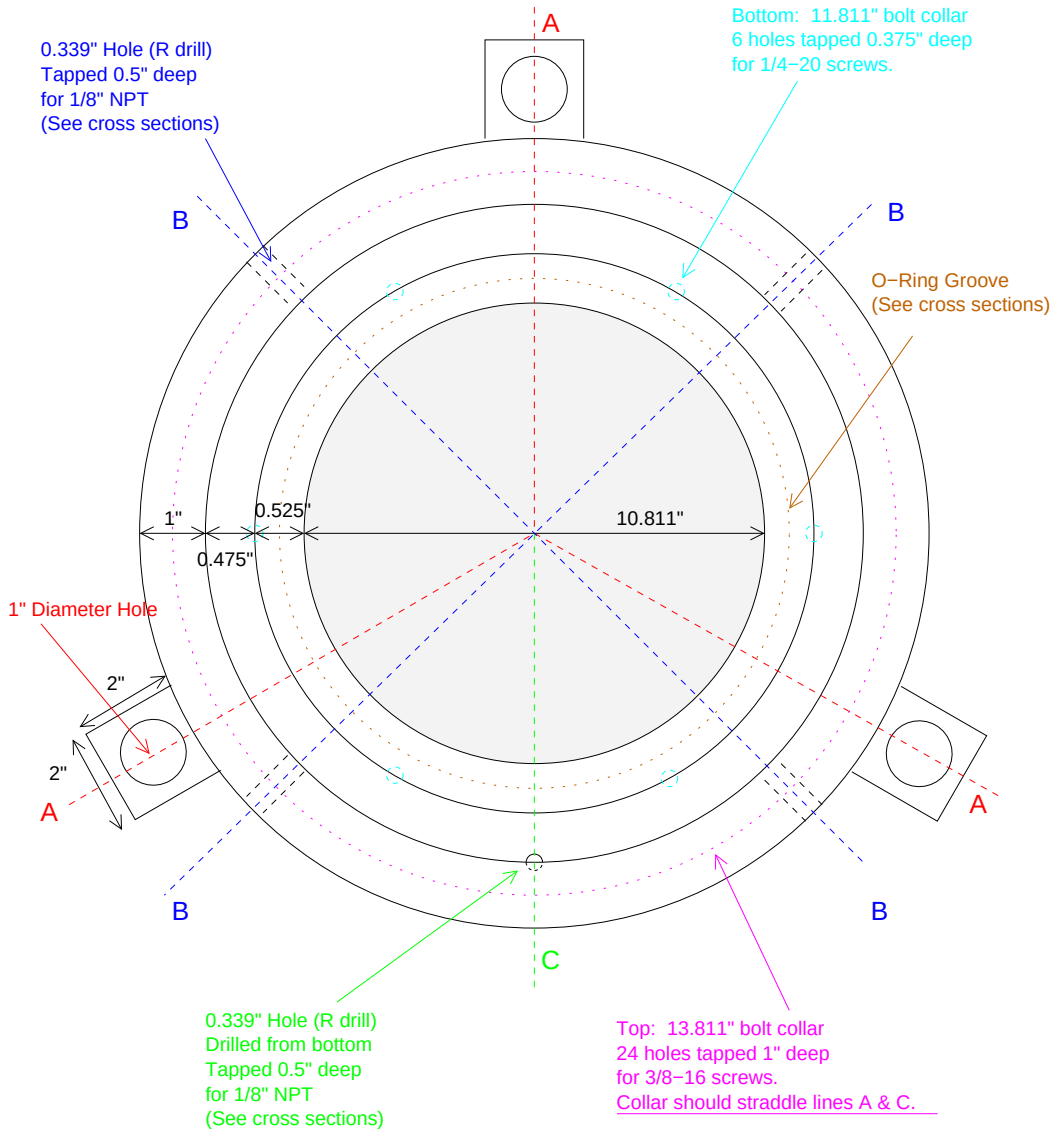

Mickey Moore
471−5425
mgmoore@chaos.ph.utexas.edu
Advisor: H. Swinney

Ring Buffer: Special Cross Sections

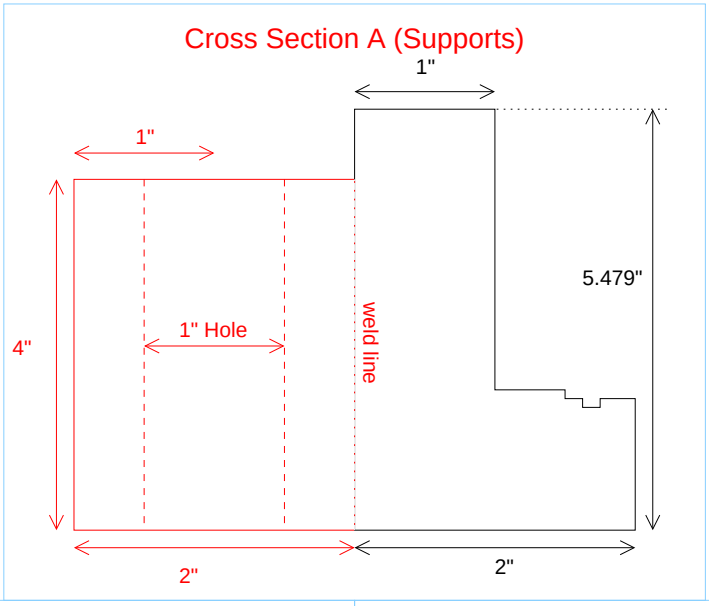

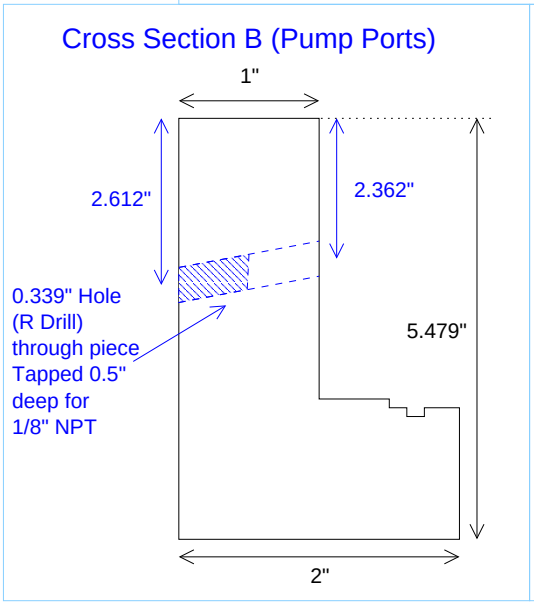

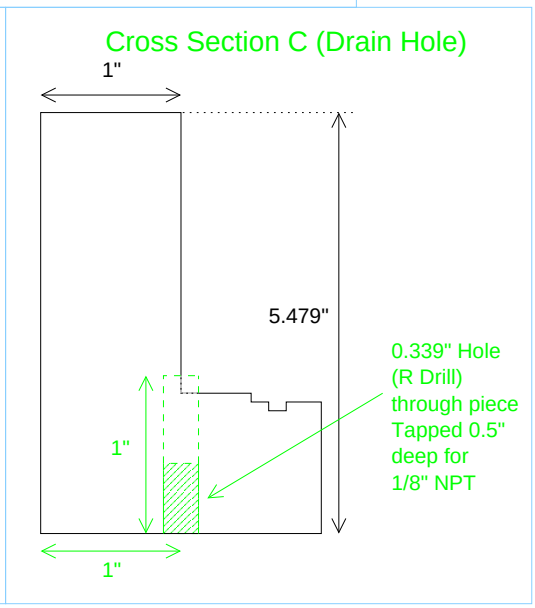

Mickey Moore
471−5425
mgmoore@chaos.ph.utexas.edu
Advisor: H. Swinney

Clamp: Top View

Material: 1" Thick Clear Acrylic
Total Diameter: 14.811"

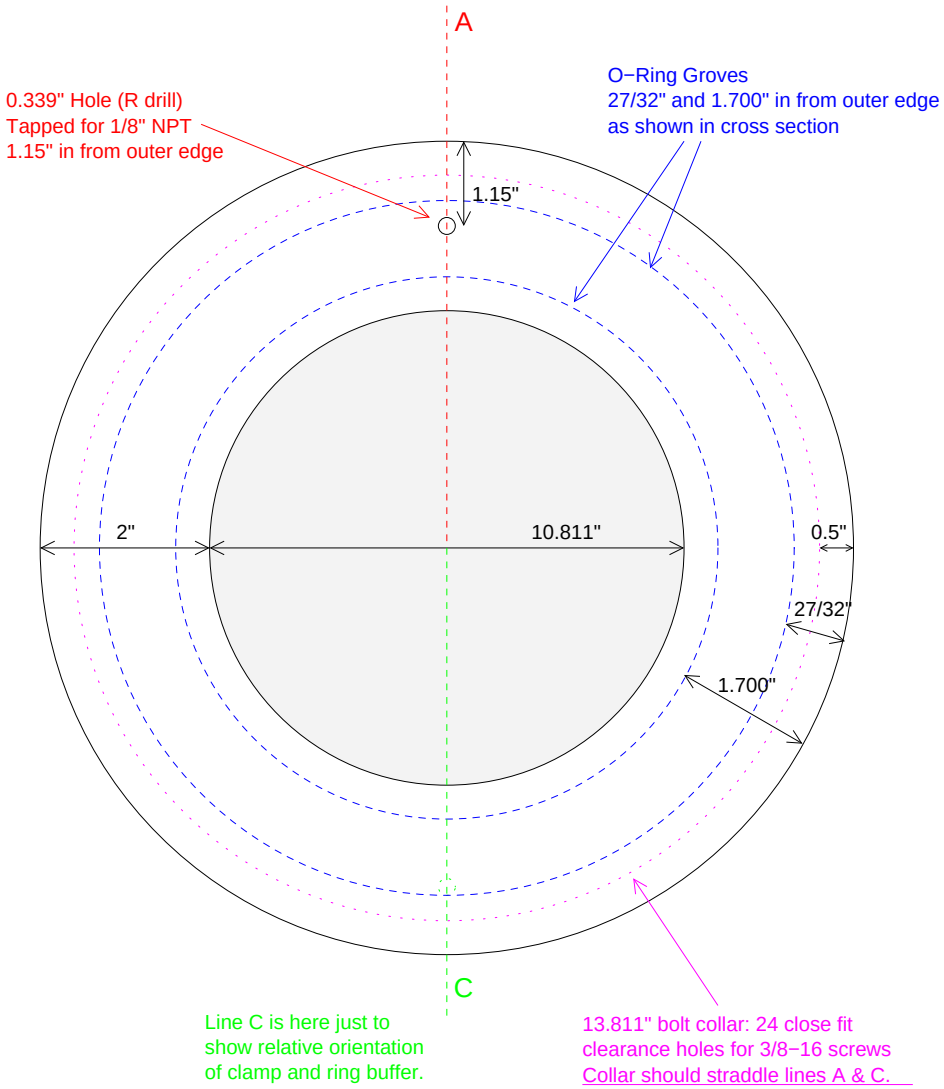

Appendix B

Calculations from Experiment Construction

B.1 Deflection of Glass due to Weight

We begin with equation for the bending of a beam due to a uniform force when the beam is clamped at both ends, from *Building Scientific Apparatus* [97], p. 38.

The shape of the beam across the direction of the width y is

$$z = \frac{fy^2}{24EI}(w^2 - 2wy + y^2), \tag{B.1}$$

where f is the weight per unit length, E is the elastic modulus, I is the centroidal moment of inertia, and w is the width.

This reaches its maximum value at $y = w/2$, so

$$z_{\max} = \frac{f}{24EI}\frac{w^4}{16}. \tag{B.2}$$

First, $I = t^3L/12$, where t is thickness of glass and L is its length. Also, $f = F/L = Ltw\rho g/L = tw\rho g$, where F is total weight of glass, ρ is density of glass, and g is the acceleration due to gravity. Inserting this into eqn. B.2 gives

$$z_{\max} = \frac{tL\rho g w^4}{32Et^3L} = \frac{\rho g w^4}{32Et^2}. \tag{B.3}$$

The experimental values for these parameters are $\rho_{\text{glass}} = 2.58$ g/cm^3, $w = 25.4$ cm, $t = 1.91$ cm, and $E = 1.04 \times 10^{11}$ g/cms^2.

This gives $z_{\max} = 8.71 \times 10^{-5}$ cm, which is 0.17% compared to the smallest value of $b = 0.0508$ cm.

B.2 Deflection of Glass due to Pressure Gradient

We start again with eqn. B.2, but multiplied by 2 since both plates will deflect inward to decrease the gap. The force is caused by the pressure difference between the fluid in the cell and atmospheric pressure. This varies along the length of the cell. To simplify the calculations, we consider the bending of a strip of length $\delta = 1$ cm at the end of the channel near the oil buffer. This will give us an upper bound on the bending; it overestimates it because this strip is in actuality part of the larger glass plate which would lend it support. We then use $I = t^3\delta/12$.

The force per unit length due to the pressure gradient is $f = (\Delta P/\delta)\delta w = w\Delta P$, where $\Delta P = P_{\text{atm}} - P_{\text{cell}}$. We find ΔP from Darcy's Law,

$$\frac{\mathrm{d}P}{\mathrm{d}x} = \frac{12\mu}{b^2}v. \tag{B.4}$$

Integrating over the length of the cell, we get

$$\Delta P = \frac{12\mu v L}{b^2}. \tag{B.5}$$

Bringing all of this together gives

$$\Delta b_{\max} = \frac{3w^5\mu v L}{4Et^3b^2\delta}. \tag{B.6}$$

We will take $V = 0.268$ cm/s to match the figure quoted in chapter 4. We also have $\mu = 10$ cP $= 0.10$ cm^2/s, $L = 254$ cm, and we will find the worst case by using the smallest value of $b = 0.0508$ cm.

This gives $\Delta b_{\max} = 2.90 \times 10^{-3}$ cm, which is 5.71% compared to the smallest b.

The measured deflection for this case was 2.2%, so this approximation estimates the bending within a factor of roughly two.

B.3 Depth of Field

To calculate depth of field, we calculate the nearest (s_n) and farthest (s_f) points still acceptably in focus when focused on an object at s_o; the formulas for this (easily verified by some simple ray optics) are

$$s_f = s_o \frac{h}{h + f - s_o}, \tag{B.7}$$

$$s_n = s_o \frac{h}{h - f + s_o}, \tag{B.8}$$

where $h = f^2/Nc$ is the hyperfocal distance, $f = 80$ mm is the focal length of the lens, N is the f-stop, and c is the "circle of confusion", the maximum tolerable fuzziness. For us, this will be the size of one pixel on the CCD array of the camera, 6.7 μm $= 6.7 \times 10^{-4}$ cm.

The easiest length to set during our design was s_n, which was 286.1 cm (the distance from camera to mirror plus the distance from mirror to cell). So

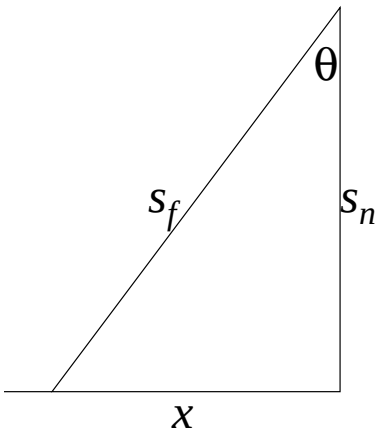

Figure B.1: Calculating the distance down the channel that will be in focus given s_n and s_f: $x = s_f \sin\theta$, $\cos\theta = s_n/s_f$.

we invert eqn. B.8,

$$s_o = s_n \frac{h - f}{h - s_n}. \tag{B.9}$$

Using $N = 16$, we get $s_o = 300.1$ cm and $s_f = 315.5$ cm. We will then be able to view a distance x down the channel from the optical center, where $x = s_f \sin\left[\cos^{-1}(s_n/s_f)\right]$ (see fig. B.1). We get $x = 133.1$ cm, which is more than the required 114.3 cm (45") distance. The next f-stop available on the lens is $N = 11$, which is insufficient because it gives $x = 107.7$ cm.

To achieve all this, we should focus on a point $s_o \sin\left[\cos^{-1}(s_n/s_o)\right] = 90.6$ cm from the optical center of the channel.

Bibliography

[1] A. P. Aldushin and B. J. Matkowsky. Extremum principles for selection in the Saffman-Taylor finger and Taylor-Saffman bubble problems. *Physics of Fluids*, 11(6):1287–1296, 1999.

[2] R. F. Almgren. Comment on 'Selection of the Saffman-Taylor finger width in the absence of surface tension: An exact result'. *Physical Review Letters*, 81(26):5951, 1998.

[3] A. Arneodo, F. Argoul, J. F. Muzy, and M. Tabard. Structural fivefold symmetry in the fractal morphology of diffusion-limited aggregates. *Physica A*, 188(1-3):217–242, 1992.

[4] A. Arnéodo, Y. Couder, G. Grasseau, V. Hakim, and M. Rabaud. Uncovering the analytical Saffman-Taylor finger in unstable viscous fingering and diffusion-limited aggregation. *Physical Review Letters*, 63(9):984–987, 1989.

[5] R. C. Ball and E. Somfai. Theory of diffusion controlled growth. *Physical Review Letters*, 89(13):135503, 2002.

[6] Robin C. Ball, Neill E. Bowler, Leonard M. Sander, and Ellák Somfai. Off-lattice noise reduction and the ultimate scaling of diffusion-limited aggregation in two dimensions. *Physical Review E*, 66:026109, 2002.

[7] Felipe Barra, Benny Davidovitch, Anders Levermann, and Itamar Procaccia. Laplacian growth and diffusion limited aggregation: Different universality classes. *Physical Review Letters*, 87(13):134501, 2001.

[8] J. Bataille. Stabilité d'un écoulement radial non miscible. *Revue Inst. Pétrole*, 23:1349–1364, 1968.

[9] Martine Ben Amar. Exact self-similar shapes in viscous fingering. *Physical Review A*, 43(10):5724–5727, 1991.

[10] Martine Ben Amar, Vincent Hakim, Maurice Mashaal, and Yves Couder. Self-dilating viscous fingers in wedge-shaped Hele-Shaw cells. *Physics of Fluids A*, 3(7):1687–1690, 1991.

[11] E. Ben-Jacob, R. Godbey, Nigel D. Goldenfeld, J. Koplik, H. Levine, T. Mueller, and L. M. Sander. Experimental demonstration of the role of anisotropy in interfacial pattern formation. *Physical Review Letters*, 55(12):1315–1318, 1985.

[12] David Bensimon. Stability of viscous fingering. *Physical Review A*, 33(2):1302–1308, 1986.

[13] David Bensimon, Leo P. Kadanoff, Shoudan Liang, Boris I. Shraiman, and Chao Tang. Viscous flows in two dimensions. *Reviews of Modern Physics*, 58(4):977–999, 1986.

[14] Daniel Bonn and Jacques Meunier. Viscoelastic free-boundary problems: Non-Newtonian viscosity vs normal stress effects. *Physical Review Letters*, 79(14):2662–2665, 1997.

[15] T. Borzsonyi, T. Toth-Katona, Á. Buka, and L. Gránásy. Dendrites regularized by spatially homogeneous time-periodic forcing. *Physical Review Letters*, 83(14):2853–2856, 1999.

[16] Elisabeth Bouchaud. Scaling properties of cracks. *Journal of Physics: Condensed Matter*, 9:4319–4344, 1997.

[17] A. J. Bray. Theory of phase-ordering kinetics. *Advances in Physics*, 51(2):481–587, 2002. (Originally published as Adv. Phys. **43**, 357 (1994).).

[18] C. Bréchignac, Ph. Cahuzac, F. Carlier, C. Colliex, J. Leroux, A. Masson, B. Yoon, and Uzi Landman. Instability driven fragmentation of nanoscale fractal islands. *Physical Review Letters*, 88:196103, 2002.

[19] F. P. Bretherton. The motion of long bubbles in tubes. *Journal of Fluid Mechanics*, 10:166–188, 1961.

[20] J. Casademunt and F. X. Magdaleno. Comment on 'Selection of the Saffman-Taylor finger width in the absence of surface tension: An exact result'. *Physical Review Letters*, 81(26):5950, 1998.

[21] J. Casademunt and F. X. Magdaleno. Dynamics and selection of fingering patterns. recent developments in the Saffman-Taylor problem. *Physics Reports*, 337(1):1–35, 2000.

[22] Ching-Yao Chen and Eckart Meiburg. Miscible porous media displacements in the quarter five-spot configuration. Part 1. The homogeneous case. *Journal of Fluid Mechanics*, 371:233–268, 1998.

[23] Ching-Yao Chen and Eckart Meiburg. Miscible porous media displacements in the quarter five-spot configuration. Part 2. Effect of heterogeneities. *Journal of Fluid Mechanics*, 371:269–299, 1998.

[24] Jing-Den Chen. Growth of radial viscous fingers in a Hele-Shaw cell. *Journal of Fluid Mechanics*, 201:223–242, 1989.

[25] R. L Chuoke, P. van Meurs, and C. van der Poel. The instability of slow immiscible viscous liquid-liquid displacements in permeable media. *Trans. AIME*, 216:188, 1959.

[26] R. Combescot and M. Ben Amar. Selection of Saffman-Taylor fingers in the sector geometry. *Physical Review Letters*, 67(4):453–456, 1991.

[27] R. Combescot and T. Dombre. Selection in the Saffman-Taylor bubble and asymmetrical finger problem. *Physical Review A*, 38(5):2573–2581, 1988.

[28] R. Combescot, V. Hakim, T. Dombre, Y. Pomeau, and A. Pumir. Analytic theory of the Saffman-Taylor fingers. *Physical Review A*, 37(4):1270–1283, 1988.

[29] Roland Combescot, Thierry Dombre, Vincent Hakim, Yves Pomeau, and Alain Pumir. Shape selection of Saffman-Taylor fingers. *Physical Review Letters*, 56(19):2036–2039, 1986.

[30] Massimo Conti, Baruch Meerson, Avner Peleg, and Pavel V. Sasorov. Phase ordering with a global conservation law: Ostwald ripening and coalescence. *cond-mat/0109157*, 2002.

[31] Massimo Conti, Baruch Meerson, and Pavel V. Sasorov. Breakdown of scale invariance in the phase ordering of fractal clusters. *Physical Review Letters*, 80(21):4693–4696, 1998.

[32] Massimo Conti, Baruch Meerson, and Pavel V. Sasorov. Breakdown of dynamical scale invariance in the coarsening of fractal clusters. *cond-mat/9912426v2*, 2000.

[33] Massimo Conti, Baruch Meerson, and Pavel V. Sasorov. Private communication, 2002.

[34] Y. Couder. Viscous fingering in a circular geometry. In E. Stanley and N. Ostrowsky, editors, *Random fluctuations and pattern growth*, pages 75–81. Kluwer Academic Publishers, 1988.

[35] Y. Couder, N. Gérard, and M. Rabaud. Narrow fingers in the Saffman-Taylor instability. *Physical Review A*, 34(6):5175–5178, 1986.

[36] Yves Couder. Growth patterns: From stable curved fronts to fractal structures. In Roberto Artuso, Predrag Cvitanović, and Giulio Casati, editors, *Chaos, order, and patterns*, volume 280 of *NATO ASI Series B: Phyiscs Vol. 280*, pages 203–227. Plenum Press, New York, 1991.

[37] Yves Couder. Viscous fingering as an archetype for growth patterns. In G. K. Batchelor, H. K. Moffatt, and M. G. Worster, editors, *Perspectives in fluid dynamics*, pages 53–104. Cambridge University Press, Cambridge, UK, 2000.

[38] H. Darcy. *Les Fontaines Publiques de la Ville de Dijon: Distribution deau et Filtrage des Eaux*. Victor Dalmont, 1856.

[39] Benny Davidovitch, Anders Levermann, and Itamar Procaccia. Convergent calculation of the asymptotic dimension of diffusion limited aggregates: Scaling and renormalization of small clusters. *Physical Review E*, 62(5):5919–5922, 2000.

[40] A. J. DeGregoria and L. W. Schwartz. Finger breakup in Hele-Shaw cells. *Physics of Fluids*, 28(8):2313–2314, 1985.

[41] A. J. DeGregoria and L. W. Schwartz. A boundary-integral method for two-phase displacement in Hele-Shaw cells. *Journal of Fluid Mechanics*, 164:383–400, 1986.

[42] Dow Corning Corporation. *Information about Low Viscosity Silicone Fluids*, 1997.

[43] Mitchell J. Feigenbaum, Itamar Procaccia, and Benny Davidovich. Dynamics of finger formation in Laplacian growth without surface tension. *Journal of Statistical Physics*, 103(5/6):973–1007, 2001.

[44] Juan Fernandez and G. M. Homsy. Viscous fingering with chemical reaction: Effect of in-situ production of surfactants. *Journal of Fluid Mechanics*, 480:267–281, 2003.

[45] Keith A. Gillow and Sam D. Howison. A bibliography of free and moving boundary problems for Hele-Shaw and Stokes flow, (Last Updated August 19,1998).

[46] P. Gondret, N. Rakotomalala, M. Rabaud, D. Salin, and P. Watzky. Viscous parallel flows in finite aspect ratio Hele-Shaw cell: Analytical and numerical results. *Physics of Fluids A*, 9(6):1841–1843, 1997.

[47] Thomas C. Halsey, Mogens H. Jensen, Leo P. Kadanoff, Itamar Procaccia, and Boris I. Shraiman. Fractal measures and their singularities: The characterization of strange sets. *Physical Review A*, 33(2):1141–1151, 1986.

[48] Harold M. Hastings and George Sugihara. *Fractals: A user's guide for the natural sciences*. Oxford University Press, 1993.

[49] H. S. Hele-Shaw. The flow of water. *Nature*, 58(1489):34–36, 1898.

[50] S. Hill. Channelling in packed columns. *Chemical Engineering Science*, 1(6):247–253, 1952.

[51] G. M. Homsy. Viscous fingering in porous media. *Annual Review of Fluid Mechanics*, 19:271–311, 1987.

[52] D. C. Hong and J. S. Langer. Analytic theory of the selection mechanism in the Saffman-Taylor problem. *Physical Review Letters*, 56(19):2032–2035, 1986.

[53] S.-C. Huang and M. E. Glicksman. Fundamentals of dendritic solidification — II. Development of sidebranch structure. *Acta Metallurgica*, 29:717–734, 1981.

[54] K. Humayun and A. J. Bray. Non-equilibrium dynamics of the Ising model for T less-than/equal-to Tc. *Journal of Physics A*, 24:1915–1930, 1991.

[55] Mogens H. Jensen, Albert Libchaber, Pierre Pelcé, and Giovanni Zocchi. Effect of gravity on the Saffman-Taylor meniscus: Theory and experiment. *Physical Review A*, 35(5):2221–2227, 1987.

[56] Bayard K. Johnson and Robert F. Sekerka. Diffusion-limited aggregation: Connection to a free-boundary problem and lattice anisotropy. *Physical Review E*, 52(6):6404–6414, 1995.

[57] S. Katano and M. Iizumi. Crossover phenomenon in dynamical scaling of phase separation in Fe-Cr alloy. *Physical Review Letters*, 52(10):835–838, 1984.

[58] D. A. Kessler, Z. Olami, J. Oz, I. Procaccia, E. Somfai, and L. M. Sander. Diffusion-limited aggregation and viscous fingering in a wedge: Evidence for a critical angle. *Physical Review E*, 57(6):6913–6916, 1998.

[59] David A. Kessler, Joel Koplik, and Herbert Levine. Pattern selection in fingered growth phenomena. *Advances in Physics*, 37(3):255–339, 1988.

[60] David A. Kessler and Herbert Levine. Stability of finger patterns in Hele-Shaw cells. *Physical Review A*, 32(3):1930–1933, 1985.

[61] David A. Kessler and Herbert Levine. Theory of the Saffman-Taylor "finger" pattern. II. *Physical Review A*, 33(4):2634–2639, 1986.

[62] Ljubinko Kondic, Peter Palffy-Muhoray, and Michael J. Shelley. Models of non-Newtonian Hele-Shaw flow. *Physical Review E*, 54(5):4536–4539, 1996.

[63] Ljubinko Kondic, Michael J. Shelley, and Peter Palffy-Muhoray. Non-Newtonian Hele-Shaw flow and the Saffman-Taylor instability. *Physical Review Letters*, 80(7):1433–1436, 1998.

[64] Anne R. Kopf-Sill and G. M. Homsy. Nonlinear unstable viscous fingers in Hele-Shaw flows. I. experiments. *Physics of Fluids*, 31(2):242–249, 1988.

[65] Eric Kostelich. Personal communication, 2003.

[66] H. La Roche, J. F. Fernández, M. Octavio, A. G. Loeser, and C. J. Lobb. Diffusion-limited-aggregation model for Poisson growth. *Physical Review A*, 44(10):R6185–R6188, 1991.

[67] E. Lajeunesse and Y. Couder. On the tip-splitting instability of viscous fingers. *Journal of Fluid Mechanics*, 419:125–149, 2000.

[68] L. D. Landau and E. M. Lifshitz. *Fluid mechanics*, volume 6 of *Landau and Lifshitz: Course in theoretical physics*. Butterworth-Heinemann, second, revised edition, 1998.

[69] J. S. Langer. Instabilities and pattern formation in crystal growth. *Reviews of Modern Physics*, 52(1):1–28, 1980.

[70] K. S. Lee and E. L. Claridge. *Society of Petroleum Engineers Journal*, pages 56–62, 1968.

[71] E. Lemaire, P. Levitz, G. Daccords, and H. Van Damme. From viscous fingering to viscoelastic fracturing in colloidal fluids. *Physical Review Letters*, 67(15):2009–2012, 1991.

[72] Anders Levermann and Itamar Procaccia. New algorithm for parallel Laplacian growth by iterated conformal maps. *cond-mat/0305521*, 2003.

[73] I. M. Lifshitz. *Zh. éksp. teor. Fiz.*, 42:1354, 1962. (Engl. Transl., 1962, Sov. Physics JETP, 15, 939).

[74] I. M. Lifshitz and V. V. Slyozov. The kinetics of precipitation from supersaturated solid solutions. *Journal of Physics and Chemistry of Solids*, 19(1-2):35–50, 1961.

[75] Azi Lipshtat, Baruch Meerson, and Pavel V. Sasorov. Anomalous dynamic scaling in locally conserved coarsening of fractal clusters. *Physical Review E*, 65:050501, 2002.

[76] Gloria B. Lubkin. Combustion in two dimensions yields fingering instability. *Physics Today*, 52(1):19–21, 1999. (Also cover photograph.).

[77] F. X. Magdaleno and J. Casademunt. Surface tension and dynamics of fingering patterns. *Physical Review E*, 57(4):3707–3710, 1998.

[78] F. X. Magdaleno and J. Casademunt. Two-finger selection theory in the Saffman-Taylor problem. *Physical Review E*, 60(5):5013–5016, 1999.

[79] J. Marro, Joel L. Lebowitz, and M. H. Kalos. Computer simulation of the time evolution of a quenched model alloy in the nucleation region. *Physical Review Letters*, 43(4):282–285, 1979.

[80] T. Maxworthy. The nonlinear growth of a gravitationally unstable interface in a Hele-Shaw cell. *Journal of Fluid Mechanics*, 177:207–232, 1987.

[81] S. E. May and Maher. Fractal dimension of radial fingering patterns. *Physical Review A*, 40(3):1723–1726, 1989.

[82] K. V. McCloud and J. V. Maher. Experimental perturbations to Saffman-Taylor flow. *Physics Reports*, 260(3):139–185, 1995.

[83] K. V. McCloud and J. V. Maher. Pattern selection in an anisotropic Hele-Shaw cell. *Physical Review E*, 51(2):1184–1190, 1995.

[84] Steve McConnell. *Code complete: A practical handbook of software construction.* Microsoft Press, 1993.

[85] J. W. McLean and P. G. Saffman. The effect of surface tension on the shape of fingers in a Hele-Shaw cell. *Journal of Fluid Mechanics*, 102:455–469, 1981.

[86] John Weidman McLean. *I. The fingering problem in flow through porous media, II. The kinetic equation for Hamiltonian systems.* Ph.D., California Institute of Technology, 1980.

[87] Paul Meakin. Universality, nonuniversality, and the effects of anisotropy on diffusion-limited aggregation. *Physical Review A*, 33(5):3371–3382, 1986.

[88] Paul Meakin, Robin C. Ball, P. Ramanlal, and L. M. Sander. Structure of large two-dimensional square-lattice diffusion-limited aggregates: Approach to asymptotic behavior. *Physical Review A*, 35(12):5233–5239, 1987.

[89] Mark Mineev. Personal communication.

[90] Mark Mineev-Weinstein. Mineev-weinstein replies. *Physical Review Letters*, 81(20):4529, 1998.

[91] Mark Mineev-Weinstein. Mineev-weinstein replies. *Physical Review Letters*, 81(26):5952, 1998.

[92] Mark Mineev-Weinstein. Selection of the Saffman-Taylor finger width in the absence of surface tension: An exact result. *Physical Review Letters*, 80(10):2113–2116, 1998.

[93] Mark B. Mineev-Weinstein and Silvina Ponce Dawson. Class of nonsingular exact solutions for Laplacian pattern formation. *Physical Review E*, 50(1):24–27, 1994.

[94] José A. Miranda. Analytical approach to viscous fingering in a cylindrical Hele-Shaw cell. *Physical Review E*, 65:026303, 2002.

[95] José A. Miranda. Nonlinear effects due to gravity in a conical Hele-Shaw cell. *Physical Review E*, 65:036310, 2002.

[96] José A. Miranda, Fernando Parisio, Fernando Moraes, and Michael Widom. Gravity-driven instability in a spherical Hele-Shaw cell. *Physical Review E*, 63:016311, 2000.

[97] John H. Moore, Christopher C. Davis, and Michael A. Coplan. *Building Scientific Apparatus*. Perseus Books Publishing, second edition, 1991.

[98] Mitchell G. Moore, Anne Juel, John M. Burgess, W. D. McCormick, and Harry L. Swinney. Fluctuations in viscous fingering. *Physical Review E*, 65:030601, 2002.

[99] Mitchell G. Moore, Anne Juel, John M. Burgess, W. D. McCormick, and Harry L. Swinney. Fluctuations and pinch-offs observed in viscous fingering. In Visarath In, Ljupco Kocarev, Thomas L. Carroll, Bruce J. Gluckman, Stefano Boccaletti, and Jürgen Kurths, editors, *Proceedings of the 7th Experimental Chaos Conference*, pages 189–194. Springer-Verlag, 2003.

[100] W. W. Mullins and R. F. Sekerka. Stability of a planar interface during solidification of a dilute binary alloy. *Journal of Applied Physics*, 35(2):444–451, 1964.

[101] M. A. Novotny, R. Tao, and D. P. Landau. Relaxation in DLA with surface tension. *Journal of Physics A*, 23(14):3271–3278, 1990.

[102] Christian Pankiewitz and Eckart Meiburg. Miscible porous media displacements in the quarter five-spot configuration. Part 3. Non-monotonic viscosity profiles. *Journal of Fluid Mechanics*, 388:171–195, 1999.

[103] Fernando Parisio, Fernando Moraes, José A. Miranda, and Michael Widom. Saffman-Taylor problem on a sphere. *Physical Review E*, 63:036307, 2000.

[104] C. W. Park, S. Gorell, and G. M. Homsy. Two-phase displacement in Hele-Shaw cells: Experiments on viscously driven instabilities. *Journal of Fluid Mechanics*, 141:257–287, 1984.

[105] C. W. Park and G. M. Homsy. Two-phase displacement in Hele-Shaw cells: Theory. *Journal of Fluid Mechanics*, 139:291–308, 1984.

[106] C. W. Park and G. M. Homsy. The instability of long fingers in Hele-Shaw flows. *Physics of Fluids*, 28(6):1583–1585, 1985.

[107] Lincoln Paterson. Radial fingering in a Hele-Shaw cell. *Journal of Fluid Mechanics*, 113:513–529, 1981.

[108] E. Pauné, M. Siegel, and J. Casademunt. Effects of small surface tension in Hele-Shaw multifinger dynamics: An analytical and numerical study. *Physical Review E*, 66:046205, 2002.

[109] Pierre Pelcé. *Dynamics of curved fronts*. Academic Press, 1988.

[110] Avner Peleg. Personal communication, 2002.

[111] Avner Peleg, Massimo Conti, and Baruch Meerson. Normal scaling in globally conserved interface-controlled coarsening of fractal clusters. *Physical Review*, 64:036127, 2001.

[112] J. D. Pelletier. Statistical self-similarity of magmatism and volcanism. *Journal of Geophysical Research*, 104(B7):15425–15438, 1999.

[113] Philippe Petitjeans, Ching-Yao Chen, Eckart Meiburg, and Tony Maxworthy. Miscible quarter five-spot displacements in a Hele-Shaw cell and the role of flow-induced dispersion. *Physics of Fluids*, 11(7):1705–1716, 1999.

[114] E. Pitts. Penetration of fluid into a Hele-Shaw cell: The Saffman-Taylor experiment. *Journal of Fluid Mechanics*, 97(1):53–64, 1980.

[115] Eugenia Corver Poiré. *Anisotropic viscous fingering.* Ph.D., McGill University, 1995.

[116] Eugenia Corvera Poiré and Martine Ben Amar. Finger behavior of a shear thinning fluid in a Hele-Shaw cell. *Physical Review Letters*, 81(10):2048–2051, 1998.

[117] Olivier Praud. Personal communication, 2003.

[118] M. Rabaud, Y. Couder, and N. Gerard. Dynamics and stability of anomalous Saffman-Taylor fingers. *Physical Review A*, 37(3):935–947, 1988.

[119] S. N. Rauseo, P. D. Barnes, and J. V. Maher. Development of radial fingering patterns. *Physical Review A*, 35(3):1245–1251, 1987.

[120] D. A. Reinelt. Interface conditions for two-phase displacement in Hele-Shaw cells. *Journal of Fluid Mechanics*, 183:219–234, 1987.

[121] Shashwati Roy and S. Tarafdar. Patterns in the variable Hele-Shaw cell for different viscosity ratios: Similarity to river network geometry. *Physical Review E*, 54(6):6495–6499, 1996.

[122] P. G. Saffman and Geoffrey Taylor. The penetration of a fluid into a porous medium or Hele-Shaw cell containing a more viscous liquid. *Proceedings of the Royal Society of London. Series A, Mathematical and Physical Sciences*, 245(1242):312–329, 1958.

[123] L. M. Sander. Lecture at conference: Pattern formation and diffusion-limited growth, 2001.

[124] Leonard M. Sander. Diffusion-limited aggregation: A kinetic critical phenomenon? *Contemporary Physics*, 41(4):203–218, 2000.

[125] A. Sarkissian and H. Levine. Comment on 'Selection of the Saffman-Taylor finger width in the absence of surface tension: An exact result'. *Physical Review Letters*, 81(20):4528, 1998.

[126] L. W. Schwartz and A. J. DeGregoria. Simulation of Hele-Shaw fingering with finite-capillary-number effects included. *Physical Review A*, 35(1):276–279, 1987.

[127] Leonard Schwartz. Stability of Hele-Shaw flows: The wetting-layer effect. *Physics of Fluids*, 29(9):3086–3088, 1986.

[128] Leonard W. Schwartz and Anthony J. DeGregoria. Two-phase flow in Hele-Shaw cells: Numerical studies of sweep efficiency in a five-spot pat-

tern. *Journal of the Australian Mathematical Society, Series B*, 29:375–400, 1988.

[129] Eran Sharon, Mitchell G. Moore, W. D. McCormick, and Harry L. Swinney. Fractal coarsening of viscous fingers. *Physical Review Letters*, to appear, 2003.

[130] Boris I. Shraiman. Velocity selection and the Saffman-Taylor problem. *Physical Review Letters*, 56(19):2028–2031, 1986.

[131] Michael Siegel and Saleh Tanveer. Singular perturbation of smoothly evolving Hele-Shaw solutions. *Physical Review Letters*, 76(3):419–422, 1996.

[132] Michael Siegel, Saleh Tanveer, and Wei shen Dai. Singular effects of surface tension in evolving Hele-Shaw flows. *Journal of Fluid Mechanics*, 323:201–236, 1996.

[133] Eric D. Siggia. Late stages of spinodal decomposition in binary mixtures. *Physical Review Letters*, 20(2):595–605, 1979.

[134] P. Tabeling and A. Libchaber. Film draining and the Saffman-Taylor problem. *Physical Review A*, 33(1):794–796, 1986.

[135] P. Tabeling, G. Zocchi, and A. Libchaber. An experimental study of the Saffman-Taylor instability. *Journal of Fluid Mechanics*, 177:67–82, 1987.

[136] S. Tanveer. Analytic theory for the selection of a symmetric Saffman-Taylor finger in a Hele-Shaw cell. *Physics of Fluids*, 30(6):1589–1605, 1987.

[137] S. Tanveer. Analytic theory for the selection of Saffman-Taylor fingers in the presence of thin film effects. *Proceedings of the Royal Society of London. Series A, Mathematical and Physical Sciences*, 428:511–545, 1990.

[138] S. Tanveer. Some analytical properties of solutions to a two-dimensional steadily translating inviscid bubble. *Proceedings of the Royal Society of London. Series A, Mathematical and Physical Sciences*, 452(1949):1397–1410, 1996.

[139] S. Tanveer. Surprises in viscous fingering. *Journal of Fluid Mechanics*, 409:273–308, 2000.

[140] G. I. Taylor and P. G. Saffman. A note on the motion of bubbles in a hele-shaw cell and porous medium. *Quarterly Journal of Mechanics and Applied Mathematics*, 12:265, 1959.

[141] H. Thomé, M. Rabaud, V. Hakim, and Y. Couder. The Saffman-Taylor instability: From the linear to the circular geometry. *Physics of Fluids A*, 1(2):224–240, 1989.

[142] Jean Marc Vanden-Broeck. Fingers in a Hele-Shaw cell with surface tension. *Physics of Fluids*, 26(8):2033–2034, 1983.

[143] D. H. Vlad and J. V. Maher. Tip-splitting instabilities in the channel Saffman-Taylor flow of constant viscosity elastic fluids. *Physical Review E*, 61(5):5439–5444, 2000.

[144] C. Wagner. *Z. Elektrochem.*, 65:581, 1961.

[145] T. A. Witten and L. M. Sander. Diffusion-limited aggregation, a kinetic critical phenomenon. *Physical Review Letters*, 47(19):1400–1403, 1981.

[146] H. Zhao and J. V. Maher. Viscous-fingering experiments with periodic boundary conditions. *Physical Review A*, 42(10):5894–5897, 1990.

[147] P. Zhuravlev. *Zap Leningrad Com. Inst.*, 133:54, 1956. (in Russian).

[148] Ory Zik, Zeev Olami, and Elish Moses. Fingering instability in combustion. *Physical Review Letters*, 81(18):3868–3871, 1998.

[149] Giovanni Zocchi, Bruce E. Shaw, Albert Libchaber, and Leo P. Kadanoff. Finger narrowing under local perturbations in the Saffman-Taylor problem. *Physical Review A*, 36(4):1894–1900, 1987.

Vita

Mitchell George Moore was born in Dearborn, MI on 22 December 1969. He is the son of Thomas Sidney Moore and Patricia Jean Moore. He graduated from Northville High School in Northville, MI in June 1988 and received a B.S. in General Physics and Mathematical Sciences from the University of Michigan (Ann Arbor, MI) in December 1995. He began his graduate studies in pursuit of a Ph.D. in Physics at the University of Texas at Austin in September 1996.

Permanent address: 1823-A River Crossing Circle
Austin, Texas 78741-3281

This dissertation was typeset with LaTeX 2_ε[†] by the author.

[†]LaTeX 2_ε is a document preparation system developed by Leslie Lamport as a special version of Donald Knuth's TeX Program.